Carbon dioxide removal from industrial gases using an indirectly heated and cooled temperature swing adsorption process.

Von der Fakultät für Ingenieurwissenschaften,
Abteilung Maschinenbau und Verfahrenstechnik

der

Universität Duisburg-Essen
genehmigte Dissertation zum Erwerb des akademischen Grades

eines

Doktors der Ingenieurwissenschaften
Dr.-Ing.

von

Gabriel Salazar Duarte
aus
Bogota / Kolumbien

Tag der mündlichen Prüfung: 07.04.2017

Gutachter:
Prof. Dr.-Ing. Dieter Bathen
Prof. Dr.-Ing. Kai-Olaf Hinrichsen (TUM)

Acknowledgements

First of all, I would like to express my deepest gratitude to Prof. Dr.-Ing. Bathen for accepting being my advisor, for the continuous support throughout the completion of this thesis, for his motivation, the fruitful discussions, and immense knowledge. His guidance always helped me during my time of research and during the writing of this thesis.

Furthermore, I would like to thank Prof. Dr.-Ing. Hinrichsen for being the second examiner of this thesis. Also, I would like to thank the rest of my thesis committee: Prof. Dr. Atakan and Prof. Dr. Mohri.

I am also indebted to Alexander Sakowski and Nicolas Berg for their valuable work in the frame of their Master Thesis.

Many thanks also go to my colleagues from the institute of thermal process engineering for always making me feel part of the team every time I went to visit or at conferences. In particular, I would like to mention Florian Birkmann, Christian Bläker, Volkmar Chowanietz, Frederik Berg, Dirk Bucher and Guido Schraven.

In addition, I would like to express my deepest gratitude to Dr.-Ing. Voss from Linde Engineering for giving me the chance to do my PhD thesis at his department. Also, I would like to especially thank Dr.-Ing. Schürer for all his help, guidance and fruitful discussions during my time at Linde. To all my colleagues at RDA I also want to express my gratitude for the great working atmosphere. Dr. Tota and Dr. Stegmaier, thank you very much for all the fruitful and interesting discussions. Mr. Fichtner, thank you very much for all your support during my experimental work.

Finally, I would like to thank my family for their unconditional support, love and for always believing in me.

Gabriel Salazar Duarte

Abstract

In addition to absorption and membrane processes, adsorption processes offer the possibility of capturing and recovering CO_2 from fossil fueled power plants. Because of the long heating and cooling times required in a TSA process and because during desorption the recovered component is diluted, an indirectly heated and cooled TSA process is proposed for CO_2 capture. The suitability of the indirectly heated and cooled temperature swing adsorption process for CO_2 capture is investigated in this work. The heat transfer characteristics of an adsorbent packed bed with and without convection are investigated, since heat transfer plays a major role in this process. The adsorption characteristics of an indirectly heated and cooled adsorber is also an important topic in this work. A multidimensional mathematical model is derived in order to simulate the indirect heated and cooled temperature swing adsorption process.

The heat conductivity of the solid particle and the wall Biot number are important model parameters and are required for modeling the indirect heated and cooled TSA process. The convective contribution to the radial heat conductivity at low Péclet numbers showed a similar relationship to the relationship that is postulated in the literature for higher Péclet numbers. Contrary to the radial heat conductivity, the convective contribution to the wall heat transfer coefficient shows no clear relationship. The reasons for this are the correlation between the parameters and that the non-convective contribution dominates over the range of Péclet numbers that are used in this work.

To investigate the adsorption characteristics, an isotherm is scaled by comparing the experimental loading value that is measured with a breakthrough curve and the loading obtained by the isotherm. This is necessary since the same activation procedure cannot be achieved during the in situ activation of the bed. The model is validated and kinetic parameters are calculated. Moreover, the agreement between the model and the measurements is strong, especially for the CO_2 concentration. The small discrepancies between the measured and predicted temperature profiles can be explained on one hand by flow disturbances and on the other hand by the uncertainty caused by scaling the isotherm. The recoveries obtained by the model are within the range of the experimental error and show the same dependency of the recovery with the regeneration temperature. The average purity of the recovered CO_2 is also within the experimental error.

Using the derived model and the determined kinetic parameters, a parametric sweep is conducted in order to see the influence of different parameters on the process. The influence is measured by three different key performance indicators: the average purity of the recovered CO_2, the CO_2 recovery, and the specific energy required. The numerical study shows that promising results are obtained by reducing the radial thermal resistance. Using optimal parameters, high recoveries and purities can be achieved and specific

energy requirements that are lower than the benchmark process (amine wash).

This work shows, that the indirectly heated and cooled TSA process offers a promising alternative to CO_2 capture.

Zusammenfassung

Adsorptionsprozesse bieten neben Absorptions- und Membranprozessen die Möglichkeit CO_2 aus Rauchgasen zu entfernen. Allerdings zeigt der klassische TSA-Prozess Nachteile wie z.B. die langen Regenrationszeiten und die Verdünnung der desorbierten Komponente durch die direkte Beheizung des Bettes. Aus diesem Grund werden indirekt beheizte und gekühlte TSA-Prozesse für die CO_2 Abtrennung aus Rauchgasen vorgeschlagen. Die Einsetzbarkeit eines solchen indirekt beheizten und gekühlten TSA Prozesses wird in dieser Arbeit untersucht. Hierfür wird die Wärmeübertragung in adsorptiven Schüttungen mit und ohne Konvektion untersucht. Ebenso wird die Adsorptionscharakteristik untersucht sowie ein mathematisches Modell entwickelt um diesen Prozess zu simulieren.

Mithilfe nicht durchströmter Wärmeübertragungsversuche werden die Wärmeleitfähigkeit der Partikeln unter Benutzung des Zehner/Bauer/Schlünder-Models sowie die Wand Biot-Zahl ermittelt. Beide Parameter sind zwingend erforderlich für das mathematische Modell. Bei den Versuchen mit der durchströmten Schüttung bei geringen Péclet-Zahlen kann für die effektive radiale Wärmeleitfähigkeit ein ähnlicher Zusammenhang festgestellt werden, wie der Zusammenhang, der in der Literatur für größere Péclet-Zahlen postuliert wird. Im Gegensatz dazu kann kein Zusammenhang für den konvektiven Beitrag des Wandwärmeüberganges beobachtet werden. Der Grund liegt an der Korrelation beider Parameter und außerdem daran, dass der nicht konvektive Anteil in dem hier untersuchten Péclet Bereich dominiert.

Um die Adsorptionscharakteristik zu untersuchen, wird eine Adsorptionsisotherme skaliert, um die tatsächliche Kapazität der Schüttung zu reproduzieren. Dies ist erforderlich, da die Schüttung nicht unter denselben Bedingungen in situ aktviert werden konnte. Anschließend wird das entwickelte Modell mithilfe der Experimente validiert und kinetische Parameter werden ermittelt. Die Übereinstimmung zwischen Modell und Versuchen ist sehr zufriedenstellend, besonders für die CO_2 Konzentration. Die Unterschiede bei den Temperaturprofilen können zum einem durch die geringe Péclet Zahl erklärt werden, da Strömungseffekte die Temperaturprofile beeinflussen können. Zum anderen durch die Skalierung der Isotherme, da dies eine gewisse Unsicherheit mit sich bringt. Die berechneten Ausbeuten liegen alle innerhalb des experimentellen Fehlers und zeigen dieselbe Abhängigkeit von der Regenerationstemperatur. Die berechneten Reinheiten liegen ebenfalls innerhalb des experimentellen Fehlers.

Anschließend wird eine Parameter-Studie mithilfe eines selbst entwickelten mathematischen Modells durchgeführt. Diese dient dazu, den Einfluss unterschiedlicher Parameter auf den Prozess zu untersuchen. Der Einfluss auf den Prozess wird anhand von drei unterschiedlicher Leistungskennzahlen beurteilt, nämlich der Reinheit des zurückgewonnenen CO_2, der Ausbeute an CO_2 und des spezifische Energieverbrauchs.

Die nummerische Studie zeigt, dass bei einer Minimierung des radialen thermischen Widerstandes vielversprechende Ergebnisse erzielt werden können. Hohe Reinheiten und hohe Ausbeuten sowie ein geringerer spezifischen Energieverbrauch als bei den Referenzverfahren, der Aminwäsche, kann erzielt werden, wenn optimale Parameter ausgewählt werden.

Diese Arbeit zeigt, dass der indirekt beheizte und gekühlte TSA-Prozess eine vielversprechende alternative zur CO_2 Trennung ist.

Contents

List of Figures

List of Tables

Nomenclature

Roman Symbols

Symbol	Description	Unit
a	structure parameter	-
a_s	surface to volume ratio	$^{1}/_{\mathrm{m}}$
a_{spec}	surface area	m^2
A	area	m^2
A_1	model parameter	$^{\mathrm{Pa \cdot s}}/_{\mathrm{m}^2}$
A_2	model parameter	$^{\mathrm{kg}}/_{\mathrm{m}^4}$
A_3	parameter for uncertainty estimation	$^{1}/_{\mathrm{mol}}$
A_4	parameter for uncertainty estimation	$^{1}/_{\mathrm{mol}}$
$A_{\text{heat conductivity}}$	dimensionless parameter for convective heat conductivity	-
ΔA	differential surface area	m^2
b	Langmuir parameter	$^{1}/_{\mathrm{bar}}$
B_{ZBS}	Zehner/Bauer/Schlünder model parameter	-
c	concentration	$^{\mathrm{mol}}/_{\mathrm{m}^3}$
c_{p}	heat capacity	$^{\mathrm{J}}/_{\mathrm{kg \cdot K}}$
d	diameter	m
d_{p}	particle diameter	m
d_{pore}	pore diameter	m
D	diffusion/dispersion coefficient	$^{\mathrm{m}^2}/_{\mathrm{s}}$
f	function	-
F	function	-
$\boldsymbol{g}$	gravity	$^{\mathrm{m}}/_{\mathrm{s}^2}$
g_{Adsorpt}	specific free enthalpy of the adsorpt phase	$^{\mathrm{J}}/_{\mathrm{kg}}$
g_{fluid}	specific free enthalpy of the fluid phase	$^{\mathrm{J}}/_{\mathrm{kg}}$
$\dot{G}$	mole source/sink term	$^{\mathrm{mol}}/_{\mathrm{s}}$
h	triangle height	m
H	height	m
$\dot{H}$	convective heat flow	W

ΔH_{ads}	heat of adsorption	$^{\text{kJ}}/_{\text{mol}}$
$\boldsymbol{I}$	direction vector	-
k	x,y,z coordinate	m
k_{LDF}	linear-driving-force kinetic parameter	$^{1}/_{\text{s}}$
K_{rad}	model parameter of convective heat conductivity	-
m_{scale}	scaling factor	-
$\dot{m}$	mass flow	$^{\text{kg}}/_{\text{s}}$
$\dot{m}_g$	mass flow density	$^{\text{kg}}/_{\text{m}^2\cdot\text{s}}$
M	molecular weight	$^{\text{g}}/_{\text{mol}}$
$\dot{M}$	mass flow	$^{\text{kg}}/_{\text{s}}$
$\dot{n}$	mole flow	$^{\text{mol}}/_{\text{s}}$
N	moles	mol
N	Zehner/Bauer/Schlünder model parameter	-
$\dot{N}$	mole flow	$^{\text{mol}}/_{\text{s}}$
p	pressure	bar
$\boldsymbol{p}$	parameter vector	-
P	probability	-
q	loading	$^{\text{mol}}/_{\text{kg}}$
q^{eq}	equilibrium loading	$^{\text{mol}}/_{\text{kg}}$
q_{∞}	saturation loading	$^{\text{mol}}/_{\text{kg}}$
$\dot{Q}$	conductive heat flow	W
r	radial coordinate or radius	m
r_{p}	particle radius	m
R	radius	m
$\mathbb{R}$	ideal gas constant	$^{\text{J}}/_{\text{mol}\cdot\text{K}}$
s	uncertainty	-
t	time	s
T	temperature	K
u	velocity	$^{\text{m}}/_{\text{s}}$
U	inner energy	J
V	volume	m^3
V_{D}	atomic diffusion volumes	cm^3
$\dot{V}$	volume flow	$^{\text{m}^3}/_{\text{s}}$

$\dot{V}_n$	standard volume flow	$^{\mathrm{Nm^3}}/_{\mathrm{s}}$
ΔV	differential volume	m^3
$\dot{w}$	volumetric heat source	$^{\mathrm{W}}/_{\mathrm{m^3}}$
$\dot{W}$	heat source/sink	W
x	parameter	-
$x_{\min}$	Eigenberger and Bey model parameter	m
y	mole fraction	-
Y	driving force for mass transport	$^{\mathrm{kg}}/_{\mathrm{m^3}}$
z	axial coordinate	m

Greek Symbols

Symbol	Description	Unit
α	heat transfer coefficient	$^{W}/_{m^2 \cdot K}$
ϵ	porosity	-
$\boldsymbol{\phi}$	combined momentum flux	Pa
ϕ	surface to volume ratio	$^{1}/_{m}$
ϕ_{Maxwell}	Maxwell parameter	-
η	dynamic viscosity	Pa·s
λ	heat conductivity	$^{W}/_{m \cdot K}$
Λ	effective heat conductivity	$^{W}/_{m \cdot K}$
μ_{p}	tortuosity	-
θ	Wilke model parameter	-
ρ	density	$^{kg}/_{m^3}$
σ	standard deviation	-
$\boldsymbol{\tau}$	stress tensor	Pa

Dimensionless Numbers

Symbol	Description
Bi	Biot number
Kn	Kndusen number
Nu	Nusselt number
Pe	Péclet number
Pr	Prandtl number
Re	Reynolds number

Subscripts

Symbol	Description
0	superficial / non convective
1	component 1
2	component 2
∞	saturation / constant value
Ax	axial
bed	particle bed
c	core
conc	concentration
conv	convective
CO_2	carbon dioxide
diff	free gas diffusion
eff	effective
exp	experimental
f	fluid
g	gas phase
HEX	heat exchanging fluid
i	component i / inner
j	component j
k	coordinate r,z
lit	literature
n	normal conditions
N	component N
N_2	nitrogen
o	outer
overall	overall coefficient
p	particle
r	radial
Rad	radial
s	surface / solid
tot	total
w	wall

z	axial
α	heat transfer
Δ	triangle
λ	conductive

Superscripts

Symbol	**Description**
*	equilibrium
a	adsorption
diff	free gas diffusion
eq	equilibrium
h	heating
i	component i
Kn	Knudsen
visc	viscous

1 Introduction

The separation of carbon dioxide (CO_2) is a major task in several industrial processes. In cryogenic processes, it is necessary to remove any condensable components to avoid solid plugging in the cryogenic unit [1–3]. CO_2 can also be a catalyst poison and its removal in such processes is mandatory [1]. In addition, there are processes in which it is desirable to recover the CO_2 for subsequent processing, such as Enhanced Oil Recovery [1].

Another important CO_2 capture process that has received increasing attention over the past years is the removal of CO_2 from flue gases emitted by fossil fueled power plants since anthropogenic CO_2 emissions are one of the main causes of global warming. A reduction in emissions is not expected in near future since the economic growth of developed and emerging countries will increase the demand for electricity. The International Energy Agency (IEA) assumes in its New Policies Scenario that an increase of over 70% in the demand for electricity between 2010 and 2035 is expected, with coal remaining the backbone fuel for the generation of electricity [4]. Therefore, concepts such as carbon capture and sequestration (CCS) or carbon capture and use (CCU) have been proposed in recent years [5–7]. The goal of CCS and CCU is to capture approximately 90% of the emitted CO_2 [8], and to recover the separated CO_2 with high purities (>95% [9]) in order to compress and store it, or to use it for another process, and therefore reduce the amount of CO_2 that is released into the atmosphere. In recent years important steps towards a reduction in CO_2 emissions have been made, including the Clean Power Plan [10] and the Paris Agreement in 2015 [11]. Nonetheless, a complete neglect of fossil fuel power plants in the near future is not expected; therefore, CCS and CCU continue to play a major role in the reduction of CO_2 emissions. The costs of carbon capture systems remain high and the reduction of these costs is an essential task for carbon capture development [5, 12].

There are three general routes for capturing CO_2 from fossil fuels power plants: the oxy-fuel combustion, the pre-combustion capture, and the post-combustion capture [13]. Since the oxy-fuel combustion and the pre-combustion routes cannot be retrofitted to existing power plants, which is essential for a reduction in CO_2 emissions, only the post-combustion route can be used for existing fossil fuel power plants [13]. A schematic of the post-combustion route is shown in Figure 1.1.

Amine wash units are considered one of the most suitable technologies for post-combustion capture since this technology is widely used for CO_2 capture in several industrial processes [14–16]. However, the main drawback is its high energetic demand for the solvent regeneration that reduces the power plant efficiency [14]. New developments have reduced the specific energetic requirements to $\approx 2.7\ ^{\mathrm{MJ}}/_{\mathrm{kg_{CO_2}}}$ [17]. This energetic

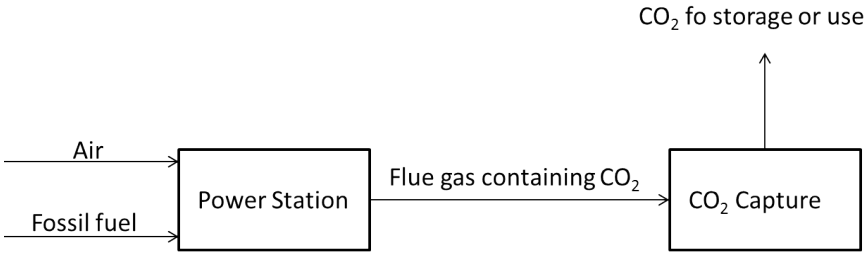

Figure 1.1: Schematic representation of the post-combustion CO_2 capture route.

demand remains high and the development of CO_2 capture technologies with decreased energetic demand is essential in order to reduce the costs of CCS [1]. In addition to the amine wash, other technologies have been proposed for post-combustion CO_2 capture, such as membrane processes or adsorptive processes. The different technologies are presented in the following sections with a focus on the adsorptive processes.

1.1 Absorption processes

Absorption processes can be classified into two categories [1]:

- Physical absorption
- Chemical absorption

For the removal of CO_2, physical absorption processes are generally suitable if the CO_2 partial pressure is high and the temperature is low [1]. On the other hand, if the partial pressure of CO_2 is low and the temperature is relatively high, chemical absorption processes are more suitable [1]. From an energetic perspective, the chemical absorption process is more demanding than the physical absorption process because of the chemical bonds [1]. A schematic representation of the equilibrium characteristics of the physical and chemical solvents are illustrated in Figure 1.2. Since the pressure of the

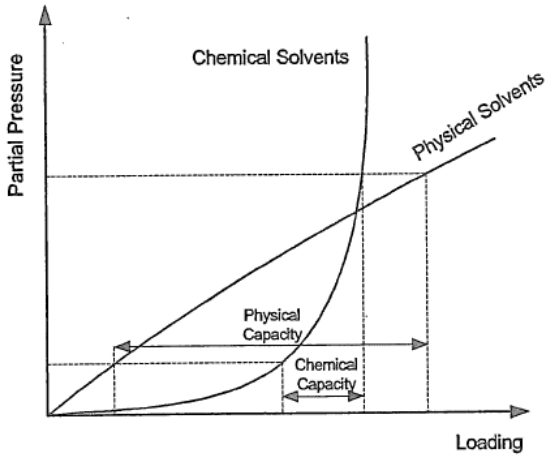

Figure 1.2: Schematic representation of the equilibrium characteristics of physical and chemical absorption taken from [1].

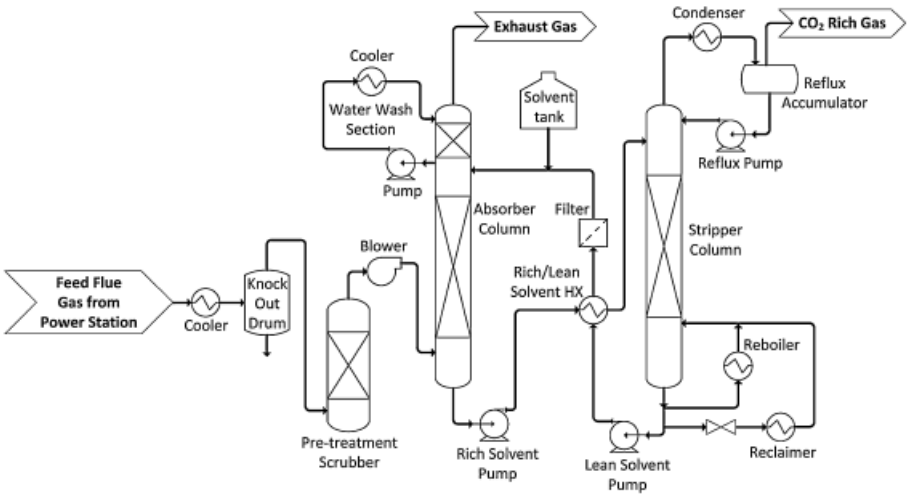

Figure 1.3: Schematic representation of the chemical absorption process using amine solvents taken from [18].

flue gas in the post-combustion capture route is not high, the partial pressure of CO_2 is low. Futhermore, the temperature of the flue gas is high, which makes the chemical absorption process adequate for this separation process, despite the higher energy cost for regeneration. Amine-based solvents are used in chemical absorption processes for separating CO_2. One of the most common used amine solvents is Monoethanolamine (MEA). As a primary amine it has excellent reactivity and absorption capacity [18]. In addition to MEA, Diethanolamine (DEA) or Methyldiethanolamine (MDEA) are often used as amine-based solvents. The chemical absorption process using amine-based solvents consist of two steps: absorption and solvent regeneration. Each step takes place in a different tower. The CO_2 is absorbed into the amine solution in the absorber tower [16]. The loaded solvent is then regenerated in the regenerator by stripping with water vapor at 100°C to 120°C [16], and the water is condensed leading to nearly pure CO_2 [16]. A schematic representation of the chemical absorption process using amine solvents to capture CO_2 is illustrated in Figure 1.3. Since the energetic demand is high during the regeneration step, improvements in process technology and solvent development have recently been topics of research to make CCS feasible [1, 14, 17–20].

1.2 Membrane processes

The principal role of membranes is to separate two components with a thin, semipermeable barrier; the components are separated on the basis of the different rates at which they permeate through this thin barrier. This rate of permeation is driven by a change in chemical potential between both phases, consequently a pressure difference between both phases is required. The separation of CO_2 and nitrogen (N_2) with membranes is not a demanding task since membranes with high selectivity and high permeances have been developed [21]. The problem with CCS is the scale of the processes and the large,

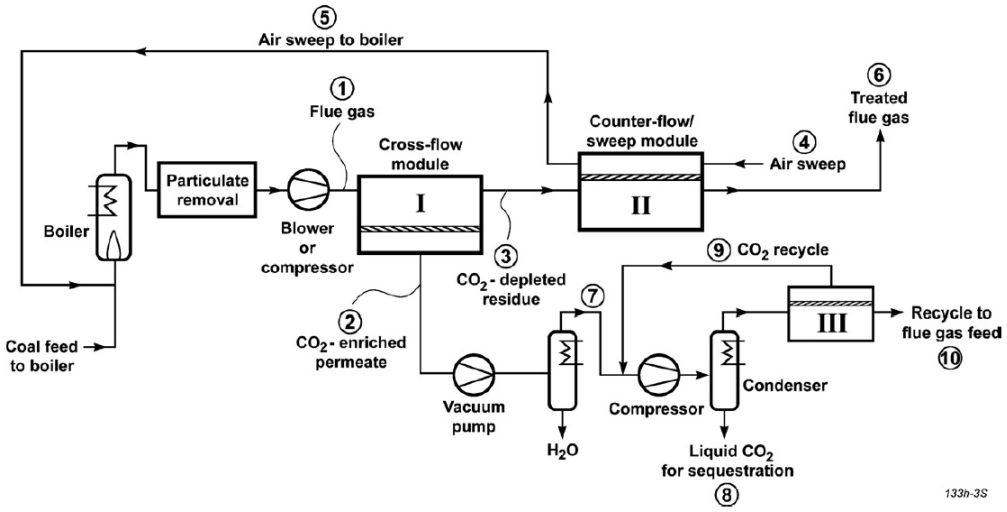

Figure 1.4: Schematic representation of the multi-stage membrane process by Merkel et al. [21].

expensive, and energy consuming compression equipment that is necessary because of the large volume that must be processed [21]. According to Merkel et al. [21], only a pressure ratio of five can be afforded for CCS and it is preferable to use a vacuum on the permeate instead of compressing the feed. They also propose a multi-stage design which incorporates counter-flow/sweep membrane modules in order to make the process for CCS feasible. A schematic representation of the process is shown in Figure 1.4. The necessity of using a vacuum is one of the major limitations of this process.

1.3 Adsorption processes

Adsorption processes can be categorized into Pressure Swing Adsorption (PSA) processes and Temperature Swing Adsorption (TSA) processes. To regenerate the adsorbent a pressure difference is used in PSA processes, whereas in TSA processes the temperature is increased. Both processes have been investigated as potential technologies for CCS.

1.3.1 Pressure Swing Adsorption

The pressure difference that is required for the PSA process can either be achieved by compression of the feed or by the use of a vacuum during the regeneration step. Since the volume flow treated for CCS is large, a vacuum for regeneration is usually preferred instead of compression of the feed, similar to the membrane processes. This process is also referred as the Vacuum Swing Adsorption (VSA) process. A schematic representation of a VSA process for CO_2 capture is illustrated in Figure 1.5. Despite significant research on VSA processes for post-combustion CO_2 capture in recent years [22–26], the VSA process has the same major drawback as the membrane process: the necessity of the use of a vacuum.

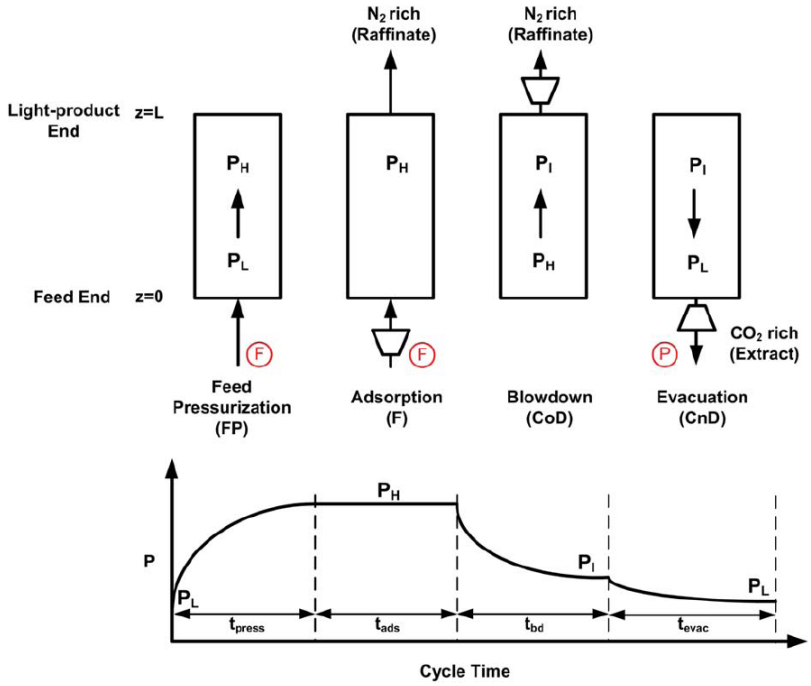

Figure 1.5: Schematic representation of a VSA process taken from [22].

1.3.2 Temperature Swing Adsorption

TSA processes are usually applied to remove trace components, because of the long cycle times. Since the component that must be separated binds strongly to the sorbent in the TSA process, high purities of the product stream can be achieved. A hot regeneration gas is often used to regenerate the sorbent, meaning a direct heating of the bed is used. A schematic representation of a classical TSA process is illustrated in Figure 1.6. Since adsorption is an exothermic process, heat is released during the adsorption step. If the amount of impurities that must be removed is not large, the increase in temperature will not have a negative impact on the process. Nevertheless, considering the removal of CO_2 from a flue gas, a large amount must be removed which leads to a negative impact on the process due to the temperature increase. This limits the application

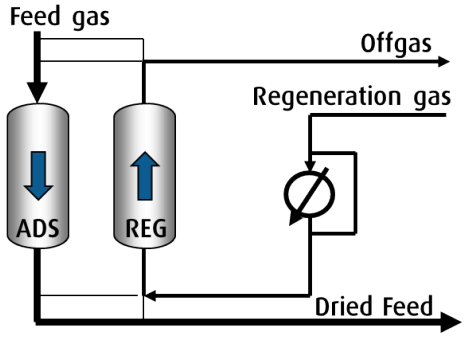

Figure 1.6: Schematic representation of a TSA process.

of the classical TSA process for the capture of CO_2 from flue gas. Another drawback of the classical TSA process for CO_2 capture from flue gas is direct heating with a regeneration gas during the regeneration step, since the recovered CO_2 is diluted. To overcome these limitations, indirect heated and cooled TSA processes were developed. The advantages of these processes are that the heat of adsorption can be removed during the adsorption step, which allows higher capacities, and, because of the indirect heating of the sorbent bed, the recovered CO_2 is not diluted [13, 27]. In the next sections two promising indirectly heated and cooled TSA processes are presented.

1.3.2.1 Hollow fibers as heat exchangers

Lively et al. [13, 28–30] developed hollow fibers that are impregnated with 13X zeolite crystals and have an impermeable inner lumen layer. Since the bore is sealed with the lumen layer, this concept is similar to a shell and tube heat exchanger. The concept of the hollow fibers is illustrated in Figure 1.7. They proposed to use this concept to capture CO_2 from flue gas. One of the advantages of this concept is the low thermal resistance through the fibers since they are thin. This low thermal resistance allows for the achievement of fast cycles. Therefore, higher throughputs and smaller units can be envisioned. Since the flue gas is saturated with water, a dehydration unit would be necessary in order to avoid a negative impact on the CO_2 capacity of 13X. In order to process a saturated flue gas, the workgroup developed amine supported hollow fibers [31–35] since they can tolerate the presence of water. The idea of using amine groups is derived from amine-based solvents that are used for chemical absorption. Another advantage of this concept is the possibility of recovering heat since the heat of adsorption can be captured by the cooling fluid and used to heat the module that requires heat.

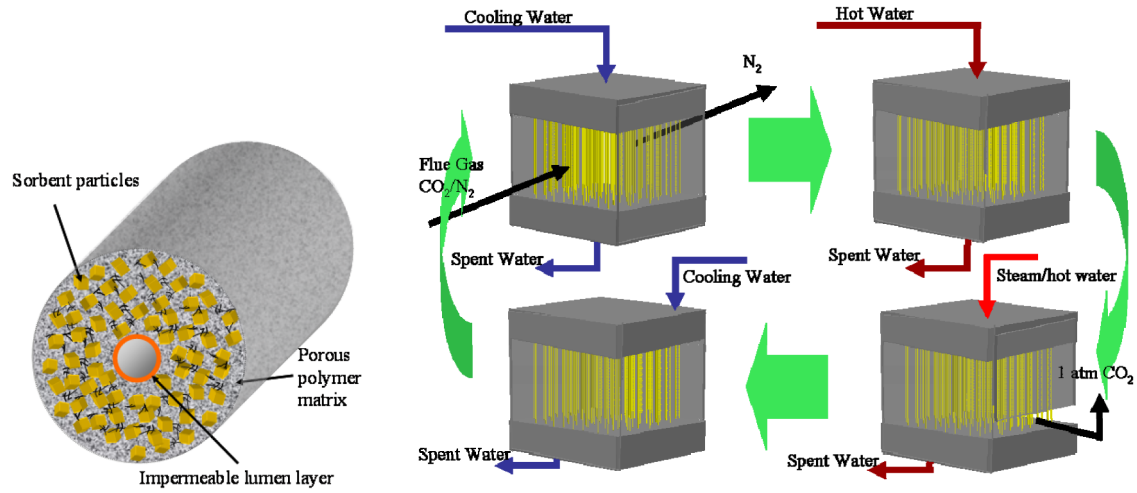

(a) Hollow fiber with impermeable lumen layer.

(b) CO_2 capture concept.

Figure 1.7: Hollow fiber heat exchangers for CO_2 capture taken from [13].

Although this is a promising concept in the short-term, one cannot expect this concept to be ready for industrial scale since there are still issues that must be resolved, such as its economical scalability, since a large volume has to be treated for CCS.

1.3.2.2 Classical heat exchanger concept

In this case, concepts that are similar to heat exchangers, such as a shell and tube heat exchanger or plate fin heat exchanger, are proposed. Fillipi [27] and Jain [36] postulated the use of indirect heated TSA processes based on a heat exchanger to capture CO_2. The workgroup around Francis Meunier and Shivaji Sicar also postulated a concept based on shell and tube heat exchangers. In the following section, the concepts of Meunier and Sircar are described in detail.

Coaxial heat exchanger with fins

Bonjour et al. [37] describe a TSA process that consists of two coaxial tubes. The outer tube is filled with adsorbent whereas the inner tube is used to pass a cooling or heating media. In order to increase the heat transfer, the inner tube is equipped with fins on the outer surface; a representation of the system is illustrated in Figure 1.8. This concept was first developed for the removal of volatile organic compounds. Merel et al. [38, 39] investigated the application of this concept for CO_2 capture from flue gas, and they

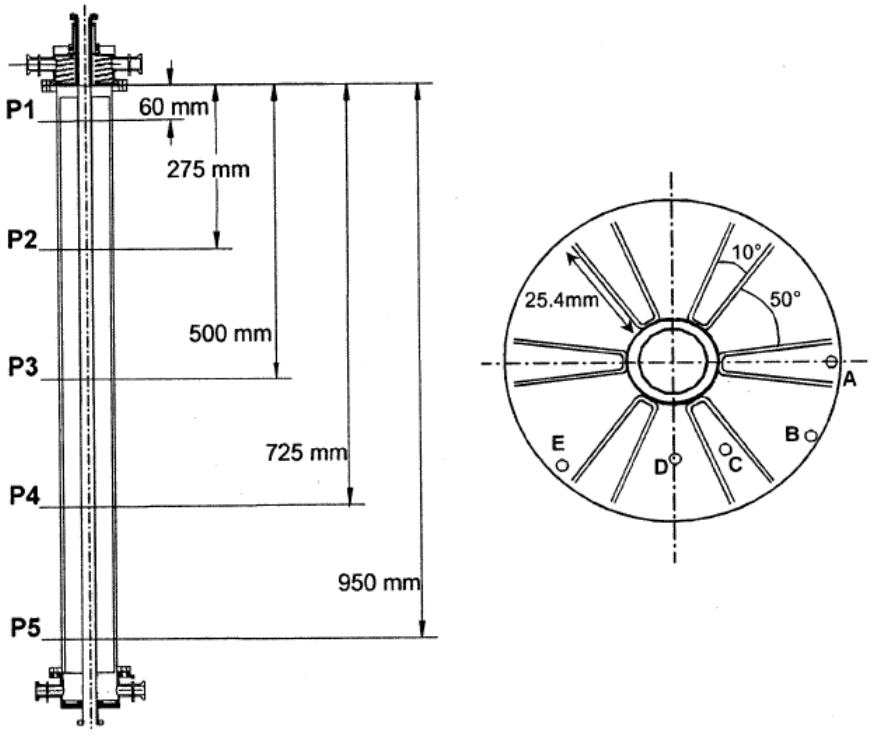

Figure 1.8: Indirect heated and cooled process proposed by Bonjour et al [37].

were able to obtain specific energy consumptions of around 6 $^{MJ}/_{kg_{CO_2}}$ and CO_2 purities $\geq 94\%$ in their experimental setup. The specific energy demand is higher than that of the chemical absorption process using amine based solvents. Nevertheless, they assumed that their concept would have an energy demand of approximately 4.5 $^{MJ}/_{kg_{CO_2}}$ on an industrial scale. Clausse et al. [40] later showed in a numerical study that the energy consumption could be decreased to 3.23 $^{MJ}/_{kg_{CO_2}}$ with a recovered CO_2 purity near 95% and a CO_2 recovery of approximately 81%.

This concept has some drawbacks. First, fins are required in order to increase the heat transfer from the heating media to the adsorbent, since the adsorbent has a low thermal conductivity. This would increase the capital costs. Second, since non conventional tubes are used the scalability of this concept can be considered as a drawback.

Shell and tube heat exchanger

Sircar proposed the use of a shell and tube heat exchanger type adsorber for the removal of water and other impurities from air [3]. In this case, the adsorbent is filled inside the tubes and to regenerate the bed, a hot heat exchanging fluid is passed through the shell of the tube bundle. To cool the tube bundle, a cold heat exchanging fluid is passed through the shell; a schematic representation of his concept is illustrated in Figure 1.9. Lee and Sircar [41] and Beaver and Sircar [42] proposed the use of the shell and tube heat exchanger type adsorber for the removal of CO_2 from flue gas. They used an Na_2O promoted alumina as a reversible CO_2 selective chemisorbent. During regeneration, they used a heating medium to indirectly heat the bed. The pressure inside of the tubes is increased due to the increase in temperature since all of the valves are closed. After

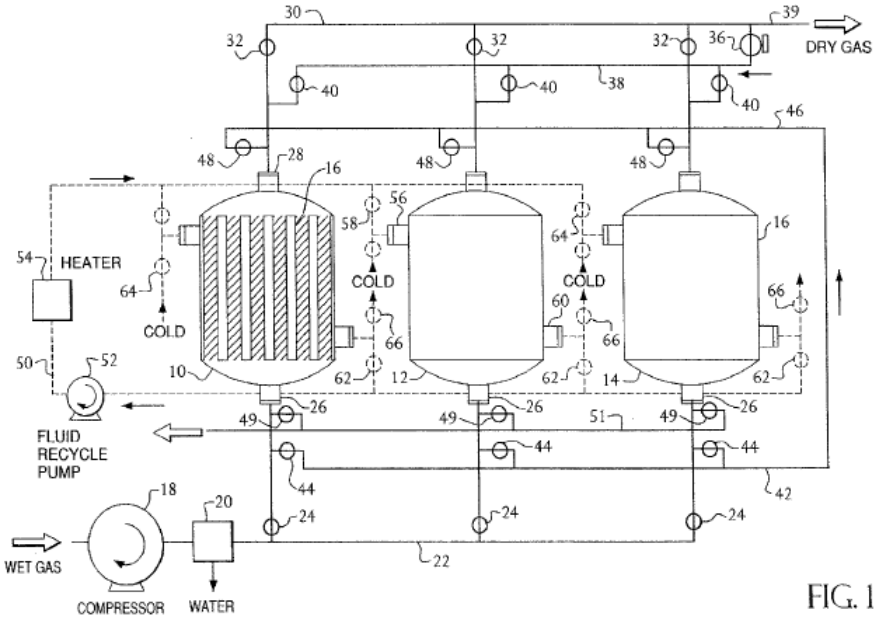

Figure 1.9: Indirect heated and cooled process proposed by Sircar [3].

a certain pressure was reached, they used a high pressure steam to purge the vessel. Subsequently, the steam was condensed leading to nearly pure CO_2. Advantages that they claim are that the feed gas does not have to be dried since the adsorbent is not water sensitive, and that CO_2 can be recovered at high pressures, which reduces the compression work afterwards in CCS. They also claim to achieve a high CO_2 purity of approximately 99% and recoveries near 93% with a steam requirement of ≈ 0.44 tons of high pressure steam per tons of CO_2 product gas and ≈ 3.06 tons of low pressure steam per tons of CO_2 product gas.

One of the drawbacks of this concept is the need for high temperatures for regeneration, since this could lead to a requirement for special materials that would increase the capital costs. Furthermore, the use of high pressure steam would lead to a reduction in the efficiency of the power plant. The fact that non-conventional adsorbents are used is another drawback because of their availability and cost. Nevertheless, this concept represents a process that is viable over the short-term, since it combines two known unit operations: shell and tube heat exchanger or tube bundle reactors and TSA.

1.4 Motivation and goal of this work

Indirect heated and cooled adsorption processes represent a promising alternative to CO_2 capture since they do not require a vacuum or chemical solvents. They also offer the possibility of recovering and integrating heat since in this case, one degree of freedom is available compared to classical TSA. The shell and tube heat exchanger type adsorber combines two state of the art unit operations: heat exchanger and TSA, which makes it viable over the short-term. Nevertheless, a deeper understanding of this process is required in order to design a techno-economical process, which is important for CO_2 capture from flue gas. This is also one of the goals of this work, as well as the derivation of a detailed mathematical model which is required for process design.

This work shall contribute to the investigation of the heat transfer characteristics of beds that are packed with typical industrial sorbents, and to the adsorption and desorption characteristics of an indirectly heated and cooled TSA process. Therefore, an experimental setup was used to investigate the heat transfer with and without convection in a tube that was packed with a typical industrial sorbent; this tube could be heated and cooled indirectly. In addition, adsorption experiments were conducted using this experimental setup. Important parameters/properties were determined using the experimental setup in order to use them in the detailed numerical model that was developed for modeling the indirect heated and cooled TSA process with heat integration and heat recovery routines. Lastly, a numerical study using the obtained parameters was conducted in order to prove the applicability of this concept to CO_2 capture.

1.5 Proposed process for CO_2 capture

Similar to PSA or standard TSA processes, a minimum of two adsorbers is required in order to deliver purified feed gas continuously. Depending on the quantity of gas that has to be processed and the given boundary conditions, process schemes with more adsorbers are possible. In this work, the separation process that is considered consists of three tube bundle adsorbers with indirect heating and cooling. A schematic representation of the process can be observed in Figure 1.10. Three vessels are used in order to reduce the energetic demands of the process by heat integration. In addition, the cycle time can be reduced using three vessels. Therefore, this three-adsorber concept represents the basic case for the indirect heated adsorption process with heat integration. Each of the adsorber vessels undergoes three different steps: adsorption, heating/desorption, and cooling+pressurization. A schematic representation of the process scheme can be seen in Figure 1.11. During the adsorption step, the feed gas enters the adsorber vessel. The adsorptive is preferably adsorbed by the adsorbent material and an almost adsorptive free stream leaves the adsorber. A heat transfer fluid passes through the shell of the vessel in a co-current manner in order to remove the adsorption heat. After the bed is fully loaded with the adsorptive, the heating/desorption step begins. The outlet heat transfer fluid of the vessel that is in the cooling+pressurization step, after passing through a heat exchanger, passes through the shell of the vessel in order to indirectly heat the adsorbent bed. Therefore, the heat stored in the vessel that is in the cooling+pressurization step is used to heat the vessel that is currently in the heating/desorption step. The adsorptive begins to desorb because of the temperature

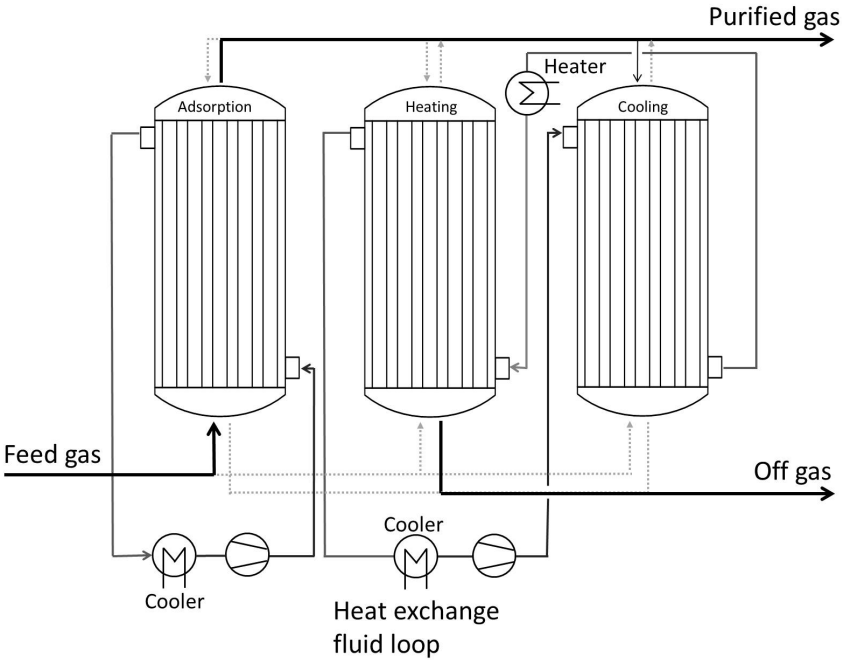

Figure 1.10: Schematic representation of the separation process using a tube bundle adsorber with indirect heating and cooling.

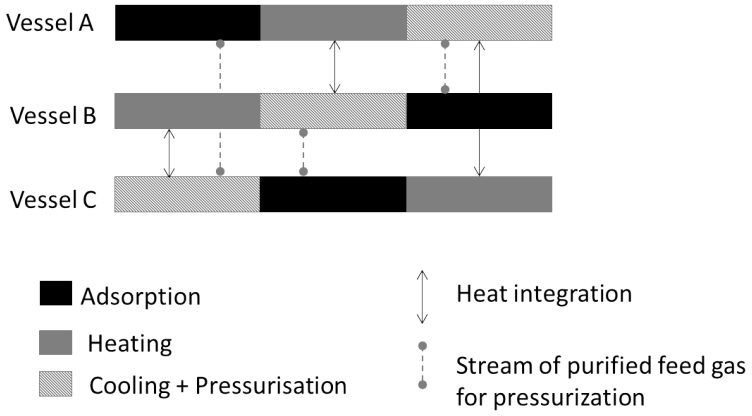

Figure 1.11: Schematic representation of the process scheme.

increase. After the heating/desorption step, the adsorbent bed is cooled. For this purpose, the outlet heat transfer fluid of the vessel that is in the heating/desorption step, after passing through a heat exchanger, is sent through the shell of the vessel. Therefore, heat integration between the vessel that is in the heating/desorption step and the vessel that is in the cooling+pressurization step is achieved. Furthermore, a small stream from the purified feed gas is used to pressurize the vessel. This is necessary since the temperature drop of a closed vessel would cause a pressure drop during the cooling step.

2 Theory

The theoretical background for the investigation of the indirectly heated and cooled adsorption process will be exposed. Special focus will be set on the heat transfer in packed beds and the mathematical description of the indirect heated adsorption process. Also, the methods applied for parameter estimation and general concepts of adsorption will be exposed .

2.1 Adsorption

The following sections will introduce the fundamentals for understanding an adsorption process. Besides the thermodynamic and kinetic theory of adsorption the type of adsorbent used in this work will be presented. More detailed information can be found in [43–47].

2.1.1 Fundamentals of physical adsorption

Physical adsorption is a process in which molecules, also called adsorptives, are bonded on the surface of a highly porous solid, which is called the adsorbent. If the molecule is bonded to the adsorbent then it is called adsorpt. The complex build by the adsorbent and the adsorpt is known as adsorbate. The reverse process of adsorption is desorption. In this process a bonded molecule is released from the adsorbent. A schematic representation of adsorption and its different phases is illustrated in Figure 2.1.

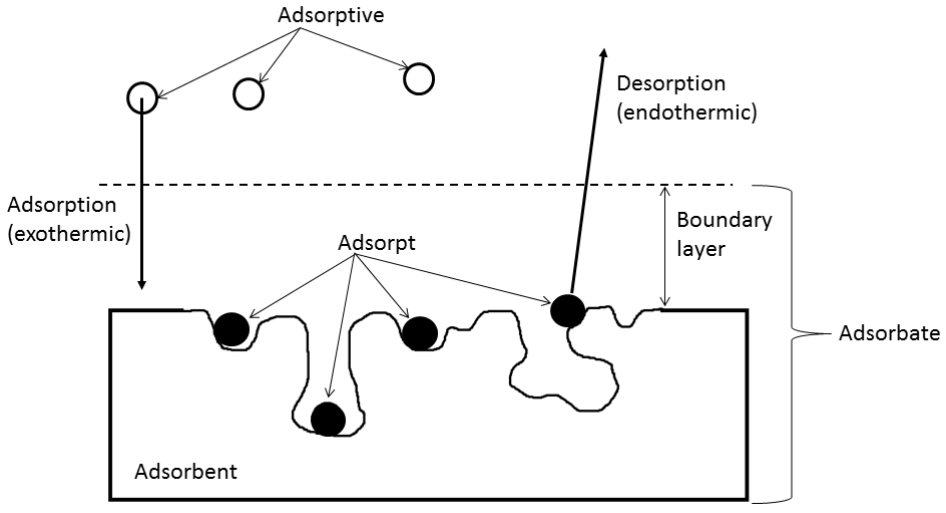

Figure 2.1: Schematic representation of adsorption and its different phases according to [43].

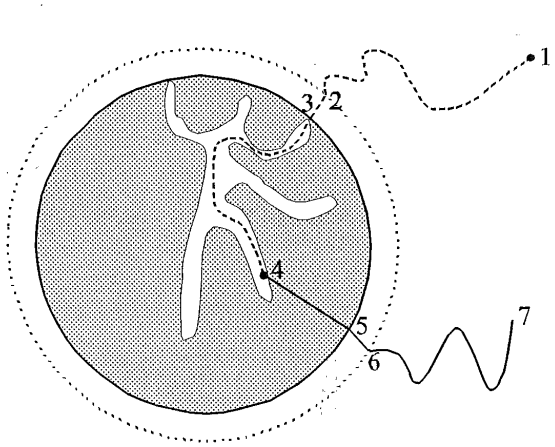

Figure 2.2: Schematic of the different adsorption process steps taken from [43].

The following description is based on Bathen and Breitbach [43]. The adsorption and desorption process is a very complex combination of different mass and heat transport phenomena. In general, the process can be divided in seven steps as is illustrated in Figure 2.2. In the first step (1→2) the adsorptive is transported by diffusive and convective mechanisms to the outer boundary layer. An actual boundary layer does not exist, but it is considered as an auxiliary conception for the modeling [43]. After the adsorptive has reached the boundary layer it will diffuse through it (2→3) before entering the pores. Inside the pores several diffusive mechanisms will take place (3→4). Once in the pores adsorption will take place (4). Since adsorption is an exothermic process, there is a heat transport from the pores to the bulk phase. Inside the adsorbent the heat is transported through conduction from the pores to the surface of the adsorbent (4→5). Similar as for the mass transport the heat is transported through the outer boundary layer through conduction (5→6). The last step is the transportation of heat from the boundary layer to the fluid, which occurs in a similar matter as the mass transport, namely by convection and conduction (5→6).

Like for all thermal separation processes, the driving force for adsorption is a disturbance of the equilibrium. The system will tend to reach a new equilibrium state. While the thermodynamics will dictate in which direction the system will tend to the kinetics will determine the velocity of this change. Both aspects will be presented in the following sections after having introduced the family of adsorbents used in this work, since the adsorbent plays a major role in the design of adsorption processes.

2.1.2 Zeolites

Zeolites are aluminosilicates with a defined lattice structure and in general with exchangeable alkali or earth alkali cations. The primary building unit of these structures are crystalline $[AlO_4]^{5-}$ and $[SiO_4]^{4-}$ tetrahedrons. The two most common unit cells,

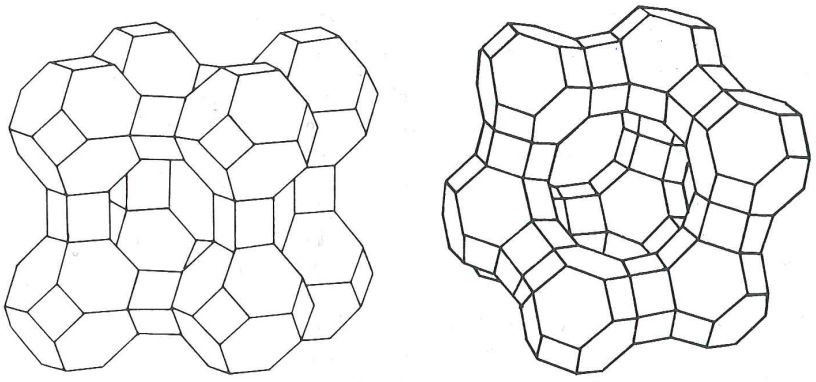

(a) Type A (b) Type X and Y

Figure 2.3: Different zeolite crystal structures taken from [45].

built from these tetrahedrons are the zeolite crystal type A and the zeolite crystal type X and Y. A schematic illustration of these zeolite crystals can be seen in Figure 2.3. One can observe from Figure 2.3, that the crystal build by the tetrahedrons contains cages which can be differentiated into larger α-cages and smaller β-cages [47, 48]. The openings to the cages of the zeolite crystal type A are around 0.3-0.5 nm and the ones for type X and Y around 0.7-0.75 nm [43]. Therefore the openings of these structures act as sieves. This is the reason why zeolites are often called molecular sieves since only those molecules which have a molecular diameter small enough to get through the openings can be adsorbed. Since the metal cations are exchangeable the openings of the zeolites can be modified. For example, if Na-cations are exchanged by K-cations the openings can be reduced from 0.42 nm to 0.3 nm [45]. In Table 2.1 the typical effective pore diameter (opening) for different zeolites is listed.

Table 2.1: Effective pore diameters for different zeolites taken from [45].

Structure type	Cation	effective pore diameter (nm)
A	Na^+	0.42
A	Ca^{2+}	0.5
A	K^+	0.38
X	Ca^{2+}	0.8
X	Na^+	0.9-1
Y	Na^+	0.9-1

2.1.3 Adsorption thermodynamics

The thermodynamics fundamentals of adsorption were postulated by Gibbs in 1876 [43]. He based his concept on the assumption, that the three phase system (adsorbent, adsorbate, and fluid phase) can be thermodynamically reduced to a two phase system (adsorpt and fluid phase) [43]. This reduction will allow an analogy to the thermodynamics of liquid-gas mixture [43]. The thermodynamic equilibrium is then given if the specific free enthalpy of both phases is equal [43]:

$$\mathrm{d}g_{\mathrm{Adsorpt}} = \mathrm{d}g_{\mathrm{fluid}}$$

From this equality a theoretical adsorption isotherm, also called the Gibbs-Isotherm can be derived [43]. But it was Langmuir who at first derived an actual adsorption isotherm based on a physical model [45].

2.1.3.1 Langmuir adsorption isotherm

The Langmuir adsorption isotherm is based on the following assumptions [43]:

1.) adsorption sites are energetically uniform

2.) all adsorption sites can be occupied

3.) there is no interaction between the adsorbed molecules

4.) there is only a mono-layer coverage of the adsorbent surface

5.) ideal gas is considered

From the equilibrium condition, which implies that the adsorption and desorption rates are equal, the following correlation can be derived [43]:

$$q_{\mathrm{i}}^{\mathrm{eq}} = q_{\infty} \frac{b(T) \cdot p_{\mathrm{i}}}{1 + b(T) \cdot p_{\mathrm{i}}} \tag{2.1}$$

An exemplary Langmuir adsorption isotherm at different temperatures is illustrated in Figure 2.4. Besides the classical Langmuir adsorption isotherm, extensions of this isotherm, e.g. the dual site Langmuir isotherm [49–51], have been used to fit experimental measurements. The dual site Langmuir isotherm can be written as follows [49]:

$$q_{\mathrm{i}}^{\mathrm{eq}} = q_{\infty,1} \frac{b_1(T) \cdot p_{\mathrm{i}}}{1 + b_1(T) \cdot p_{\mathrm{i}}} + q_{\infty,2} \frac{b_2(T) \cdot p_{\mathrm{i}}}{1 + b_2(T) \cdot p_{\mathrm{i}}} \tag{2.2}$$

2.1.4 Adsorption kinetics

Adsorption kinetics will give information about the rate of the change. The steps that are connected to the adsorption process kinetic are the mass transfer through the boundary layer (step 2→3 in Figure 2.2), the mass transport to the pores (step 3→4 in Figure 2.2), and the adsorption itself [43]. Since the adsorption step is very fast [43] it

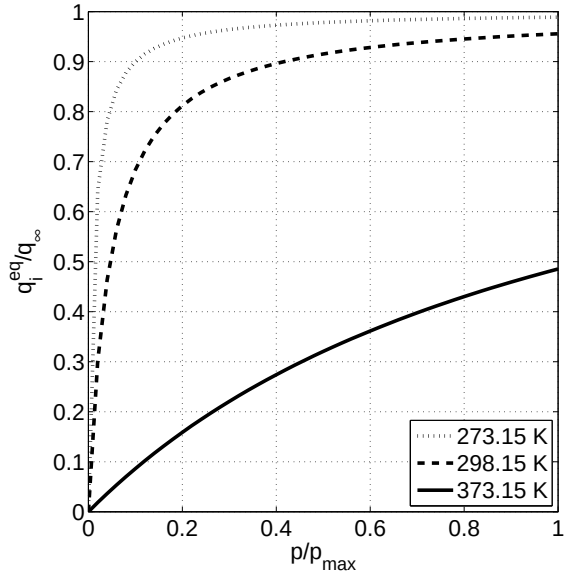

Figure 2.4: Schematic Langmuir adsorption isotherm at different temperatures.

can in general be neglected as the rate limiting step. Therefore the limiting step would be either the outer mass transfer or the internal mass transfer. In general the internal mass transfer can be assumed to be the limiting step in packed beds under typical industrial conditions [43]. The internal mass transfer can be described by different mechanisms with:

- viscous flow
- Knudsen diffusion
- free pore diffusion

being the most common mechanisms for gas adsorption (neglecting the surface diffusion) [43]. The internal mass transfer can be modeled using Fick's law [43, 45, 52]:

$$\dot{m} = -D^i \cdot a_{\text{spec}} \frac{\partial Y}{\partial r} = -D^i \cdot a_{\text{spec}} \frac{M}{\mathbb{R} \cdot T} \frac{\partial p}{\partial r} \tag{2.3}$$

with D^i being the corresponding diffusion coefficient and $\frac{\partial Y}{\partial r}$ or $\frac{\partial p}{\partial r}$ being the driving force for mass transport.

A viscous flow will be present if the pores of the adsorbent are subjected to an external pressure change [43]. In this case a laminar flow will exist in the pores larger than the mean free path of the molecules [43]. The mass transfer can then be described by the law of Hagen-Poisseuille which leads to the following correlation for the diffusion coefficient [45]:

$$D^{\text{visc}} = \frac{p \cdot d_{\text{pore}}^2}{32 \cdot \eta_{\text{g}} \cdot \mu_{\text{p,diff}}^{2.6}} \tag{2.4}$$

with η_g being the dynamic viscosity and $\mu_{p,diff}$ being the tortuosity for free gas diffusion.

If the pores are smaller than the mean free path of the molecules, which would be the case for a Knudsen number higher than 10 (Kn > 10) then the governing mechanism is Knudsen diffusion [43]. In this case the impact between the molecules and the wall of the pores dominate the mass transfer [43]. The resulting diffusion coefficient can be written for Knudsen diffusion as [45]:

$$D^{Kn} = \frac{4}{3}\frac{d_{pore}}{\mu_{p,diff}^{1.7}}\sqrt{\frac{\mathbb{R}\cdot T}{2\cdot\pi\cdot M}} \tag{2.5}$$

Free pore diffusion will be the existing mechanism if the Knudsen number is lower than 0.1 (Kn<0.1) which means that the pores are larger than the mean free path of the molecules [43]. The impact between the molecules will then dominate the mass transport [43]. The diffusion coefficient for this mechanism can be postulated as follows [45]:

$$D^{diff} = \frac{D_{i,N}}{\mu_{p,diff}} \tag{2.6}$$

with $D_{i,N}$ being the binary diffusion coefficient, which can be calculated for example, using the correlation of Fuller [53]:

$$D_{i,N} = \frac{1\cdot 10^{-3}\cdot T^{1.75}\sqrt{1/M_i + 1/M_N}}{p(V_{Di}^{1/3} + V_{DN}^{1/3})^2} \tag{2.7}$$

where the temperature T has to be in K, the molecular weights M_i and M_N in $^{g}/_{mol}$ the pressure p in atm and the atomic diffusion volumes V_{Di} and V_{DN} in cm^3.

In general, it is very difficult to define which mechanism is the dominating one especially at the transitions. The diffusion coefficient at the transition from Knudsen diffusion to free pore diffusion can be calculated using the following correlation [43]:

$$D_{overall,1} = \left(\frac{1}{D^{Kn}} + \frac{1}{D^{diff}}\right)^{-1} \tag{2.8}$$

which is also known as the Bosanquet equation [48] and for the transition between viscous flow and Knudsen diffusion [43]:

$$D_{overall,2} = D^{Kn} + D^{visc} \tag{2.9}$$

2.1.4.1 Linear-driving-force model (LDF-model)

Homogenous models for describing the kinetics are often used, since in industrial processes the dominating mechanism is not usually known [43]. Also, if the radial concentration of the adsorbent particle would be considered the numerical complexity would be increased [45, 54]. In the homogeneous model the concentration inside the adsorbent is assumed as radial independent and the entire mass transfer resistance is set at the boundary layer:

$$\frac{\partial q_\mathrm{i}}{\partial t} = k_{\mathrm{LDF,i}} \left(q_\mathrm{i}^{\mathrm{eq}}(p_\mathrm{i}) - q_\mathrm{i}(p_\mathrm{i}^*) \right) \tag{2.10}$$

A schematic representation of the model can be seen in Figure 2.5. This model is also known as the Linear-Driving-Force (LDF) model. The LDF-model is widely used in industry [43] and represents a suitable option for modeling the adsorption kinetics. The mass transfer coefficient k_{LDF} can be postulated as follows [48]:

$$k_{\mathrm{LDF,i}} = 15 \frac{D_{\mathrm{eff,i}}}{r_\mathrm{p}^2} \tag{2.11}$$

with the effective diffusion coefficient $D_{\mathrm{eff,i}}$ as [43, 45]:

$$D_{\mathrm{eff,i}} = \frac{D_{\mathrm{overall,1}}}{1 + \dfrac{\rho_\mathrm{p}}{\epsilon_\mathrm{p}} \dfrac{\partial q_\mathrm{i}^{\mathrm{eq}}}{\partial c_\mathrm{i}}} \approx \frac{D_{\mathrm{overall,1}}}{\dfrac{\rho_\mathrm{p}}{\epsilon_\mathrm{p}} \dfrac{\partial q_\mathrm{i}^{\mathrm{eq}}}{\partial c_\mathrm{i}}} \tag{2.12}$$

The approximation of equation 2.12 derives from the thought that the amount of the molecules in the void space of the pores is negligible compared to the amount adsorbed on the solid phase [45]. Over the years, several authors have studied the validity of the LDF-model and also postulated modified LDF-coefficients [50, 55–57]

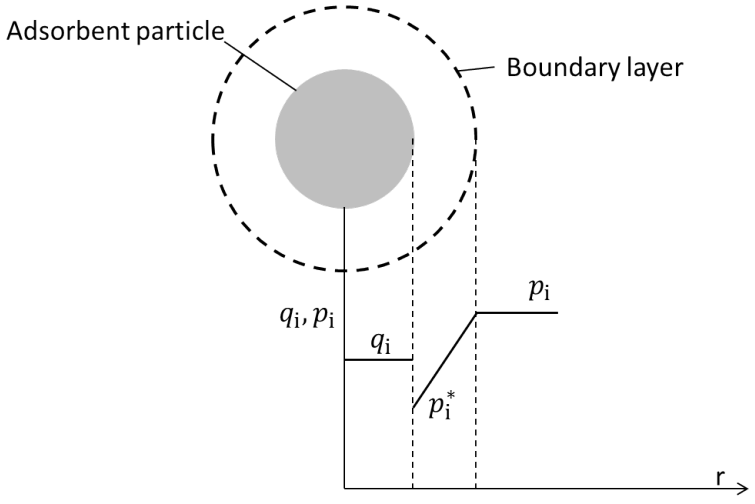

Figure 2.5: Schematic representation of the homogeneous kinetic model (LDF-model).

2.1.5 Adsorption dynamics

Information about the adsorption dynamics can be obtained by breakthrough curves. A typical breakthrough curve can be observed in Figure 2.6. The slope of the breakthrough curve is influenced by the adsorption thermodynamics and the adsorption kinetics.

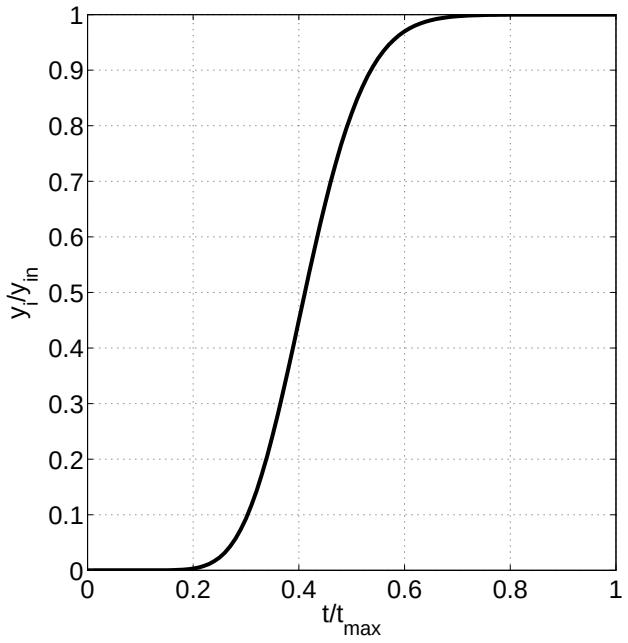

Figure 2.6: Typical breakthrough curve.

2.1.5.1 The impact of adsorption thermodynamics

If the equilibrium theory is assumed, which implies that the adsorption kinetics is fast, dispersive effects are neglected, and isothermal conditions and a constant velocity are assumed, the following correlation can be postulated for the concentration front velocity [45]:

$$u_{\mathrm{conc}} = \frac{u_0/\epsilon}{1 + \dfrac{1-\epsilon}{\epsilon}\rho_{\mathrm{p}}\dfrac{\partial q_{\mathrm{i}}^{\mathrm{eq}}}{\partial c_{\mathrm{i}}}} \tag{2.13}$$

The concentration velocity is inverse proportional to the slope of the adsorption isotherm, which implies that as the slope increases, the concentration front velocity slows. If the isotherm is linear, the concentration profile will be a step traveling through the vessel. On the other hand, if a Langmuir isotherm is considered, which has a large slope at the beginning but decreases and tends to zero when saturation is reached, the shape of the traveling front will change across the bed. This occures because for lower concentrations the slope is high and the velocity will be decreased, whereas for higher concentrations the velocity will be increased since the slope is lower. This would lead to

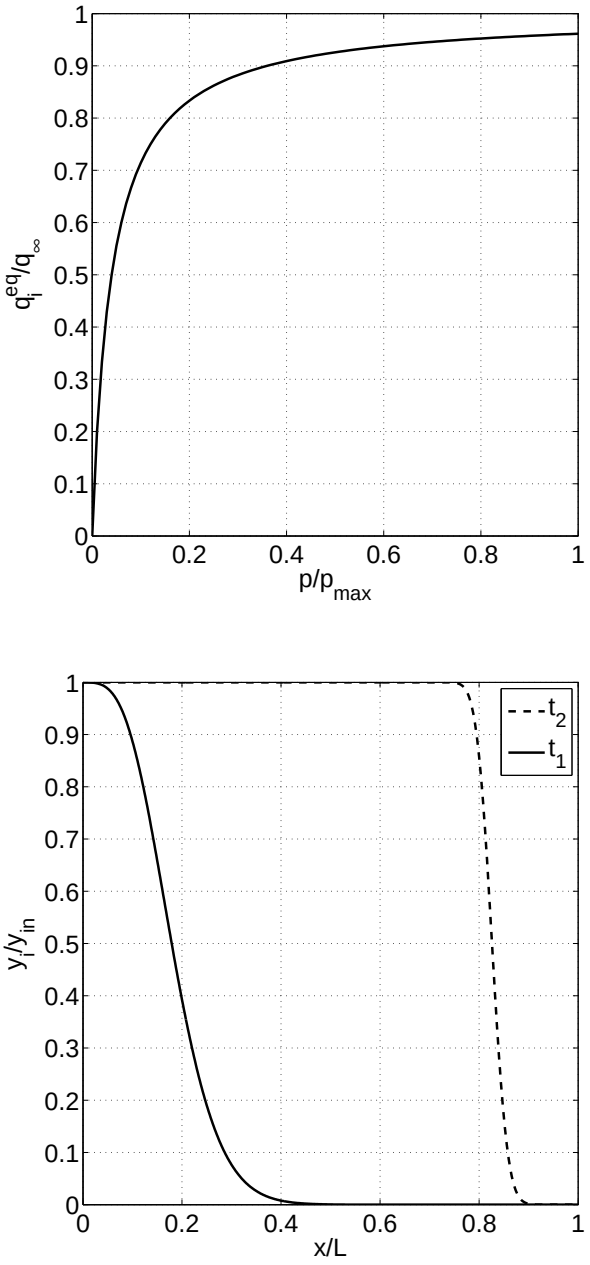

Figure 2.7: Self sharpening effect when a Langmuir-isotherm is considered ($t_2 > t_1$).

a self-sharpening effect since the velocity of the higher concentrations is faster than the velocity for the lower concentrations. A schematic representation of the self-sharpening effect when a Langmuir isotherm is considered is shown in Figure 2.7.

2.1.5.2 The impact of adsorption kinetics

If the mass transfer resistance is increased, then it is expected that the mass-transfer-zone (MTZ) will increase, which would lead to flatter breakthrough curves. On the other hand, if the mass transfer resistance is decreased (faster kinetics), a smaller MTZ is

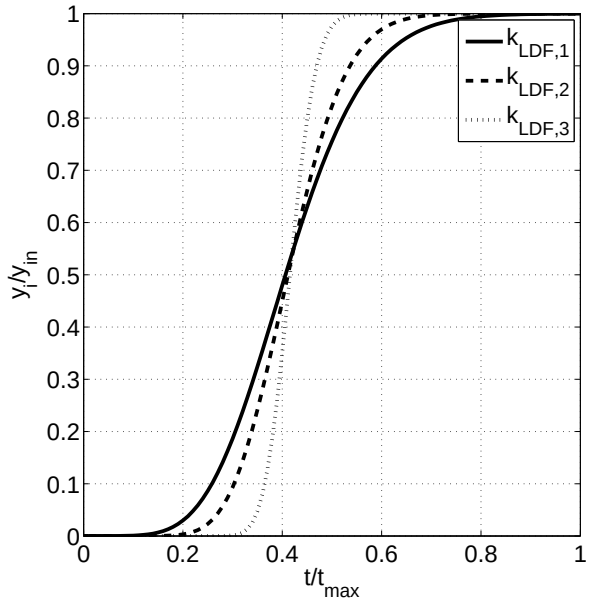

Figure 2.8: Influence of the kinetic on the breakthrough curve ($k_{\mathrm{LDF},1} < k_{\mathrm{LDF},2} < k_{\mathrm{LDF},3}$). The lower the kinetic factor (higher mass transfer resistance) the flatter the breakthrough curve.

expected, which would lead to sharper breakthrough curves. This is also observed in Figure 2.8 where breakthrough curves that were obtained by using different kinetic parameters are plotted.

2.2 Heat transfer in packed beds

Heat transfer in packed beds has been a topic of investigation for several decades. The complex morphology of the investigated system makes it difficult to understand all of the physical phenomena that occur in packed beds. This is reflected in the modeling of packed beds since several models have been postulated. In general, the modeling of heat transfer in packed beds can be divided in two groups [58], discreet models and continuum models, as shown in Figure 2.9. The idea of the discreet models is to describe the bed as a multidimensional network of perfectly stirred tanks [59, 60], which makes these models very flexible [58]. Nevertheless, not all of the model parameters can be derived theoretically and experimental measurements are therefore required [58].

Continuum models, on the other hand, treat each phase, fluid and solid, as a continuum, which allows for the use of Fourier's law to describe the conductive heat transfer [61]. The heat conduction coefficient of these phases must be seen as an effective coefficient. As shown in Figure 2.9, continuum models can also be divided into two groups: homogeneous models and heterogeneous models. Heterogeneous models treat each phase individually, meaning that the gas phase and the solid phase are modeled separately. Homogeneous

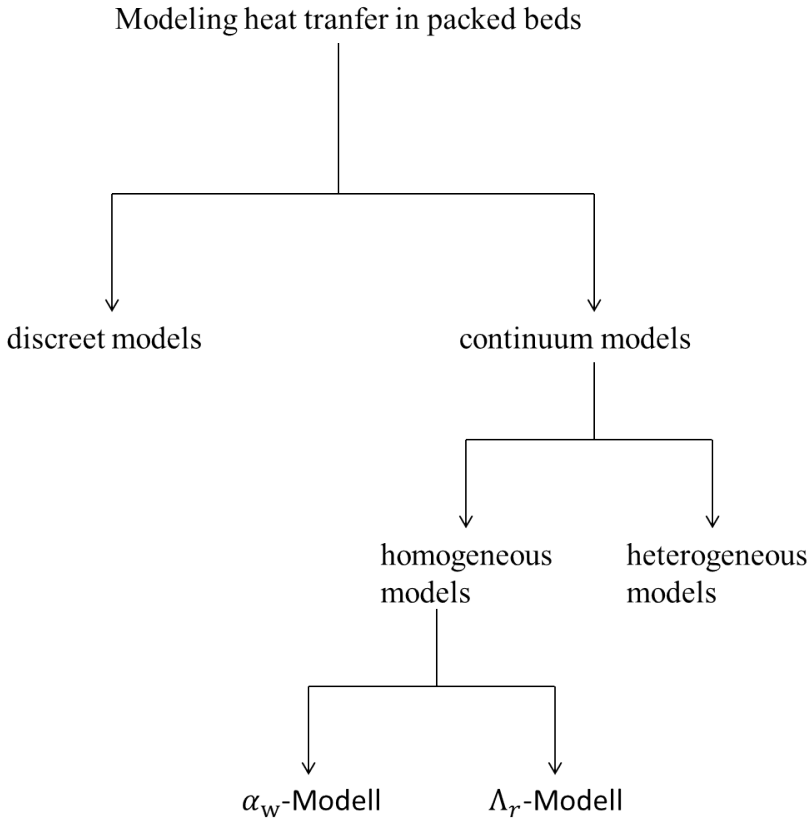

Figure 2.9: Most common models for the description of heat transfer in packed beds.

models on the other hand, do not differentiate between the solid and gas phases; thus, they assume thermal equilibrium between both phases [62].

2.2.1 Heterogeneous model

The heterogeneous model considers both phases individually and couples them through heat transfer from one phase to the other. Since the axial heat conduction can be neglected in wall heated or cooled packed bed tubes [58, 63–65], the following simplified energy balance at stationary conditions can be derived [58]:

Fluid

$$\Lambda_{r,\mathrm{f}}\left(\frac{1}{r}\frac{\partial T_\mathrm{f}}{\partial r}+\frac{\partial^2 T_\mathrm{f}}{\partial r^2}\right)-a_s\alpha_{\mathrm{f,s}}\left(T_\mathrm{f}-T_\mathrm{s}\right)=u_0\rho_\mathrm{f}c_{\mathrm{p,f}}\frac{\partial T_\mathrm{f}}{\partial z} \tag{2.14}$$

Solid

$$\Lambda_{r,\mathrm{s}}\left(\frac{1}{r}\frac{\partial T_\mathrm{s}}{\partial r}+\frac{\partial^2 T_\mathrm{s}}{\partial r^2}\right)+a_s\alpha_{\mathrm{f,s}}\left(T_\mathrm{f}-T_\mathrm{s}\right)=0 \tag{2.15}$$

A detailed derivation of these equations is not discussed at this point since the derivation of energy balances is presented in Section 2.3. As shown in equations (2.14) and (2.15), convection is only considered in the fluid phase. The boundary conditions for each

Table 2.2: Boundary conditions for the heterogeneous model according to [58].

Fluid	Solid
$\frac{\partial T_\mathrm{f}}{\partial r}\vert_{r=0} = 0$	$\frac{\partial T_\mathrm{s}}{\partial r}\vert_{r=0} = 0$
$\Lambda_{r,\mathrm{f}}\frac{\partial T_\mathrm{f}}{\partial r}\vert_{r=r_i} = \alpha_{\mathrm{w,f}}(T_\mathrm{w} - T_\mathrm{f})$	$\Lambda_{r,\mathrm{s}}\frac{\partial T_\mathrm{s}}{\partial r}\vert_{r=r_i} = \alpha_{\mathrm{w,s}}(T_\mathrm{w} - T_\mathrm{s})$

phase can be taken from Table 2.2.

The heterogeneous model offers the possibility of modeling more complex physical processes in the solid phase [58], since the solid phase is modeled individually. Nevertheless, the heterogeneous model has some disadvantages over the homogeneous model. On one hand, the numerical complexity of the heterogeneous model is higher than the numerical complexity of the homogeneous model, which generally do not impose a significant disadvantage [58]. On the other hand, it is difficult to obtain the model parameters from individual experiments or rather, to individually measure the temperature of the solid and the gas phase [58].

2.2.2 Homogeneous model

Compared to the heterogeneous model, the homogeneous model does not differentiate between the solid and gas phases. As demonstrated in Figure 2.9, the homogeneous model can be divided into two sub-models [61]:

- Λ_r-model
- α_w-model

2.2.2.1 Λ_r-model

In the Λ_r-model the porosity of the bed is not considered constant across the bed; instead a porosity distribution is considered. This porosity distribution leads to radial distributed parameters. Therefore, the velocity or the effective heat conduction coefficient of the bed are functions of the radius. The energy balance can be written as follows [66]

$$\begin{aligned}(\epsilon(r)c_{\mathrm{p,g}}\rho_\mathrm{g} + (1-\epsilon(r))c_{\mathrm{p,p}}\rho_\mathrm{p})\,\frac{\partial T}{\partial t} + u_0(r)\rho_g c_{\mathrm{p,g}}\frac{\partial T}{\partial z} =& \frac{1}{r}\frac{\partial}{\partial r}\left[\Lambda_r(r) r \frac{\partial T}{\partial r}\right] \\ &+ \Lambda_{\mathrm{Ax}}(r)\frac{\partial^2 T}{\partial z^2} + \dot{w}(r)\end{aligned} \tag{2.16}$$

The radial boundary conditions are tabulated in Table 2.3.

Table 2.3: Boundary conditions for the diabatic Λ_r-model according to [64].

$r = 0$	$r = r_i$
$\frac{\partial T}{\partial r} = 0$	$T = T_\mathrm{w}$

Different models have been postulated for the porosity distribution. Giese [67] for example, proposed the following correlation for describing the porosity distribution of the bed:

$$\epsilon(r) = \epsilon_\infty \left(1 + 1.36 \exp\left(-5\frac{R-r}{d_\mathrm{p}}\right)\right) \tag{2.17}$$

Eigenberger and Bey [68] proposed a porosity distribution that is divided into two regions, including a core region and a region adjacent to the wall:

$$\epsilon_\mathrm{wall} = 0.24 + (1 - 0.24) \cdot r_*^2 \quad \text{for } r_* < 0 \tag{2.18}$$

$$\epsilon_\mathrm{core} = \epsilon_\infty + (0.24 - \epsilon_\infty) \exp\left(-\frac{r_*}{10}\right) \cos\left(\frac{\pi}{0.876} r_*\right) \quad \text{for } r_* \geq 0 \tag{2.19}$$

For r_*, they proposed the following correlation [68]:

$$r_* = \left(\frac{d}{2} - r\right) / x_\mathrm{min} - 1 \tag{2.20}$$

$$x_\mathrm{min} = 0.5 \left(d - \sqrt{(d - d_\mathrm{p})^2 - d_\mathrm{p}^2}\right) \tag{2.21}$$

An exemplary distribution using both correlations is plotted in Figure 2.10. Figure 2.10

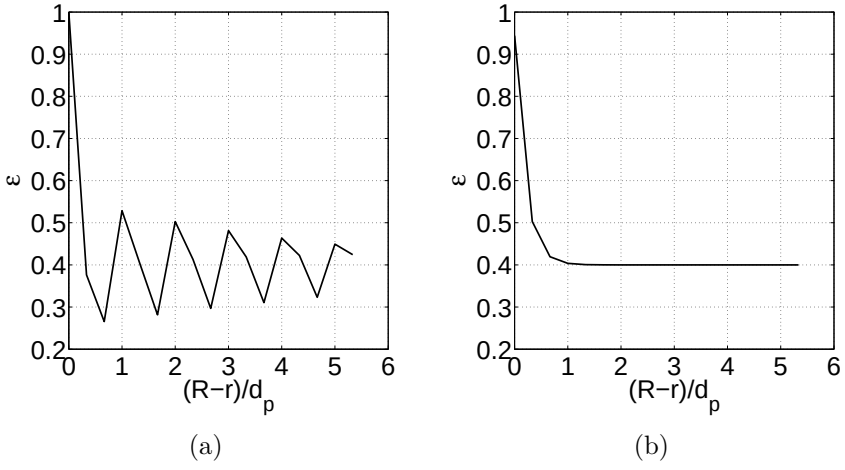

Figure 2.10: Exemplary porosity distributions using the correlations of (a) Eigenberger and Bey [68] and (b) Giese [67] with ϵ_∞=0.4, R=16 mm and d_p=3 mm.

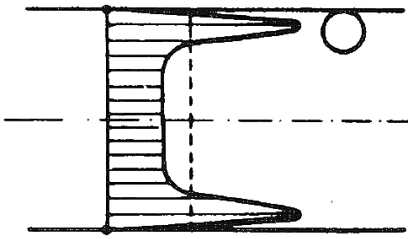

Figure 2.11: Schematic velocity distribution across the bed taken from [64].

shows that for both correlations, the porosity tends to one in the vicinity of the wall. This is also expected since it is considered that the bed consists of spheres; therefore, it is assumed that the porosity at the wall is equal to one. An overview of different porosity distribution correlations can be taken from [64]. As mentioned before, the fact that the porosity is not assumed constant and a distribution is considered leads to a radial distribution of the velocity. Since the porosity tends to one in the vicinity of the wall, the flow resistance is reduced, which leads to an increase in the velocity [64, 69]. This increase in velocity is often referred to as bypass [64]. Figure 2.11 illustrates a schematic representation of the velocity distribution along the radius of the bed.

The fact that a velocity distribution is taken into account in the Λ_r-model is considered to be one of the advantages of this model, especially for exothermic processes in diabatic packed beds [66]. Several authors have used radial dependent parameters (e.g. effective heat conduction, porosity, etc.) to model gas flow and heat transfer in packed beds with a high accuracy [66, 70–74]. Nevertheless, the question arises of whether the increase in accuracy of these models over the α_w-model is significant, such that the increase in numerical and experimental effort is justified, since an accurate porosity distribution must be measured. Winterberg et al. [66] concluded that the α_w-model also provides accurate solutions in the absence of chemical reactions. Therefore, since the heat released during physical adsorption is not as high as the heat released during an exothermic chemical reaction, and since the d-to-d_p ratio will be generally above the critical one (>10 [75]) the α_w-model seems to be the better choice in this case.

2.2.2.2 α_w-model

The energy balance for the α_w-model can be written as follows [61, 73]:

$$(\epsilon c_{\mathrm{p,g}}\rho_\mathrm{g} + (1-\epsilon)c_{\mathrm{p,p}}\rho_\mathrm{p})\frac{\partial T}{\partial t} + u_0\rho_g c_{\mathrm{p,g}}\frac{\partial T}{\partial z} = \frac{\Lambda_r}{r}\frac{\partial}{\partial r}\left[r\frac{\partial T}{\partial r}\right] + \Lambda_\mathrm{Ax}\frac{\partial^2 T}{\partial z^2} + \dot{w} \tag{2.22}$$

The boundary conditions for this model are tabulated in Table 2.4. Equation 2.22 shows that the model is based on the assumption of radial independent model parameters (e.g. porosity, velocity and the effective model parameters). This model also assumes a boundary condition of the third kind [61] between the homogeneous phase and the

Table 2.4: Boundary conditions for the diabatic α_w-model [58, 61].

$r = 0$	$r = r_i$
$\frac{\partial T}{\partial r} = 0$	$\alpha_w(T_w - T) = \Lambda_r \frac{\partial T}{\partial r}$

wall, as shown in Table 2.4. This heat transfer coefficient was introduced in order to consider the steep temperature increase at the vicinity of the wall [58]. The use of this boundary condition is also the reason why this model is called the α_w-model.

Contrary to the Λ_r-model the α_w-model only requires a constant porosity. Therefore, it is necessary to determine the mean bed porosity of the packed bed. The mean bed porosity can be obtained by integrating the porosity distribution (e.g equation 2.17) over the radius. Similar results to those obtained through the integration can be derived using the empirical correlation of Sonntag [61, 76]:

$$\epsilon = \epsilon_\infty + (1 - \epsilon_\infty)\frac{0.526}{d/d_p} \tag{2.23}$$

Since the mean bed porosity can be calculated using equation 2.23 only the dispersion coefficients and the wall heat transfer coefficient remain as unknown model parameters. As mentioned earlier, the axial dispersion can often be neglected in diabatic packed beds, which reduces the number of unknown relevant parameters of the model to the radial dispersion Λ_r and the wall heat transfer coefficient α_w.

For the wall heat transfer coefficient, several Nusselt correlations have been postulated over the years, which can be categorized into the following two groups:

$$\mathrm{Nu}_w = a_1 \cdot \mathrm{Re}^{a_2} \cdot \mathrm{Pr}^{a_3} \tag{2.24}$$

$$\mathrm{Nu}_w = \mathrm{Nu}_{w,0} + b_1 \cdot \mathrm{Re}^{b_2} \cdot \mathrm{Pr}^{b_3} \tag{2.25}$$

An overview of some of the derived Nusselt correlations can be found in [63, 64]. It is shown in equation 2.24 that, in the case of no convection ($\mathrm{Re} \to 0$), the Nusselt number will tend to zero. This would mean that the system behaves as a perfect insulator, which is not the case. Therefore, Tsotsas [64] criticized this model, arguing that the physical meaning of the wall heat transfer coefficient vanishes when the Reynolds number goes to zero. Nevertheless, several authors [58, 65, 70, 77, 78] postulated Nusselt correlations based on equation 2.25, which do not have the limitation mentioned by Tsotsas. Nilles [58, 65] for example, investigated the heat transfer in packed beds at low Reynolds numbers and postulated the following correlation [58, 61, 65]:

$$\mathrm{Nu}_w = \left(1.3 + \frac{5}{d/d_p}\right)\frac{\lambda_{bed}}{\lambda_g} + 0.19 \cdot \mathrm{Re}^{0.75} \cdot \mathrm{Pr}^{0.33} \tag{2.26}$$

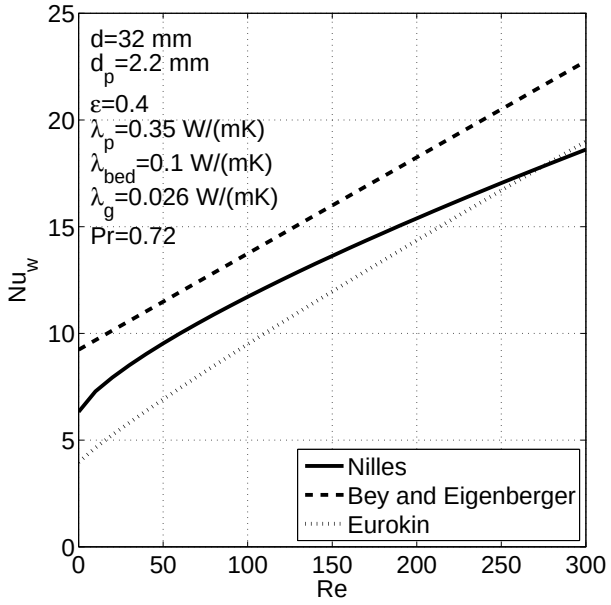

Figure 2.12: Exemplary representation of the correlations of Nilles [58, 65], Bey and Eigenberger [70] and Eurokin [77]. The parameter values that were used are listed in the upper left corner of the figure.

which is based on equation 2.25. He was able to correlate his experimental measurements satisfactorily. Therefore, the Nusselt correlations based on equation 2.25 are the ones more adequate to model the heat transfer between the wall and the homogeneous phase. An exemplary representation of different correlations is shown in Figure 2.12.

Correlations for calculating the radial dispersion will be presented in Section 2.2.4 after having introduced the correlations for the effective heat conduction of the bed λ_{bed}.

Several authors have used models based on the α_{w}-model to simulate heat transfer in packed beds [58, 63, 65, 70, 79–84] and have obtained good results. The use of this model is therefore justified, as long as the d-to-d_{p}-ratio is adequate to avoid bypass flows and no extreme exothermic reactions/processes are considered [61]. Since the d-to-d_{p}-ratio will often be higher than the critical one in this work and since the heat released during physical adsorption is lower than the heat released during an exothermic reaction the α_{w}-model was chosen as the adequate model for this work. Another advantage of the α_{w}-model is the reduction in numerical complexity [61].

2.2.3 Heat conduction in packed beds without convection

The effective heat conduction of a packed bed without convection depends on several parameters, which can be categorized in primary influence parameters and secondary influence parameters [61]. According to Tsotsas [64], the primary influence parameters are the heat conduction of the solid phase (λ_{p}), the heat conduction of the fluid phase

(λ_g), and the bed porosity (ϵ). Therefore, a functional dependency of the following type is expected for the effective heat conduction of the bed [64]:

$$\lambda_{bed} = f(\lambda_p, \lambda_g, \epsilon) \tag{2.27}$$

if the primary influence parameters are taken into account. Besides the primary influence parameters several other parameters can be considered as influence parameters, e.g. heat radiation, heat conduction through the contact area, and pressure dependency of the heat conduction of gases [69]. Also, the particle form and the particle size distribution can have an impact on the effective heat conduction of the bed [61]. These influence parameters are categorized as secondary influence parameters [61]. Secondary influence parameters can often be neglected and the effective heat conduction of the bed can be determined considering only the primary influence parameters. For example, poly-dispersed beds can be treated as mono-dispersed beds, as long as the correct porosity of the bed is considered [61]. Heat radiation for example, should only be considered if high temperatures (>200 °C) are expected during the process. The pressure dependency of the heat conduction can be neglected as long as the free mean path of the gas molecules is smaller than the particle diameter [64]. The ratio of both mentioned lengths is called the Knudsen number [64]. Thus, the effective heat conduction of the bed will only depend on the pressure if the Knudsen number is high [64]. This effect is also known as the Smoluchowski effect [64].

In order to model the heat transfer in a packed bed without convection, a mathematical model that follows the functional dependency of equation 2.27 is required. The postulated model should also fulfill the following conditions [61, 64]:

1.) $\epsilon = 0 \Rightarrow \lambda_{bed} = \lambda_p$

2.) $\epsilon = 1 \Rightarrow \lambda_{bed} = \lambda_g$

3.) $\lambda_g = \lambda_p \Rightarrow \lambda_{bed} = \lambda_g = \lambda_p$

4.) $\lambda_g \to \infty \Rightarrow \lambda_{bed} \to \infty$

5.) $\lambda_p \to \infty \Rightarrow \lambda_{bed} \to \infty$

6.) $\lambda_g = 0 \Rightarrow \lambda_{bed} = 0$

7.) $\lambda_p = 0 \Rightarrow \dfrac{\lambda_{bed}}{\lambda_g} = \dfrac{D_{bed}}{D_{i,N}}$

The first four conditions are logical, and the fifth condition is only true if there is a point contact or a surface contact between the particles [61]. Condition six can only be valid if there is no contact or if there is a point contact between the particles [61]. The last condition states, that the related effective heat conduction of a bed with particles that do not conduct heat is equal to the coefficient between the effective diffusion coefficient of the bed and the diffusion coefficient in the fluid phase [61].

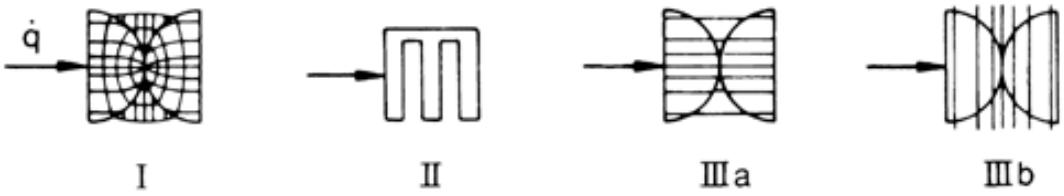

Figure 2.13: Schematic representation of the different categories for estimating the effective heat conduction of packed beds taken from [61].

Several models for describing the effective heat conduction of the packed bed have been postulated which can be divided in three categories [61, 64]:

- Type I: Exact estimation of the temperature field (analytical or numerical)
- Type II: Coupling of resistances
- Type III(a,b): Unit cell with parallel heat streamlines(a) or with parallel isotherms(b)

a schematic representation of the different categories can be observed in Figure 2.13.

A known model of Type I was derived analytically by Maxwell [61], and it assumes that the particles do not influence each other [61].

$$\frac{\lambda_{\mathrm{bed}}}{\lambda_{\mathrm{g}}} = \frac{1 + 2 \cdot \phi_{\mathrm{Maxwell}}}{1 - \phi_{\mathrm{Maxwell}}} \tag{2.28}$$

$$\phi_{\mathrm{Maxwell}} = (1 - \epsilon) \frac{\frac{\lambda_{\mathrm{p}}}{\lambda_{\mathrm{g}}} - 1}{\frac{\lambda_{\mathrm{p}}}{\lambda_{\mathrm{g}}} + 2} \tag{2.29}$$

The use of this model is therefore suitable if diluted suspension or emulsions are considered [61]. If a packed bed is considered, one can obtain reliable results only for low ratios of the heat conduction of the solid and fluid phase ($\lambda_{\mathrm{p}}/\lambda_{\mathrm{g}} < 20$) [61]. Equation 2.28 also shows that this model does not fulfill condition five [64]. This is also a limitation of this model regarding its universal applicability.

The models of Type II can be subdivided into models with resistances in series and models with resistances in parallel. Given a fixed set of coefficient parameters, the highest effective heat conduction will be obtained using the resistance in series model and the lowest by using the resistance in parallel model [61]. There is a broad range between the two limits and packed beds will lay in between these limits. Therefore, Kirscher [61, 85] proposed a model in which a parameter a will weigh the contribution of the series connection and the parallel connection.

$$\frac{\lambda_{\mathrm{bed}}}{\lambda_{\mathrm{g}}} = \left(\frac{a}{\left(\epsilon + \frac{1-\epsilon}{\frac{\lambda_{\mathrm{p}}}{\lambda_{\mathrm{g}}}} \right)^{-1}} + \frac{1-a}{\epsilon + (1-\epsilon)\frac{\lambda_{\mathrm{p}}}{\lambda_{\mathrm{g}}}} \right)^{-1} \tag{2.30}$$

In other words, parameter a is a structure parameter. For packed beds, a value of 0.2 can be used for the parameter a [61]. The model of Kirscher allows an easy and fast estimation of the effective heat conduction of the packed bed. Nevertheless, it is not adequate for an accurate estimation [61]. In addition, the model of Kirscher does not fulfill conditions four and five [61] and it provides an unreasonable result for condition seven [64]

$$\lambda_{\mathrm{p}} = 0 \Rightarrow \frac{\lambda_{\mathrm{bed}}}{\lambda_{\mathrm{g}}} = \frac{D_{\mathrm{bed}}}{D_{\mathrm{i,N}}} = 0$$

One of the most known models of Type III is the Zehner/Bauer/Schlünder-model (ZBS-model). The aim of this model is to correct the non-applicable assumption of parallel heat streamlines by simulating spheres with non-spheres [61]. The exact contour of these model particles is estimated using the parameter B_{ZBS}. The unit cell that was used to derive the ZBS-model is shown in Figure 2.14. The unit cell consists of a cylindrical core with two particle halves on opposite sides of the core and a cylindrical shell filled with fluid that surrounds the core [61]. The idea is that only part of the heat streamlines will pass through the fluid phase, and will have an area share of $1 - \sqrt{1-\epsilon}$ [86]. The other part of the heat streamlines will pass through the solid and fluid phase, and will have an area share of $\sqrt{1-\epsilon}$ [86]. If the effective heat conduction of the cylindrical core with the area share $\sqrt{1-\epsilon}$ is defined as λ_{c} the following correlation can be derived using the law of resistances in parallel for the effective heat conduction of the unit cell [86]:

$$\frac{\lambda_{\mathrm{bed}}}{\lambda_{\mathrm{g}}} = 1 - \sqrt{1-\epsilon} + \sqrt{1-\epsilon}\frac{\lambda_{\mathrm{c}}}{\lambda_{\mathrm{g}}} \tag{2.31}$$

The effective heat conduction of the core is determined considering the law of resistances in series which leads to the following integral [86]:

$$\frac{\lambda_{\mathrm{c}}}{\lambda_{\mathrm{g}}} = 2\int_{z=0}^{1} \frac{z \cdot dz}{\left(\lambda_{\mathrm{g}}/\lambda_{\mathrm{p}} - 1\right)\left(B_{\mathrm{ZBS}} - (B_{\mathrm{ZBS}} - 1)z\right)^3} \tag{2.32}$$

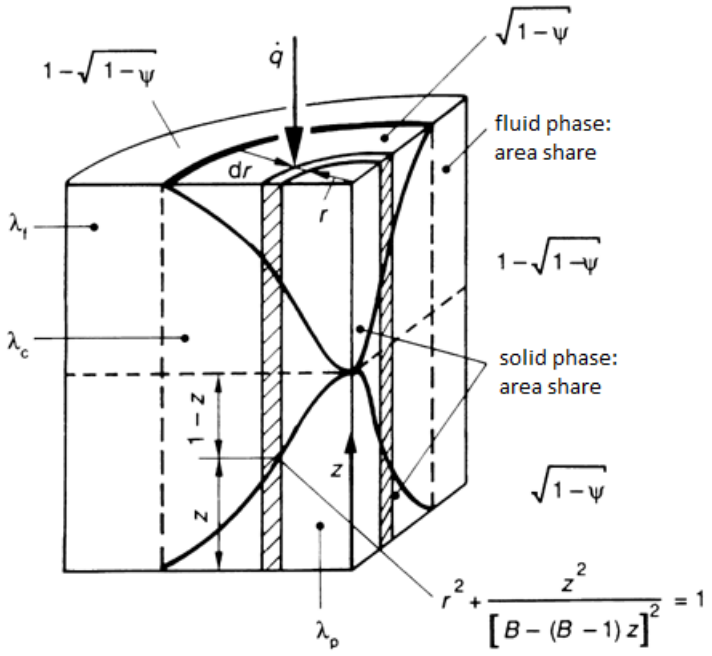

Figure 2.14: Unit cell used for deriving the ZBS-model taken from [61].

Solving the integral leads to the following correlation [61, 64, 86]:

$$\frac{\lambda_c}{\lambda_g} = \frac{2}{N}\left(\frac{B_{ZBS}}{N^2}\frac{\lambda_p/\lambda_g - 1}{\lambda_p/\lambda_g}\ln\frac{\lambda_p/\lambda_g}{B_{ZBS}} - \frac{B_{ZBS}+1}{2} - \frac{B_{ZBS}-1}{N}\right) \tag{2.33}$$

with

$$N = 1 - \frac{B_{ZBS}}{\lambda_p/\lambda_g} \tag{2.34}$$

The parameter B_{ZBS} can be calculated using the following correlation:

$$\epsilon = 1 - \left(\frac{B_{ZBS}}{(B_{ZBS}-1)^3}\left(3 - 4B_{ZBS} + B_{ZBS}^2 + 2\ln B_{ZBS}\right)\right)^2 \tag{2.35}$$

which can only be solved iteratively [86]. Therefore an approximate solution is usually used which gives almost the same results [61, 64, 86]:

$$B_{ZBS} = 1.25\left(\frac{1-\epsilon}{\epsilon}\right)^{10/9} \tag{2.36}$$

The ZBS-model also fulfills conditions one to six [61] and leads to the following expression for condition seven [61]

$$\lambda_p = 0 \Rightarrow \frac{\lambda_{bed}}{\lambda_g} = \frac{D_{bed}}{D_{i,N}} = 1 - \sqrt{1-\epsilon} \tag{2.37}$$

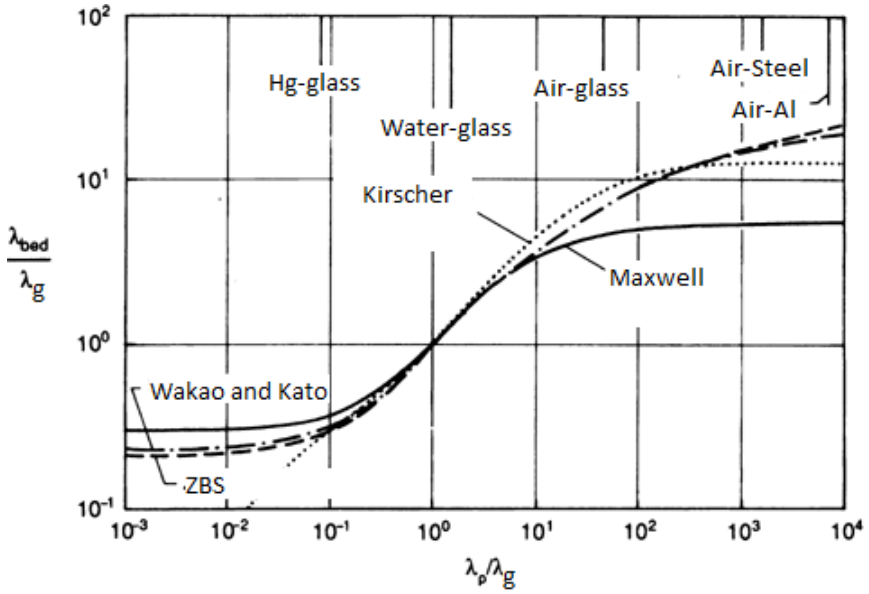

Figure 2.15: Comparison of the different models with the numerical results obtained by Wakao and Kato [87] taken from [61].For the models, a porosity of $\epsilon = 0.4$ was used, whereas in the numerical study a porosity of $\epsilon = 0.395$ was considered.

In Figure 2.15 a comparison of the different models with the numerical results obtained by Wakao and Kato [87] can be observed. Figure 2.15 demonstrates that the ZBS-model shows an excellent agreement with the numerical results that were obtained by Wakao and Kato [87]. Therefore, the ZBS-model is the most adequate model for calculating the effective heat conduction of the packed bed in this work.

2.2.4 Heat conduction in packed beds with convection

If convection is considered, the heat transfer inside the bed is increased because the fluid is mixed inside of the bed, which increases the rate of heat transfer. In the α_w-model, where thermal equilibrium and a plug-flow is assumed, this increase in heat transfer rate is considered by an increase in the effective heat conduction coefficients of the packed bed. The effective heat conduction coefficients of the packed bed can be calculated using the following correlations [61]:

$$\frac{\lambda_{\mathrm{eff,Ax}}}{\lambda_g} = \frac{\lambda_{\mathrm{bed}}}{\lambda_g} + \frac{\mathrm{Pe}}{2} \tag{2.38}$$

$$\frac{\lambda_{\mathrm{eff,Rad}}}{\lambda_g} = \frac{\lambda_{\mathrm{bed}}}{\lambda_g} + \frac{\mathrm{Pe}}{K_{\mathrm{Rad}}} \tag{2.39}$$

with [61]

$$K_{\mathrm{Rad}} = 7\left(2 - \left(1 - \frac{2}{d/d_p}\right)^2\right) \tag{2.40}$$

If the equivalence theory of Vortmeyer [62, 88]:

$$\frac{\partial^2 T_\mathrm{s}}{\partial z^2} = \frac{\partial^2 T_\mathrm{g}}{\partial z^2}$$

is applied to a heterogeneous-model in order to reduce it to a homogeneous model, similar structures to equations (2.38) and (2.39) can be obtained

$$\lambda_\mathrm{eff} = \lambda_\mathrm{bed} + \frac{\dot{m}_\mathrm{g}^2 \cdot c_\mathrm{p,g}^2}{\alpha \cdot S} \tag{2.41}$$

where α is the heat transfer coefficient from the solid to the fluid phase and S is the heat transfer area per volume.

2.3 Modeling an indirect heated adsorption process

2.3.1 Mathematical model

The model is based on the assumption that all of the tubes in the bundle behave equally. This simplifies the simulation as it allows for the simulation of only one tube of the bundle which reduces computational time significantly. For the tube a 2D axial-symmetrical model was chosen that is coupled with a 1D model for the heat transfer fluid. Figure 2.16 illustrates the model that is used in this work. Three different phases are taken into account:

1.) adsorbent bed and interstitial gas phase

2.) tube wall

3.) heat transfer fluid

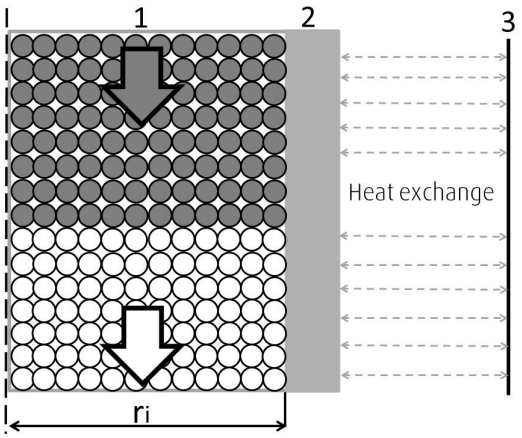

Figure 2.16: Representation of the model. The model is subdivided into three different phases. The first phase (1) is the adsorbent bed and the interstitial gas phase. The second phase (2) represents the tube wall. The heat transfer fluid is represented by the last phase (3).

2.3.1.1 Adsorbent bed and interstitial gas phase

In order to derive the partial differential equations (PDEs) that describe the first phase (adsorbent bed and interstitial gas), the following assumptions are made:

- 2D axial symmetrical model
- solid and gas phase are in thermal equilibrium
- a continuum with effective physical parameters is considered (α_{w}-model)
- gas phase is considered as ideal gas
- angular dependency of the conservation laws is neglected

Energy balance

As shown in Figure 2.17, conduction ($\dot{Q}_\lambda$) and convection ($\dot{H}$) are considered and a heat source/sink ($\dot{W}$) due to adsorption. Therefore, the energy balance is written as:

$$\begin{aligned}\frac{\partial \Delta U}{\partial t} =& \dot{Q}_{\lambda,r} - \dot{Q}_{\lambda,r+\mathrm{dr}} + \dot{Q}_{\lambda,z} - \dot{Q}_{\lambda,z+\mathrm{dz}} \\ &+ \dot{H}_r - \dot{H}_{r+\mathrm{dr}} + \dot{H}_z - \dot{H}_{z+\mathrm{dz}} + \dot{W}\end{aligned} \tag{2.42}$$

since it is a conservation law. Considering the thermal equilibrium between the solid and gas phase, the accumulation term (ΔU) is written as follows:

$$\Delta U = \left(\epsilon c_{\mathrm{p,g}} \rho_{\mathrm{g}} + (1-\epsilon) c_{\mathrm{p,p}} \rho_{\mathrm{p}}\right) T \Delta V \tag{2.43}$$

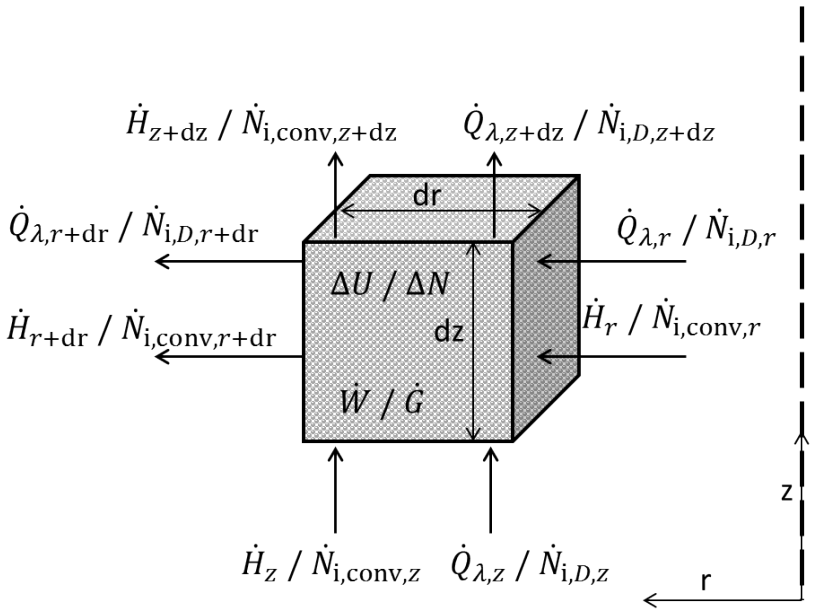

Figure 2.17: Differential control volume with conductive ($\dot{Q}_\lambda$) / diffusive ($\dot{N}_D$) flows, convective flows ($\dot{H}/\dot{N}_{\mathrm{conv}}$), accumulation ($\Delta U/\Delta N$) and a heat ($\dot{W}$) / mass ($\dot{G}$) source/sink.

where each phase is weighted by its volumetric share. The conduction term is modeled using Fourier's law [89]:

$$\dot{Q}_{\lambda,k} = \dot{q}_{\lambda,k}\Delta A_k = -\lambda_{\mathrm{eff},k}\frac{\partial T}{\partial k}\Delta A_k \tag{2.44}$$

It must be kept in mind that the conduction term has to be related to the entire control area since effective physical parameters are used [64]. Similar to the heat conduction term, the convective term must be related to the entire area and not to the volumetric weighted area of the gas phase:

$$\dot{H}_k = u_k \rho_g c_{\mathrm{p,g}} T \Delta A_k \tag{2.45}$$

The contribution of the gas phase to the effective density of the continuous phase is minimal and can therefore be neglected. This leads to the following expression for the heat source/sink $\dot{W}$:

$$\dot{W} = (1-\epsilon)\,\rho_{\mathrm{p}} \sum_{\mathrm{i}} \Delta H_{\mathrm{ads,i}} \frac{\partial q_{\mathrm{i}}}{\partial t}\Delta V \tag{2.46}$$

The terms $\dot{Q}_{\lambda,k+\mathrm{dk}}$ and $\dot{H}_{k+\mathrm{dk}}$ can be expressed as:

$$\dot{Q}_{\lambda,k+\mathrm{dk}} = \dot{Q}_{\lambda,k} + \frac{\partial \dot{Q}_{\lambda,k}}{\partial k}\Delta k \tag{2.47}$$

$$\dot{H}_{k+\mathrm{dk}} = \dot{H}_k + \frac{\partial \dot{H}_k}{\partial k}\Delta k \tag{2.48}$$

by using the Taylor series [90] and only considering the first two terms, since $\Delta k^2 \ll 0$. Inserting equation (2.43) until (2.48) into equation (2.42) leads to the PDE describing the energy balance for the adsorbent bed and interstitial gas phase:

$$\begin{aligned}(\epsilon c_{\mathrm{p,g}}\rho_{\mathrm{g}} + (1-\epsilon)c_{\mathrm{p,p}}\rho_{\mathrm{p}})\,\frac{\partial T}{\partial t} + \rho_g c_{\mathrm{p,g}}\,(\boldsymbol{u}\circ\nabla T) =& \nabla\circ(\boldsymbol{\lambda}_{\mathbf{eff}}\circ\nabla T) \\ &+ (1-\epsilon)\,\rho_{\mathrm{p}}\cdot\sum_{\mathrm{i}}\Delta H_{\mathrm{ads,i}}\frac{\partial q_{\mathrm{i}}}{\partial t}\end{aligned} \tag{2.49}$$

The effective heat conduction coefficients can be taken from equations (2.38) and (2.39).

Component mass balance

Similar to the energy balance the mass balance is also a conservation law which leads to the following postulate (Figure 2.17):

$$\begin{aligned}\frac{\partial \Delta N_{\mathrm{i}}}{\partial t} =& \dot{N}_{\mathrm{i},D,r} - \dot{N}_{\mathrm{i},D,r+\mathrm{dr}} + \dot{N}_{\mathrm{i},D,z} - \dot{N}_{\mathrm{i},D,z+\mathrm{dz}} \\ &+ \dot{N}_{\mathrm{i,conv},r} - \dot{N}_{\mathrm{i,conv},r+\mathrm{dr}} + \dot{N}_{\mathrm{i,conv},z} - \dot{N}_{\mathrm{i,conv},z+\mathrm{dz}} + \dot{G}_{\mathrm{i}}\end{aligned} \tag{2.50}$$

$\dot{N}_{\mathrm{i},D,k}$ represent the diffusive flows and $\dot{N}_{\mathrm{i,conv},k}$ the convective ones. Since adsorption/desorption is considered a mass source/sink ($\dot{G}_{\mathrm{i}}$) must be taken into account. The change in mass (ΔN_{i}) of component i is modeled as follows:

$$\Delta N_{\mathrm{i}} = \epsilon c_{\mathrm{i}} \Delta V \tag{2.51}$$

The diffusive flows are postulated using Fick's law [52, 91]:

$$\dot{N}_{\mathrm{i},D,k} = -D_{\mathrm{eff},k} \frac{\partial c_{\mathrm{i}}}{\partial k} \Delta A_k \tag{2.52}$$

with $D_{\mathrm{eff},k}$ as the dispersive coefficient and the convective flows as:

$$\dot{N}_{\mathrm{i,conv},k} = u_k c_{\mathrm{i}} \Delta A_k \tag{2.53}$$

Similar to the energy balance these terms must be related to the entire area and not only to the volumetric weighted area of the gas phase. The model parameters are, therefore, effective parameters. The mass source/sink is modeled using the following equation:

$$\dot{G}_{\mathrm{i}} = -\left(1-\epsilon\right) \rho_{\mathrm{p}} \frac{\partial q_{\mathrm{i}}}{\partial t} \cdot \Delta V \tag{2.54}$$

Like for the energy balance, the terms $\dot{N}_{\mathrm{i},D,k+\mathrm{dk}}$ and $\dot{N}_{\mathrm{i,conv},k+\mathrm{dk}}$ are approximated using the Taylor series [90] and only considering the first two terms:

$$\dot{N}_{\mathrm{i},D,k+\mathrm{dk}} = \dot{N}_{\mathrm{i},D,k} + \frac{\partial \dot{N}_{\mathrm{i},D,k}}{\partial k} \Delta k \tag{2.55}$$

$$\dot{N}_{\mathrm{i,conv},k+\mathrm{dk}} = \dot{N}_{\mathrm{i,conv},k} + \frac{\partial \dot{N}_{\mathrm{i,conv},k}}{\partial k} \Delta k \tag{2.56}$$

Inserting equations (2.51) to (2.56) into equation (2.50) leads to the PDE describing the mass balance of component i:

$$\epsilon \frac{\partial c_{\mathrm{i}}}{\partial t} + \nabla \left(\boldsymbol{u} \circ c_{\mathrm{i}}\right) = \nabla \circ \left(\boldsymbol{D}_{\mathbf{eff}} \circ \nabla c_{\mathrm{i}}\right) - \left(1-\epsilon\right) \rho_{\mathrm{p}} \cdot \frac{\partial q_{\mathrm{i}}}{\partial t} \tag{2.57}$$

The dispersion coefficient is calculated using the following correlation [61]:

$$\frac{D_{\mathrm{eff},k}}{D_{\mathrm{i,N}}} = \frac{D_{\mathrm{bed}}}{D_{\mathrm{i,N}}} + \frac{\mathrm{Pe}_{0,\mathrm{m}}}{K_k} \tag{2.58}$$

which is derived using the analogy between heat and mass transfer and with D_{bed} as [61]:

$$\frac{D_{\mathrm{bed}}}{D_{\mathrm{i,N}}} = 1 - \sqrt{1-\epsilon} \tag{2.59}$$

This correlation for the effective bed diffusion coefficient D_{bed} is similar to the correlation that is used to describe the effective heat conduction, which is again a consequence of the analogy between heat and mass transfer.

Global mass balance

Since temperature and pressure change in the adsorbent bed, the gas density and therefore the gas velocity is influenced along the adsorbent bed [92]. In order to consider the change in velocity, a PDE is necessary. The global mass balance is used in order to find the velocity distribution in the bed [92]. Adding the component mass balances over the number of components j leads to the following PDE:

$$\sum_{\mathrm{j}} \epsilon \frac{\partial c_{\mathrm{i}}}{\partial t} + \sum_{\mathrm{j}} \nabla \left(\boldsymbol{u} \circ c_{\mathrm{i}} \right) = \sum_{\mathrm{j}} \nabla \circ \left(\boldsymbol{D}_{\mathbf{eff}} \circ \nabla c_{\mathrm{i}} \right) + \sum_{\mathrm{j}} \left(1 - \epsilon \right) \rho_{\mathrm{p}} \cdot \frac{\partial q_{\mathrm{i}}}{\partial t} \tag{2.60}$$

The sum of the diffusive/dispersive flows must be equal to zero [93], which simplifies the PDE to:

$$\sum_{\mathrm{j}} \epsilon \frac{\partial c_{\mathrm{i}}}{\partial t} + \sum_{\mathrm{j}} \nabla \left(\boldsymbol{u} \circ c_{\mathrm{i}} \right) = - \sum_{\mathrm{j}} \left(1 - \epsilon \right) \rho_{\mathrm{p}} \cdot \frac{\partial q_{\mathrm{i}}}{\partial t} \tag{2.61}$$

Using Dalton's law, which implies that the pressure of a system of ideal gases is equal to the sum of the partial pressure of the gases [94]:

$$p = \sum_{\mathrm{j}} p_{\mathrm{i}} \tag{2.62}$$

using the ideal gas equation:

$$\begin{aligned} & p \cdot V = N \cdot \mathbb{R} \cdot T \\ & \Rightarrow p = c \cdot \mathbb{R} \cdot T \end{aligned} \tag{2.63}$$

shows that the concentration of the system is equal to the sum of the concentration of the components:

$$c = \sum_{\mathrm{j}} c_{\mathrm{i}} \tag{2.64}$$

Inserting equation (2.64) into equation (2.61) leads to the PDE describing the global mass balance:

$$\epsilon \frac{\partial c}{\partial t} + \nabla \left(\boldsymbol{u} \circ c \right) = - \sum_{\mathrm{j}} \left(1 - \epsilon \right) \rho_{\mathrm{p}} \cdot \frac{\partial q_{\mathrm{i}}}{\partial t} \tag{2.65}$$

Momentum balance

The momentum balance can be derived in a similar manner to the mass and energy balance, since it is also a conservation law. A balance over a control volume leads to the following PDE [93]:

$$\frac{\partial}{\partial t}\rho_g \boldsymbol{u} = -\left[\nabla \circ \boldsymbol{\phi}\right] + \rho_g \boldsymbol{g} \tag{2.66}$$

where $\boldsymbol{\phi}$ represents the combined momentum flux between molecular and convective momentum and $\rho_g \boldsymbol{g}$ is the gravitational force. The combined momentum flux is written as [93]:

$$\boldsymbol{\phi} = p\boldsymbol{I} + \boldsymbol{\tau} + \rho_g \boldsymbol{u}\boldsymbol{u} \tag{2.67}$$

where $\boldsymbol{I}$ is the unit vector pointing in the x,y,z directions and $\boldsymbol{\tau}$ is the stress tensor. Inserting equation (2.67) into equation (2.66) leads to the following PDE [93]:

$$\frac{\partial}{\partial t}\rho_g \boldsymbol{u} = -\left[\nabla \circ \rho \boldsymbol{u}\boldsymbol{u}\right] - \nabla p - \left[\nabla \circ \boldsymbol{\tau}\right] + \rho_g \boldsymbol{g} \tag{2.68}$$

where the velocity is the independent variable. Nevertheless, the velocity is determined using the global mass balance. Therefore, a correlation between the velocity and the change of pressure can be derived using equation (2.68):

$$-\nabla p = \frac{\partial}{\partial t}\rho_g \boldsymbol{u} + \left[\nabla \circ \rho \boldsymbol{u}\boldsymbol{u}\right] + \left[\nabla \circ \boldsymbol{\tau}\right] - \rho_g \boldsymbol{g} \tag{2.69}$$

If the gravitational force is neglected and if it is assumed that the velocity reaches a stationary profile immediately then equation (2.69) simplifies to:

$$-\nabla p = \left[\nabla \circ \boldsymbol{\tau}\right] + \left[\nabla \circ \rho \boldsymbol{u}\boldsymbol{u}\right] \tag{2.70}$$

The pressure change or pressure drop in fixed beds has often been modeled using semi-empirical correlations with a contribution of the viscous drag at the surface of the particles and a turbulent contribution [95]:

$$-\nabla p = A_1 \boldsymbol{u} + A_2 \boldsymbol{u}^n \tag{2.71}$$

The transition from laminar to turbulent is according to Damköhler [96] at Reynolds number between 30 and 70 ($30 \leq \mathrm{Re} < 70$). If equation (2.71) is compared to equation (2.70) one can see that the structure of both equations is similar. Therefore, one can assume, that the semi-empirical equations are based on equation (2.70) and were fitted with experimental data. This leads to less numerical intensive equations for the momentum balance. The most common semi-empirical correlation for describing the pressure drop in fixed beds is the correlation according to Ergun [92, 97]:

$$-\nabla p = 150\frac{(1-\epsilon)^2}{\epsilon^3 d_\mathrm{p}^2}\eta_g \boldsymbol{u} + 1.75\frac{1-\epsilon}{\epsilon^3 d_\mathrm{p}}\rho_g \boldsymbol{u}^2 \tag{2.72}$$

with η_g being the dynamic viscosity. The correlation of Wilke is used in order to determine the viscosity of the gas mixture [98]:

$$\eta_g = \sum_\mathrm{i} \frac{y_\mathrm{i}\eta_{g\mathrm{i}}}{\sum_\mathrm{j} y_\mathrm{j}\theta_\mathrm{ij}} \tag{2.73}$$

where $\theta_\mathrm{i,j}$ is calculated using the approximation by Herning and Zipperer [98]:

$$\theta_\mathrm{i,j} = \left(\frac{M_\mathrm{j}}{M_\mathrm{i}}\right)^{1/2} \tag{2.74}$$

Kinetic model

The LDF-model is used to describe the adsorption kinetic in the indirect heated and cooled adsorption process:

$$\frac{\partial q_\mathrm{i}}{\partial t} = k_\mathrm{LDF,i}(q_\mathrm{i}^* - q_\mathrm{i}) \tag{2.75}$$

The LDF coefficient $k_\mathrm{LDF,i}$ can be calculated according to equation (2.11).

2.3.1.2 Tube wall

No mass transfer or momentum transfer needs to be considered in the tube's wall since they are assumed solid and not permeable (e.g. steel). Therefore, only the energy balance with conductive contribution needs to be considered, as illustrated in Figure 2.18. A balance over the control volume leads to the following equation:

$$\frac{\partial \Delta U_\mathrm{w}}{\partial t} = \dot{Q}_{\mathrm{w},\lambda,r} - \dot{Q}_{\mathrm{w},\lambda,r+\mathrm{dr}} + \dot{Q}_{\mathrm{w},\lambda,z} - \dot{Q}_{\mathrm{w},\lambda,z+\mathrm{dz}} \tag{2.76}$$

The following PDE can be derived from equation (2.76):

$$\rho_\mathrm{w} c_{\mathrm{p,w}} \frac{\partial T_\mathrm{w}}{\partial t} = \nabla \circ (\boldsymbol{\lambda}_\mathbf{w} \nabla T_\mathrm{w}) \tag{2.77}$$

using Fourier's law [89] to describe $\dot{Q}_{\mathrm{w},\lambda,k}$ and approximate $\dot{Q}_{\mathrm{w},\lambda,k+\mathrm{dk}}$ with the Taylor series [90] and using for the accumulation term:

$$\Delta U_\mathrm{w} = \rho_w c_{\mathrm{p,w}} T_w \Delta V \tag{2.78}$$

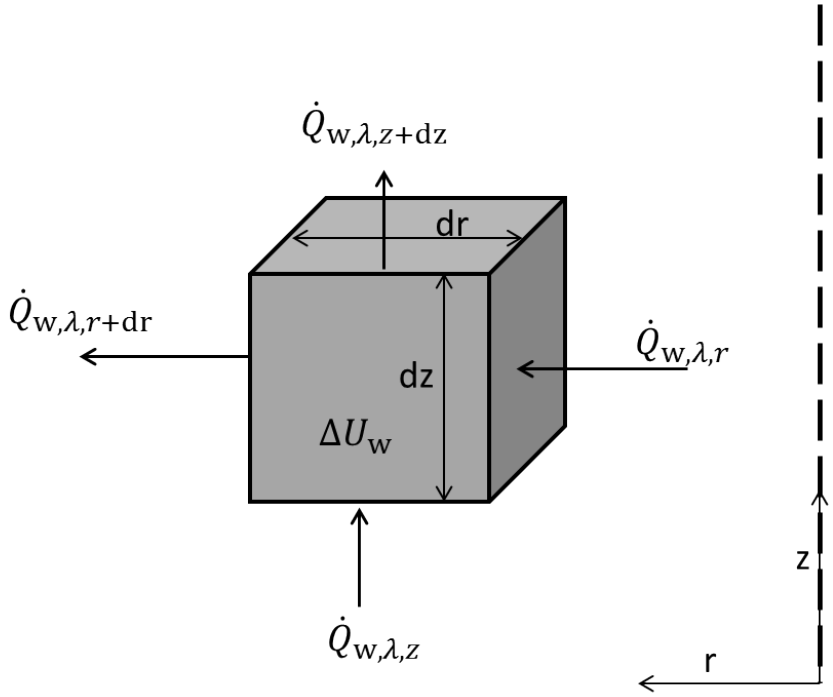

Figure 2.18: Differential control volume of the tube wall with conductive ($\dot{Q}_{w\lambda}$) flows and the accumulation term (ΔU_w).

The heat conduction coefficient of a solid can often be assumed as homogeneous and temperature independent. This simplifies equation (2.77) to:

$$\rho_w c_{p,w} \frac{\partial T_w}{\partial t} = \lambda_w \nabla \circ (\nabla T_w) \tag{2.79}$$

2.3.1.3 Heat transfer fluid

To derive the model equations that describe the heat transfer fluid, the following assumptions are made:

- 1D model
- co- or counter-current flow is assumed
- pressure drop is neglected
- triangular layout of the tubes in the bundle

Since no pressure drop is considered and no mass transfer to the solid can occur, only the heat balance is necessary to describe the heat transfer fluid phase. The following energy balance can be postulated considering Figure 2.19:

$$\frac{\partial \Delta U_{HEX}}{\partial t} = \dot{Q}_{HEX,\lambda,z} - \dot{Q}_{HEX,\lambda,z+dz} + \dot{H}_{HEX,z} - \dot{H}_{HEX,z+dz} + \dot{Q}_\alpha \tag{2.80}$$

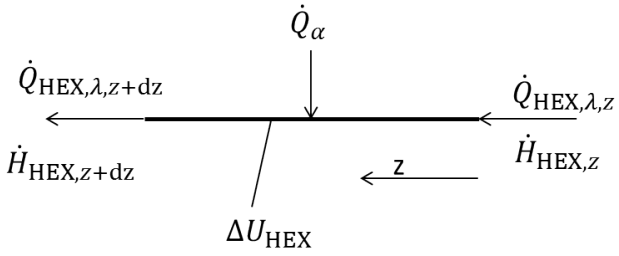

Figure 2.19: Differential control volume of the heat transfer fluid with conductive flows ($\dot{Q}_{\mathrm{HEX}\lambda}$), convective flows ($\dot{H}_{\mathrm{HEX}}$), heat transfer flows ($\dot{Q}_\alpha$), and the accumulation term (ΔU_{Hex}).

The conductive flow can be modeled using Fourier's law [89]. The convective flow and the accumulation term can be expressed as:

$$\dot{H}_{\mathrm{HEX}}, z = \rho_{\mathrm{HEX}} c_{\mathrm{p,HEX}} u_{\mathrm{HEX},z} T_{\mathrm{HEX}} \Delta A_z \tag{2.81}$$

$$\Delta U_{\mathrm{HEX}} = \rho_{\mathrm{HEX}} c_{\mathrm{p,HEX}} T_{\mathrm{HEX}} \Delta V \tag{2.82}$$

and the heat transfer flow can be expressed as:

$$\dot{Q}_\alpha = \alpha_{\mathrm{HEX}} \Delta A_{\mathrm{surf}} (T_{\mathrm{HEX}} - T_{\mathrm{w}}|_{r=r_o}) \tag{2.83}$$

where A_{surf} is the surface area. Inserting equations (2.81) to (2.83) into equation (2.80) leads to the PDE describing the energy balance of the heat transfer fluid:

$$\rho_{\mathrm{HEX}} c_{\mathrm{p,HEX}} \frac{\partial T_{\mathrm{HEX}}}{\partial t} + \rho_{\mathrm{HEX}} c_{\mathrm{p,HEX}} u_{\mathrm{HEX},z} \frac{\partial T_{\mathrm{HEX}}}{\partial z} = \frac{\partial}{\partial z} \left(\lambda_{\mathrm{HEX}} \frac{\partial T_{\mathrm{HEX}}}{\partial z} \right) + \phi \alpha_{HEX} (T_{\mathrm{HEX}} - T_{\mathrm{w}}|_{r=r_o}) \tag{2.84}$$

if the terms $\dot{Q}_{\mathrm{HEX},\lambda,z+\mathrm{dz}}$ and $\dot{H}_{\mathrm{HEX},z+\mathrm{dz}}$ are approximated using the Taylor series (see equation (2.47) and (2.48)). The PDE was derived only considering the area in which the heat transfer fluid flows in the shell of the tube bundle and not the entire area. The coefficient ϕ represents the surface to volume ratio, which relates the surface that is available for heat transfer with the volume of the fluid. In order to estimate ϕ, a unit cell of the tube bundle is considered as noted in Figure 2.20 by the dotted line. The area of the equilateral triangle is:

$$A_\Delta = \frac{1}{2} \cdot 1.25 \cdot d_o \cdot h = \frac{\sqrt{3}}{4} \cdot 1.25^2 \cdot d_o^2 \tag{2.85}$$

Since the entire area is not penetrated by the heat transfer fluid, the area of the tubes within the triangle must be subtracted. The resulting area and volume are:

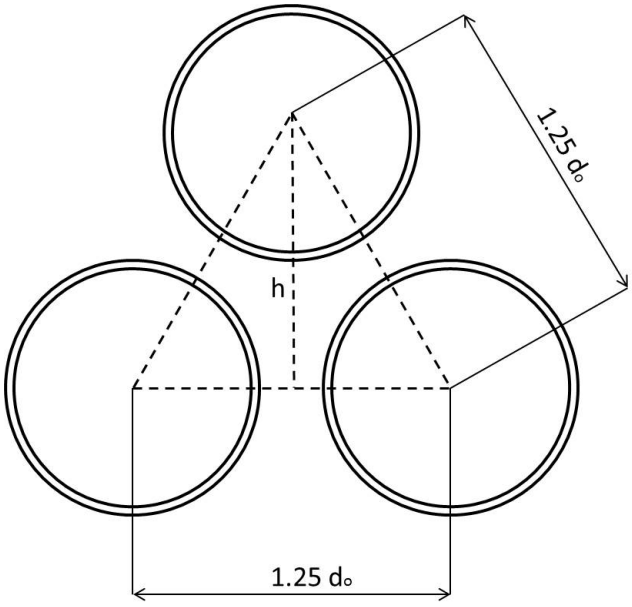

Figure 2.20: Schematic representation of the tube layout. The dotted line represents the unit cell for the estimation of the surface to volume ratio ϕ. The distance between each center point is 1.25 d_o.

$$\begin{aligned} A_{\mathrm{HEX}} &= A_{\Delta} - A_{\mathrm{circ}} = \frac{\sqrt{3}}{4} \cdot 1.25^2 \cdot d_o^2 - 3 \cdot \frac{60^\circ}{360^\circ} \cdot \pi \cdot r_o^2 \\ &= \frac{d_o^2}{4} \cdot \left(\sqrt{3} \cdot 1.25^2 - \frac{\pi}{2} \right) \end{aligned} \tag{2.86}$$

$$V_{\mathrm{HEX}} = A_{\mathrm{HEX}} \cdot H \tag{2.87}$$

The surface of the tubes in the unit cell is:

$$A_{\mathrm{surf}} = 3 \cdot \frac{60^\circ}{360^\circ} \cdot \pi \cdot d_o \cdot H = \frac{1}{2} \cdot \pi \cdot d_o \cdot H \tag{2.88}$$

which leads to the following equation for ϕ:

$$\phi = \frac{A_{\mathrm{surf}}}{V_{\mathrm{HEX}}} = \frac{\pi}{r_o \cdot \left(\sqrt{3} \cdot 1.25^2 - \frac{\pi}{2} \right)} \tag{2.89}$$

The velocity $u_{\mathrm{HEX},z}$ is calculated from the mass flow as follows:

$$u_{\mathrm{HEX},z} = \frac{\dot{M}_{\mathrm{HEX},z}}{\rho_{\mathrm{HEX}}(T_{\mathrm{HEX}}) \cdot A_{\mathrm{HEX,tube}}} \tag{2.90}$$

The area $A_{\mathrm{HEX,tube}}$ represents the area of the heat exchanging fluid per tube and can be calculated using the following equation:

$$A_{\mathrm{HEX,tube}} = \frac{\pi \cdot d_o \cdot H}{\phi \cdot H} = \frac{\pi \cdot d_o}{\phi} \tag{2.91}$$

2.3.1.4 Boundary conditions

In order to simulate the cyclic process, boundary conditions (B.C.) are required. Each tube bundle adsorber will change its boundary conditions according to the current step. Therefore, only one adsorber needs to be simulated since each adsorber will undergo the same steps.

Adsorption

The feed gas passes through the tube bundle adsorber from bottom to top during adsorption. The heat that is released during the adsorption step is transferred through the wall to the heat transfer fluid. The heat transfer fluid flows in a co-current manner in order to remove the heat upwards from the adsorption front. A counter-current flow would lead to a heating of the bed that has been saturated with the adsorptive which would lead to a reduction of the capacity. Therefore, a counter-current flow is not adequate during adsorption. The boundary conditions during the adsorption step can be taken from Table 2.5.

Heating/desorption

The boundary conditions during the heating/desorption step are tabulated in Table 2.6. As shown in Table 2.6, no gas is passed through the tube bundle adsorber during the heating/desorption step and the adsorbent bed is heated indirectly. The required heat is transferred from the heat transfer fluid to the adsorbent bed. In order to avoid a pressure rise and also in order to remove the desorbed component the pressure inside the bed is controlled.

Cooling+pressurization

The adsorbent bed transfers its heat through the tube wall to the adsorbent bed during the cooling+pressurization step. Since a temperature drop would cause a pressure drop in a closed vessel, some of the gas that leaves the tube bundle during the adsorption step is sent to the tube bundle that is undergoing the cooling+pressurization step. Since only one adsorber is being simulated, the result of the adsorption step must be stored and then used as input during the cooling+pressurization step. This is done by averaging the concentration of the adsorptive i at the outlet of the adsorber undergoing the adsorption step and then using this value as input for the cooling+pressuriztion step, as shown in Table 2.7.

Table 2.5: Boundary conditions for the adsorption step in the process cycle.

Axial B.C.	Radial B.C.
Adsorbent bed and interstitial gas	
$T\|_{z=0} = T_0$	$-\lambda_{\text{eff},r}\frac{\partial T}{\partial r}\|_{r=0} = 0$
$-\lambda_{\text{eff},z}\frac{\partial T}{\partial z}\|_{z=H} = 0$	$-\mathbf{n} \circ \left(-\lambda_{\text{eff},r}\frac{\partial T}{\partial r}\|_{r=r_i}\right) = \alpha_{\text{w}}(T_{\text{w}} - T)$
$c_{\text{i}}\|_{z=0} = \frac{y_{\text{i,in}} \cdot p}{\mathbb{R} \cdot T}$	$-\mathbf{n} \circ \left(-D_{\text{eff},r}\frac{\partial c_{\text{i}}}{\partial r} + u_r \cdot c_{\text{i}}\right)\|_{r=0} = 0$
$-D_{\text{eff},z}\frac{\partial c_{\text{i}}}{\partial z}\|_{z=0} = 0$	$-\mathbf{n} \circ \left(-D_{\text{eff},r}\frac{\partial c_{\text{i}}}{\partial r} + u_r \cdot c_{\text{i}}\right)\|_{r=r_i} = 0$
$u_z\|_{z=0} = \frac{\dot{V}_n \cdot p_n \cdot T_0}{A_{\text{tube}} \cdot p \cdot T_n}$	$u_r\|_{r=0} = 0$
$p\|_{z=H} = p_\infty$	$u_r\|_{r=r_i} = 0$
Tube wall	
$-\lambda_{\text{w}}\frac{\partial T_{\text{w}}}{\partial z}\|_{z=0} = 0$	$-\mathbf{n} \circ \left(-\lambda_{\text{w}}\frac{\partial T_{\text{w}}}{\partial r}\|_{r=r_i}\right) = \alpha_{\text{w}}(T - T_{\text{w}})$
$-\lambda_{\text{w}}\frac{\partial T_{\text{w}}}{\partial z}\|_{z=H} = 0$	$-\mathbf{n} \circ \left(-\lambda_{\text{w}}\frac{\partial T_{\text{w}}}{\partial r}\|_{r=r_o}\right) = \alpha_{\text{HEX}}(T_{\text{HEX}} - T_{\text{w}})$
Heat transfer fluid	
$T_{\text{HEX}}\|_{z=0} = T_0$	
$-\lambda_{\text{HEX}}\frac{\partial T_{\text{HEX}}}{\partial z}\|_{z=H} = 0$	

Table 2.6: Boundary conditions for the heating/desorption step in the process cycle.

Axial B.C.	Radial B.C.
Adsorbent bed and interstitial gas	
$-\lambda_{\text{eff},z}\frac{\partial T}{\partial z}\vert_{z=0} = 0$	$-\lambda_{\text{eff},r}\frac{\partial T}{\partial r}\vert_{r=0} = 0$
$-\lambda_{\text{eff},z}\frac{\partial T}{\partial z}\vert_{z=H} = 0$	$-\mathbf{n}\circ\left(-\lambda_{\text{eff},r}\frac{\partial T}{\partial r}\vert_{r=r_i}\right) = \alpha_{\text{w}}(T_{\text{w}} - T)$
$-D_{\text{eff},z}\frac{\partial c_{\text{i}}}{\partial z}\vert_{z=0} = 0$	$-\mathbf{n}\circ\left(-D_{\text{eff},r}\frac{\partial c_{\text{i}}}{\partial r} + u_r\cdot c_{\text{i}}\right)\vert_{r=0} = 0$
$-\mathbf{n}\circ\left(-D_{\text{eff},z}\frac{\partial c_{\text{i}}}{\partial z} + u_z\cdot c_{\text{i}}\right)\vert_{z=H} = 0$	$-\mathbf{n}\circ\left(-D_{\text{eff},r}\frac{\partial c_{\text{i}}}{\partial r} + u_r\cdot c_{\text{i}}\right)\vert_{r=r_i} = 0$
$p\vert_{z=0} = p_\infty$	$u_r\vert_{r=0} = 0$
$u_z\vert_{z=H} = 0$	$u_r\vert_{r=r_i} = 0$
Tube wall	
$-\lambda_{\text{w}}\frac{\partial T_{\text{w}}}{\partial z}\vert_{z=0} = 0$	$-\mathbf{n}\circ\left(-\lambda_{\text{w}}\frac{\partial T_{\text{w}}}{\partial r}\vert_{r=r_i}\right) = \alpha_{\text{w}}(T - T_{\text{w}})$
$-\lambda_{\text{w}}\frac{\partial T_{\text{w}}}{\partial z}\vert_{z=H} = 0$	$-\mathbf{n}\circ\left(-\lambda_{\text{w}}\frac{\partial T_{\text{w}}}{\partial r}\vert_{r=r_o}\right) = \alpha_{\text{HEX}}(T_{\text{HEX}} - T_{\text{w}})$
Heat transfer fluid	
$T_{\text{HEX}}\vert_{z=0} = T_{\text{Hot}}$	
$-\lambda_{\text{HEX}}\frac{\partial T_{\text{HEX}}}{\partial z}\vert_{z=H} = 0$	

Table 2.7: Boundary conditions for the cooling+pressurization step in the process cycle.

Axial B.C.	Radial B.C.
Adsorbent bed and interstitial gas	
$-\lambda_{\text{eff},z}\frac{\partial T}{\partial z}\vert_{z=H} = 0$	$-\lambda_{\text{eff},r}\frac{\partial T}{\partial r}\vert_{r=0} = 0$
$T\vert_{z=H} = T_0$	$-\mathbf{n}\circ\left(-\lambda_{\text{eff},r}\frac{\partial T}{\partial r}\vert_{r=r_i}\right) = \alpha_{\text{w}}(T_{\text{w}} - T)$
$-\mathbf{n}\circ\left(-D_{\text{eff},z}\frac{\partial c_{\text{i}}}{\partial z} + u_z\cdot c_{\text{i}}\right)\vert_{z=0} = 0$	$-\mathbf{n}\circ\left(-D_{\text{eff},r}\frac{\partial c_{\text{i}}}{\partial r} + u_r\cdot c_{\text{i}}\right)\vert_{r=0} = 0$
$c_{\text{i}}\vert_{z=H} = \bar{c}_{\text{i,outlet ads}}$	$-\mathbf{n}\circ\left(-D_{\text{eff},r}\frac{\partial c_{\text{i}}}{\partial r} + u_r\cdot c_{\text{i}}\right)\vert_{r=r_i} = 0$
$u_z\vert_{z=0} = 0$	$u_r\vert_{r=0} = 0$
$p\vert_{z=H} = p_\infty$	$u_r\vert_{r=r_i} = 0$
Tube wall	
$-\lambda_{\text{w}}\frac{\partial T_{\text{w}}}{\partial z}\vert_{z=0} = 0$	$-\mathbf{n}\circ\left(-\lambda_{\text{w}}\frac{\partial T_{\text{w}}}{\partial r}\vert_{r=r_i}\right) = \alpha_{\text{w}}(T - T_{\text{w}})$
$-\lambda_{\text{w}}\frac{\partial T_{\text{w}}}{\partial z}\vert_{z=H} = 0$	$-\mathbf{n}\circ\left(-\lambda_{\text{w}}\frac{\partial T_{\text{w}}}{\partial r}\vert_{r=r_o}\right) = \alpha_{\text{HEX}}(T_{\text{HEX}} - T_{\text{w}})$
Heat transfer fluid	
$T_{\text{HEX}}\vert_{z=0} = T_0$	
$-\lambda_{\text{HEX}}\frac{\partial T_{\text{HEX}}}{\partial z}\vert_{z=H} = 0$	

2.4 Parameter estimation

To estimate model parameters a statistical approach can be used since experimental measurements have an uncertainty [99]. Therefore, if one assumes that the experimental uncertainties are normally distributed with the standard deviation σ_i the optimal model parameters will be those that show the maximum probability at the surroundings $\Delta\theta_i$. The probability can be written as [99]:

$$\begin{aligned} P &\propto \prod_{i=1}^{N} \left[\exp\left(-\frac{1}{2} \left(\frac{\theta_i - \theta_{i,\mathrm{model}}(\mathbf{p})}{\sigma_i} \right)^2 \right) \Delta\theta_i \right] \\ &\propto \exp\left(-\frac{1}{2} \sum_{i=1}^{N} \left(\frac{\theta_i - \theta_{i,\mathrm{model}}(\mathbf{p})}{\sigma_i} \right)^2 \right) \cdot \prod_{i=1}^{N} \Delta\theta_i \end{aligned} \tag{2.92}$$

where $\mathbf{p}$ is the parameter vector; the maximal probability will be achieved if the term in the exponential function is minimized. In other words, the maximum probability will be reached if the least square error is minimized [99, 100]:

$$\sum_{i=1}^{N} \left(\frac{\theta_i - \theta_{i,\mathrm{model}}(\mathbf{p})}{\sigma_i} \right)^2 \rightarrow \min \tag{2.93}$$

Numerical routines such as the Gauß-Newton-routine are normally used to solve the minimization problem for nonlinear systems.

3 Experimental setup and materials

The experimental setup used to measure the heat transfer characteristics of the adsorbent bed and the adsorption experiments are presented in this chapter. The materials that were used are also described in the following sections.

3.1 Materials

3.1.1 Adsorbent

The zeolite used in this work is an NaX zeolite, which is also known as 13X zeolite. 13X has a high capacity for CO_2; however, in this process a high selectivity is also desired to primarily remove CO_2. A low selectivity would lead to larger beds and to a reduced purity of the recovered CO_2 if the conventional adsorption schedule is used. As shown in Figure 3.1, this zeolite shows a high selectivity for CO_2 over N_2, especially at low pressures. At high pressures, the selectivity is reduced as illustrated in Figure 3.1. Nevertheless, the selectivity is still high which makes it a feasible candidate. The structural properties of this zeolite are tabulated in Table 3.1.

Table 3.1: Structural proprieties of the 13X used in this work

Property	Value
Micro pore volume in $^{ml}/_{g}$	0.263
Micro pore area in $^{m^2}/_{g}$	589
Specific surface (BET) in $^{m^2}/_{g}$	619
Mean particle diameter in mm	2.2
Bulk density in $^{kg}/_{m^3}$	683

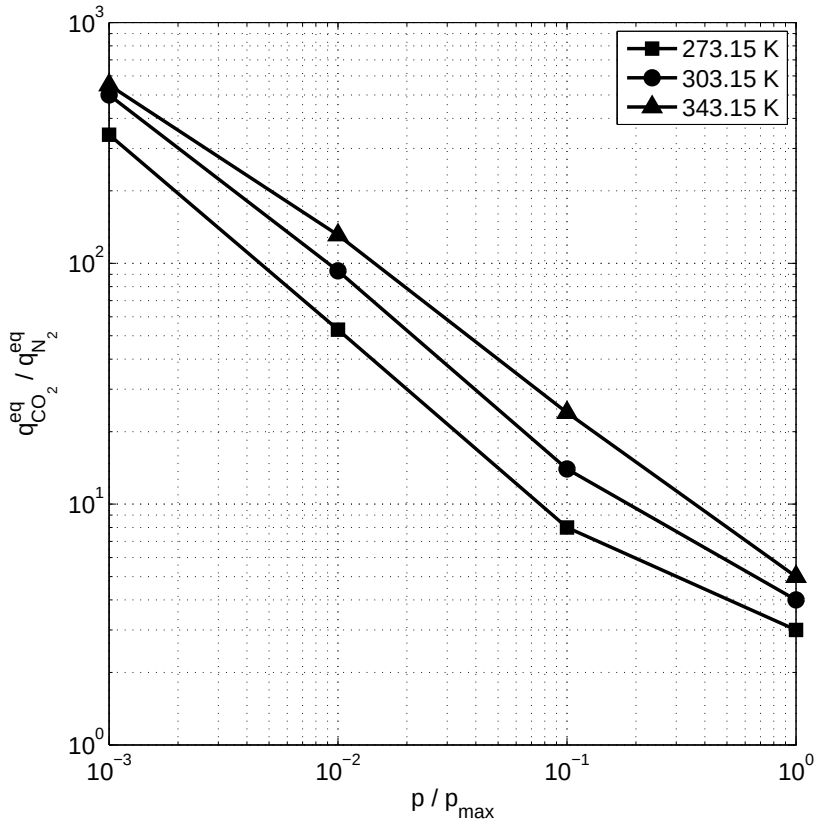

Figure 3.1: Selectivity CO_2/N_2 of the 13X used in this work.

3.1.2 Flue gas

The simulated flue gas that is used in this work consists of a dry mixture of N_2 (99.999%) and CO_2 (99.995%). The compositions that are used in this work are shown in Table 3.2. It is worth mentioning that the flue gas that is emitted by a power plant is saturated with water. Water will have a negative impact on the CO_2 separation process if a conventional zeolite is used since the CO_2 capacity is significantly reduced in the presence of water. Nevertheless, since the main goal of this work is to investigate the feasibility of the indirectly heated and cooled process for separating CO_2, it is a valid assumption to initially consider a dry flue gas, but, it must be considered that water will have to be removed on an industrial scale using either a dehydration unit (TSA-unit), a layered bed inside of the tube bundle, or another method if 13X is used. The first composition simulates a typical flue gas emitted by a coal fired power

Table 3.2: Simulated flue gas compositions that are used in this work

Component	Flue gas 1	Flue gas 2
N_2 in %	84.8	95
CO_2 in %	15.2	5

plant. The second composition simulates a flue gas emitted by a natural gas power plant.

For the heat transfer experiments and for the activation and regeneration of the adsorbent bed, only N_2 is used.

3.2 The experimental setup

In order to investigate the heat transfer characteristics of the adsorbent bed and the adsorption, a multipurpose experimental setup must be used. This experimental setup will need to allow the defining of different heating and cooling temperatures. In addition, a feed gas dosing system that enables different compositions is required. A CO_2 analysis unit with a wide range is also needed since the goal is to recover high purity CO_2. Therefore, an existing experimental setup for investigating high pressure TSA processes was modified. A schematic representation of the modified experimental setup that was used in this work is shown in Figure 3.2. The experimental setup consists of three major components: the gas supply station, the adsorber, and the thermal conductivity detector (TCD), which measures the CO_2 composition. The gas is passed from the gas supply station to the adsorber after passing through the three-way-valves, which gives the direction in which the adsorber will be flowed through. In addition to the main flow path (bold lines), there is a second one that is used for the analytics. A gas selector selects the position from which the gas is analyzed inlet, outlet, or before gas meter. The TCD, then determines the concentration of CO_2 in the gas. The three main components are further detailed in the following sections.

3.2.1 Gas supply station

The gas supply station consists of several mass flow controllers (MFCs) that are connected to a gas cylinder with a specific pure component. With these MFCs the exact amount of N_2 and CO_2 can be adjusted. The gases are then passed to a mixing tube where the desired concentration is reached. Afterwards the gas mixture is sent to the experimental setup. Relatively small streams can be reached since the superficial velocity of the feed gas cannot be set too high because of thermal inlet effects and because otherwise the residence time during adsorption would be too low. Table 3.3 gives the amount of N_2 and CO_2 that were adjusted in order to reach the feed concentrations of the different simulated flue gases used in this work.

Table 3.3: Amount of N_2 and CO_2 used during the adsorption experiments

Component / concentration	Flue gas 1	Flue gas 2
N_2 in $^{Nl}/_{min}$	0.79	0.92
CO_2 in $^{Nl}/_{min}$	≈0.142	≈ 0.048
y_{CO_2} in %	≈15.2	≈5

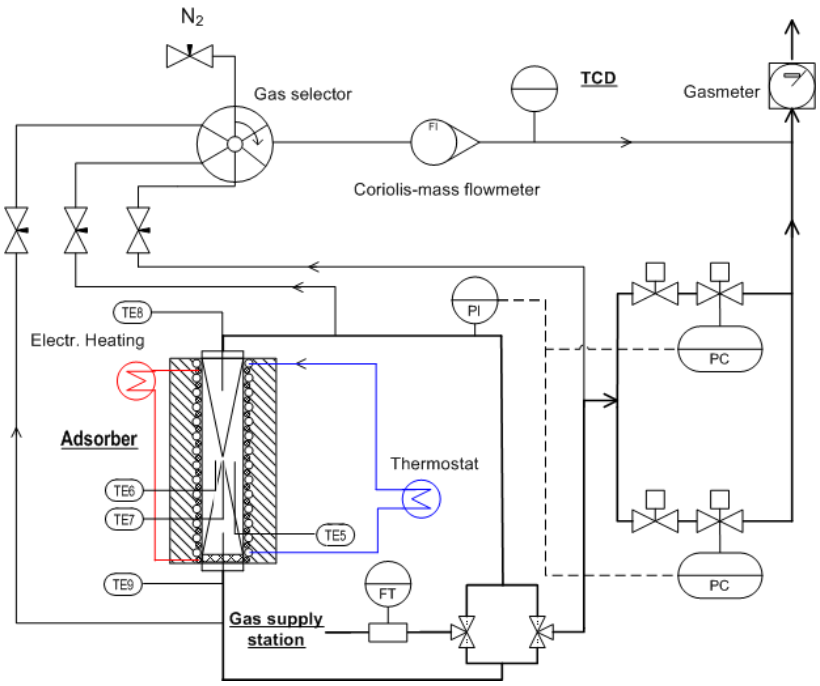

(a) Schematic representation

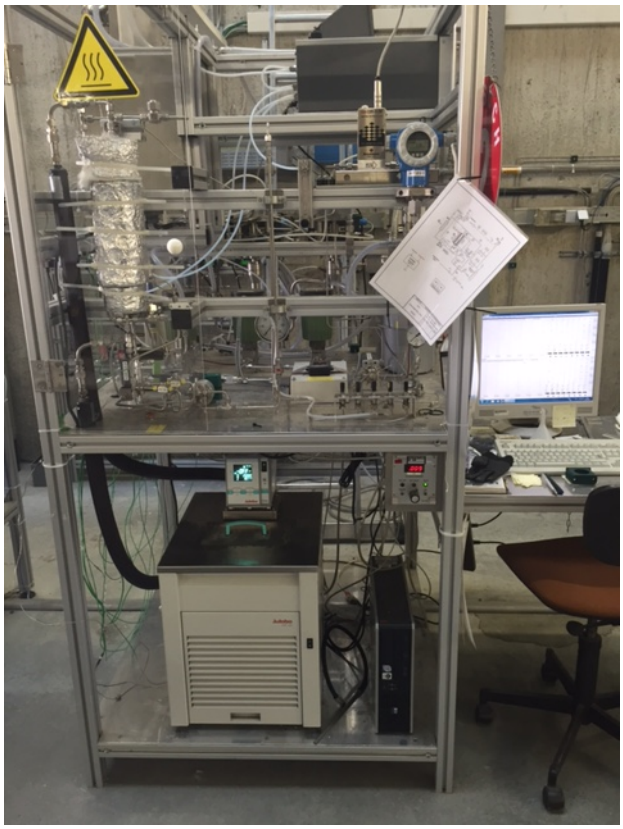

(b) The experimental setup

Figure 3.2: Experimental setup and its components

3.2.2 Thermal Conductivity Detector

The TCD (AO2020 series with Caldos27, *ABB*) consists of two chambers, a reference chamber and the measurement chamber; both chambers are maintained at the same temperature. When the gas that comes into the measurement chamber is changed, the system must change its voltage in order to reach the temperature of the reference cell. This change in voltage can be measured and correlated linearly with the concentration of the component to be measured. The TCD can only be used for binary gas mixtures with significant different heat conductivities. Since only a binary gas mixture has been considered in this work and both components have significantly different heat conductivities ($\lambda_{N_2}/\lambda_{CO_2}$ ≈1.6 at 30°C and 1 bar), the TCD represents an ideal method for measuring the CO_2 concentration continuously. The inlet concentration of CO_2 is varied for the different adsorption experiments and during the desorption step, high CO_2 concentrations are expected. Therefore, a calibration in a wide range is necessary. For the adsorption experiments, a range of: 0-100 % is used. Such a wide range will have certain uncertainties, especially at low concentrations.

3.2.3 Adsorber

The adsorber represents the main part of the experimental setup. Since the goal of this work is to investigate an indirectly heated and cooled heat exchanger type adsorber, a single tube can be investigated. Therefore, a hollow tube was designed in which different tubes can be placed. Electrical heating was wrapped around the hollow tube in order to simulate the indirect heating. Since the aim is also to cool down the adsorber indirectly, a cooling coil was also wrapped around the hollow tube. A thermal fluid held at a constant temperature with a thermostat is passed through the cooling coil. Therefore, the tube that is filled with the adsorbent and placed inside of the hollow tube can be heated and cooled quickly. A schematic representation and a picture of the adsorber is shown in Figure 3.3. In order to avoid heat losses, insulation is wrapped around the hollow tube and around the upper and lower cap nuts, as illustrated in Figure 3.3. The geometrical characteristics of the adsorber are displayed in Table 3.4.

Figure 3.3 shows that several thermocouples were introduced in the adsorber unit. On the wall of the tube, a thin thermocouple was placed in order to measure the wall temperature. A thermocouple was also placed in the outer wall of the hollow tube to

Table 3.4: Geometrical characteristics of the adsorber tube

Parameter	Value
Material	Stainless steel
Height without cap nuts in cm	22.6
Inner diameter in mm	32
Outer diameter in mm	37

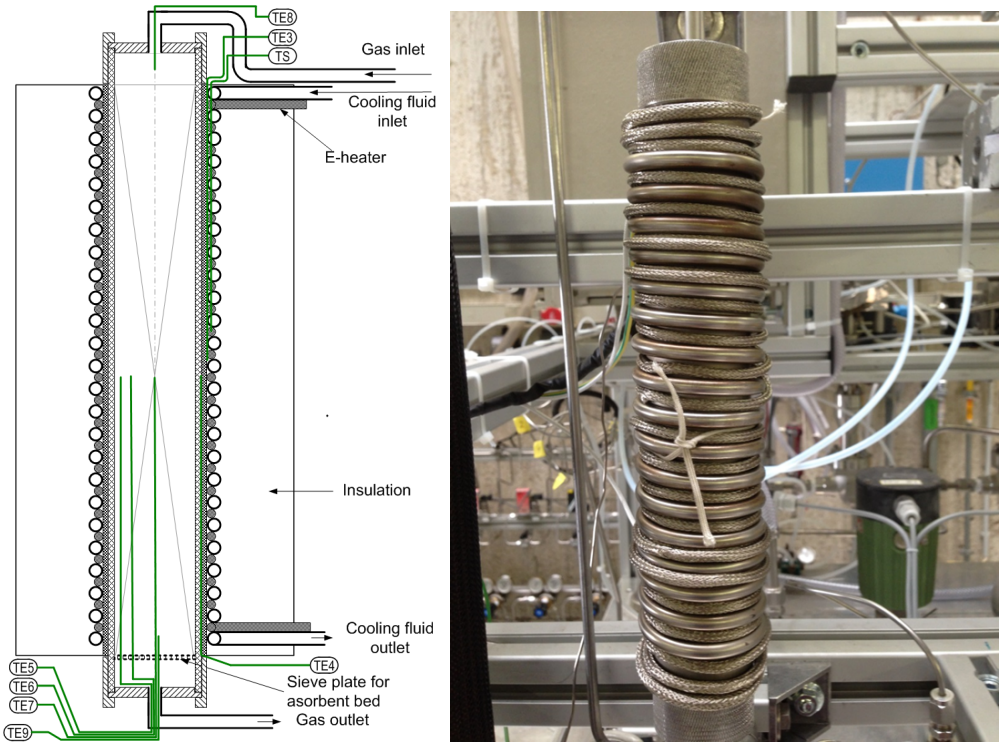

(a) Schematic representation

(b) Electrical heating and cooling coil

(c) External insulation

Figure 3.3: Adsorber

measure the exterior temperature. Five different thermocouples were placed inside the tube. With these five thermocouples, the inlet temperature, the outlet temperature and the temperature at three different radial positions can be measured. All of the

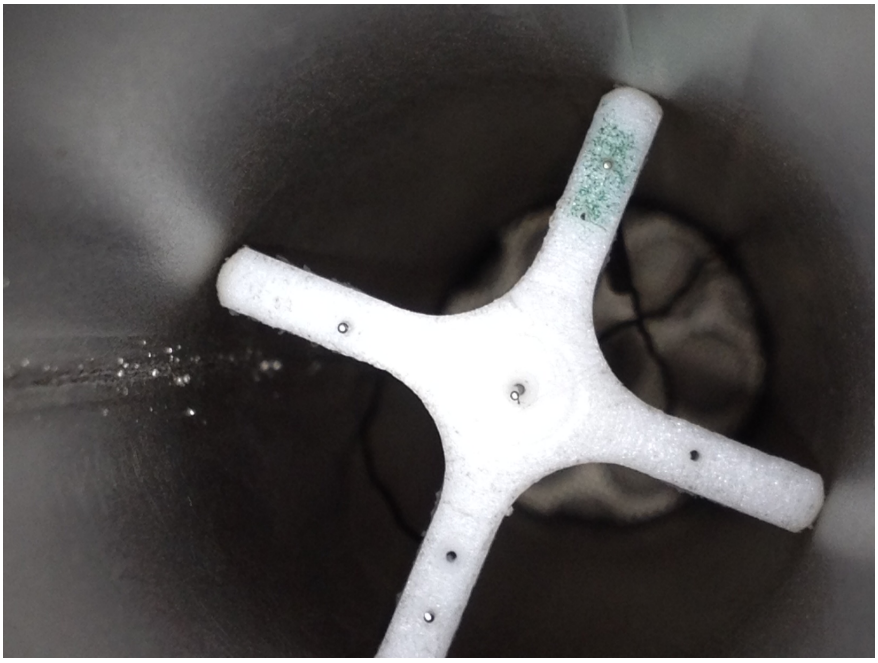

Figure 3.4: PTFE cross used to place the radial thermocouples.

thermocouples were introduced into the tube either through the top or the bottom. To position the thermocouples at different radial positions, a thin PTFE cross was made in which small holes were introduced at different radial positions; the PTFE cross is illustrated in Figure 3.4. The position of the thermocouples at different radial positions and the thermocouple at the wall and their types are tabulated in Table 3.5. In order to neglect the influence of the flow disturbance because of the PTFE cross on the temperature profiles, the feed gas is introduced from top to bottom.

Table 3.5: Position of the thermocouples that are placed at different radial positions and the thermocouple on the tube wall

Thermocouple	Axial positon / cm	Radial position / mm	Type
TE4	11.5	18.5	K
TE5	13.05	12.52	K
TE6	13.05	9.55	K
TE7	13.05	0	K

3.2.3.1 Heat losses and constant axial wall temperature

It is necessary to reduce the heat losses for the heat transfer experiments and for the adsorption experiments, since otherwise it cannot be assumed that the bed is being heated equally and symmetrically along the z-axis. This would lead to a smaller region in which the measurements could be conducted. In order to achieve a reduction of the heat losses it is necessary to insulate the adsorber unit as mentioned earlier. In

addition, it is necessary to compensate for heat losses at those positions with the major heat losses. In this case, the upper and lower cap nuts represent the parts with the highest heat losses because of their high thermal mass. To reduce the heat losses, more electrical duty is put in the upper and lower part of the hollow tube. In order to check the heat losses, an axial temperature profile is measured after reaching the stationary point. The axial temperature measurement is conducted with the thermocouple TE8, which is inserted from the top. The other thermocouples are not used during this procedure. The thermocouple is pulled 1 cm out of the adsorber tube. Subsequently, it is waited until a constant temperature reading is reached. This procedure is repeated until the thermocouple reaches the top of the adsorbent bed. Figure 3.5 illustrates the normalized axial temperature profile. At the bottom and top, the maximal temperature is not reached at the stationary point. This means that, even with the insulation and the increased electrical duty, the heat losses are not entirely compensated. Nevertheless, if the adsorbent bed is only filled between 5 cm and 17 cm one can assume a constant temperature profile and the influence of the heat losses can be significantly decreased. In order to achieve this, glass beads are filled at the bottom and top. Figure 3.6 illustrates how the adsorber tube is filled.

Since the heat transfer experiments and the adsorption experiments are not stationary experiments, but transient experiments, it is necessary to check if by placing more

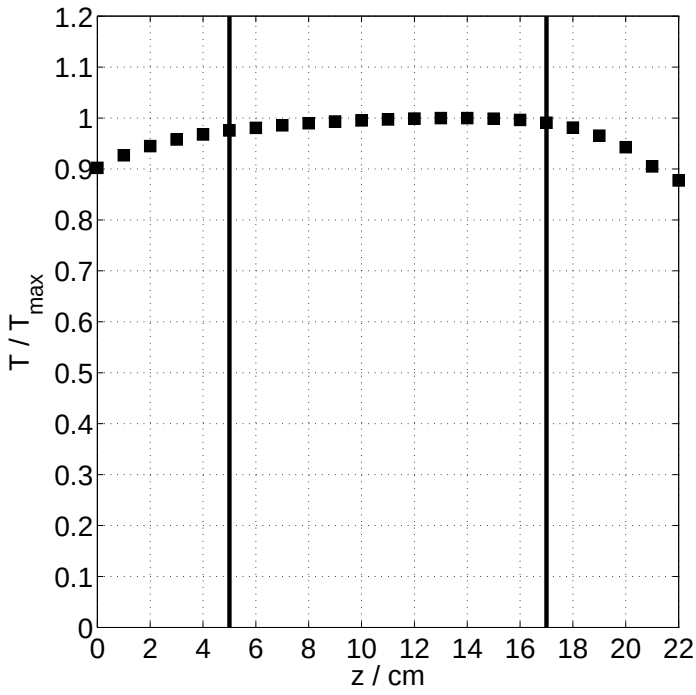

Figure 3.5: Axial temperature profile measured at the stationary point. The maximal temperature is 200 °C. The axial position represents the distance from the bottom of the tube. The region between the thick lines represent the region of the adsorbent

electrical duty at the top and bottom the assumption of constant axial temperature is still valid. This boundary condition is necessary to measure reliable temperature profiles and to validate the experiments with the numerical simulations. Therefore, two thermocouples are placed at the center of the adsorber tube at different axial positions. The axial positions are chosen such that the most important part of the bed is considered, meaning the region between the inlet and the cross. During this procedure the adsorber tube is filled with glass beads and adsorbent. The position of the thermocouples are outlined in Table 3.6. In Figure 3.7, the measured temperature profiles are shown and both temperatures are almost identical. The biggest deviation between both curves is approximately 4 K. This represents a deviation of around 5%.

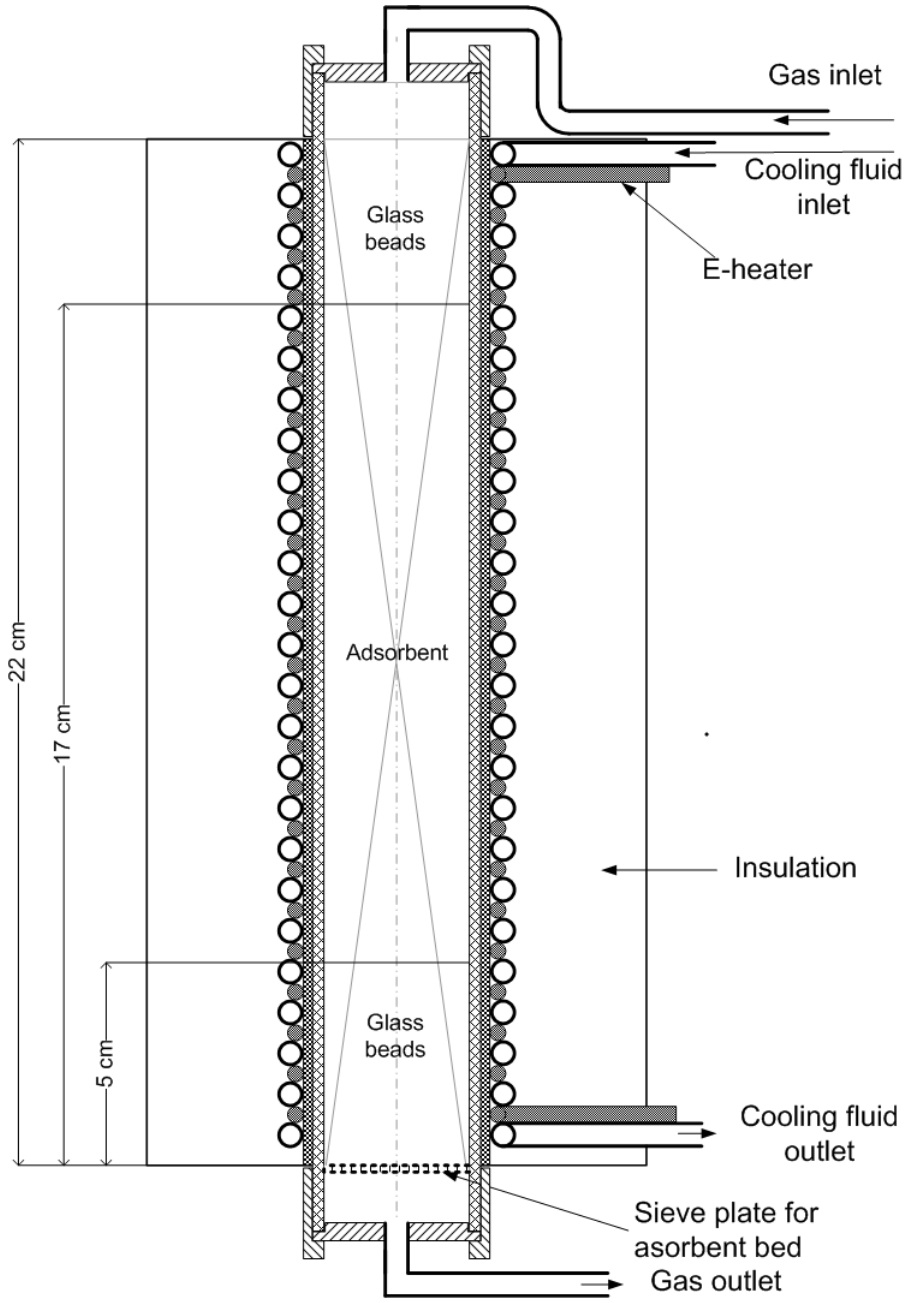

Figure 3.6: Layers inside the adsorber tube

Table 3.6: Position of the thermocouples for verifying if the assumption of constant wall temperature is valid

Thermocouple	Axial positon / cm	Radial position / mm
TE4	11.5	37
TE7	13.05	0
TE8	16.9	0

Since this deviation is only at one point and not greater than 5% it is assumed that the axial wall temperature is approximately constant over the range of interest.

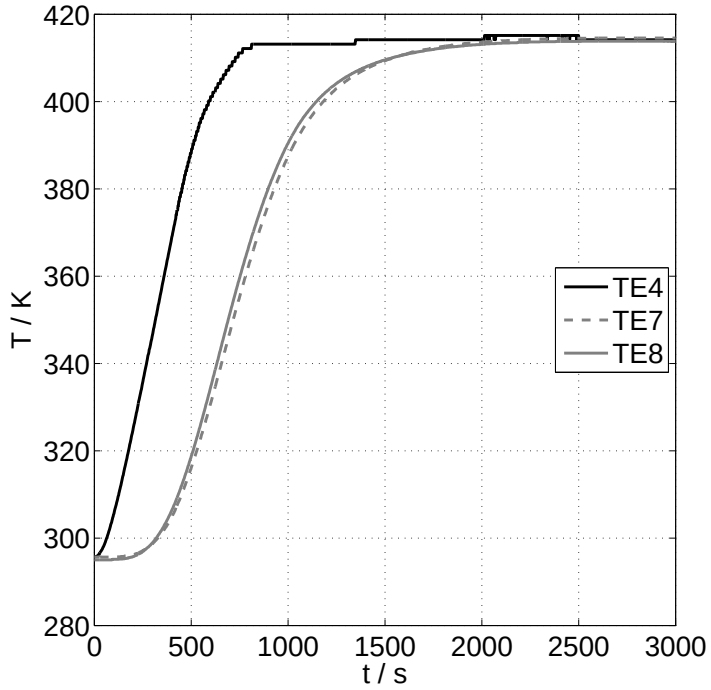

Figure 3.7: Temperature profiles at the center at different axial positions and wall temperature.

3.2.3.2 Activation of the adsorbent

To fill the adsorber tube with the adsorbent, special care is required to avoid moving the cross with the thermocouples. This means that the adsorbent will be exposed to the ambient air for a longer time. Zeolites have a high affinity towards water, which reduces the capacity for CO_2. Since the 13X will be exposed to the air for a longer period of time one can assume that water will be adsorbed by the 13X. Therefore, it is necessary to activate the bed in situ before any adsorption measurement begins. To activate the adsorbent, the packed tube is purged for several days with N_2 at high temperatures (≈230°C). The conditions for the activation are listed in Table 3.7. In

Table 3.7: Conditions for in situ activation

Parameter	Value
N_2 flow in $^{Nl}/_{min}$	≈1
Activation temperature in °C	≈230°C
time in days	≈ 7

order to determine whether the bed is fully activated, a first breakthrough curve is measured after the adsorbent bed is activated. Then, the bed is purged with N_2 again at high temperatures for a couple of hours. After the bed is cooled, a second breakthrough curve is measured and compared with the first breakthrough curve. The obtained breakthrough curves are plotted in Figure 3.8; both curves overlap meaning that the bed is fully activated.

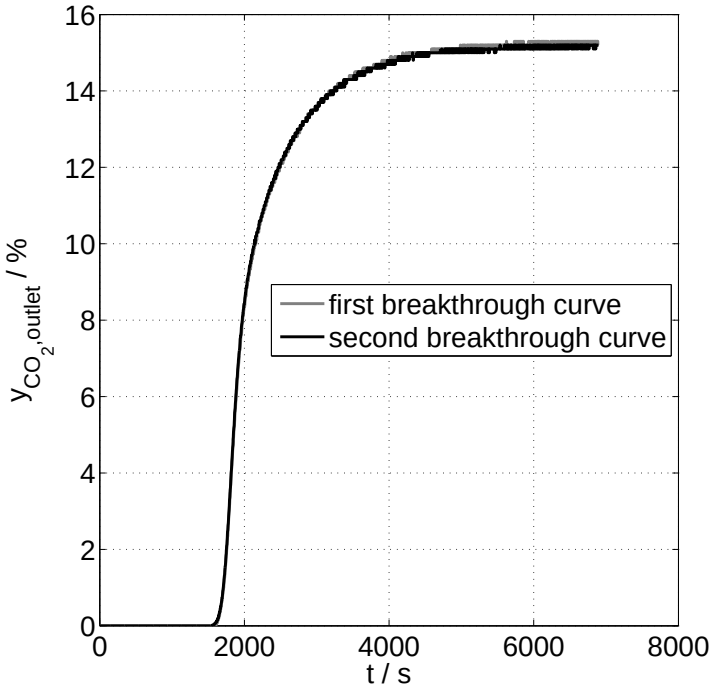

Figure 3.8: Breakthrough curves measured after activation (gray) and after having purged at high temperatures the adsorbent bed for a couple of hours (black).

3.2.4 Procedure for the heat transfer experiments

In order to measure the heat transfer characteristics, the heat transfer experiments are divided into two major parts:

- Heat transfer without convection
- Heat transfer with convection

Table 3.8: Position, type, and measurement error of the thermocouples used during the heat transfer experiments.

Thermocouple	Axial positon / cm	Radial position / mm	Type	Error in K
TE4	11.5	18.5	K	2.5
TE5	13.05	12.52	K	2.5
TE6	13.05	9.55	K	2.5
TE7	13.05	0	K	2.5
TE8	17	0	K	2.5
TE9	5.2	0	K	2.5

The procedure for both parts will be discussed in the following sections. The position of the thermocouples used during the heat transfer experiments are shown in Table 3.8.

3.2.4.1 Heat transfer without convection

For the experiments without convection the procedure is as follows:

1.) The adsorbent bed is purged with N_2 (1 $^{Nl}/_{min}$) at high temperatures (230 °C) for two hours to evacuate the adsorber unit from any impurity

2.) Next, the unit is cooled down while still purging the bed with N_2 (1 $^{Nl}/_{min}$) for two hours

3.) Before starting the experiment, the boundary condition is set in the control system:

   3.1.) The heating temperature is set for experiments with a constant wall temperature

   3.2.) The heating duty is set for experiments with constant heat duty

4.) After setting the conditions in the control system, the bed is heated for one hour and the temperatures inside the bed are recorded

5.) After the heating step is concluded, the electrical heating is turned off, the thermostat is turned on, and the bed is cooled for one hour.

6.) When the cooling step is finished, the recording of the temperatures is stopped.

3.2.4.2 Heat transfer with convection

The following procedure is used for the experiments with convection:

1.) The adsorbent bed is purged with N_2 (1 $^{Nl}/_{min}$) at high temperatures (230 °C) for two hours to evacuate the adsorber unit from any impurity

2.) Afterwards, the unit is cooled while still purging the bed with N_2 (1 $^{Nl}/_{min}$) for two hours

3.) Before starting the experiment, the N_2 flow, the pressure, and the heat duty are set in the control unit

4.) After setting the conditions, the system is pressurized to the given pressure

5.) After reaching the pressure and stable flow conditions, the electrical heating is turned on and the temperatures are recorded. The bed is heated for one hour

6.) After the heating step is concluded, the electrical heating is turned off, and the thermostat is turned on, and the bed is cooled for one hour.

7.) After the cooling step is finished, the recording of the temperatures is stopped.

3.2.5 Procedure for the adsorption experiments

During the adsorption experiments, the position of the thermocouples are kept as for the heat transfer experiments (see Table 3.8) and the following procedure is used:

1.) First the flow of CO_2 and N_2, adsorption temperature (22 °C), and pressure (1.15 bar) are set in the control system. The regeneration temperature and the number of cycles are also set.

2.) Next, the bed is regenerated at high temperatures (220 °C) and at adsorption pressure under an N_2 purge (1 $^{Nl}/_{min}$) for 150 minutes in order to remove any impurities.

3.) After the heating is finished, the bed is cooled under an N_2 purge (1 $^{Nl}/_{min}$) for 150 minutes to the adsorption temperature.

4.) When the cooling step is finished the pressure is checked. If the pressure does not represent the adsorption pressure then the bed is pressurized or depressurized to the adsorption pressure

5.) When the adsorption pressure is reached, the CO_2 valve is opened and the N_2 flow is adjusted to the value set in the first step. The gas is mixed at the gas station and sent to the adsorber unit. Furthermore, the thermostat is turned on and the temperature is set to the adsorption temperature in order to cool down the bed during adsorption.

6.) The adsorption step is conducted until 75% of the inlet concentration is reached at the outlet (breakthrough). The gas concentration is measured using the gas before the gas meter.

7.) As soon as the adsorption step finishes the thermostat is turned off, the CO_2 and N_2 valves are closed, and the electrical heating is turned on and the bed is heated for one hour. The regeneration temperature is the temperature that is set in the first step and the pressure is reduced to 1.05 bar.

8.) After the heating step, the electrical heating is turned off and the thermostat is turned on in order to cool the bed for one hour. The cooling temperature is the same as the adsorption temperature. In addition, an N_2 purge ($0.3^{Nl}/_{min}$) is used to pressurize the bed again to the adsorption pressure and to compensate the decrease of pressure during the cooling.

9.) After the cooling one cycle is completed. If the number of cycles is lower than the number of cycles given in the first step, then Steps 4 to Step 8 are repeated.

10.) When the desired number of cycles is reached, the regeneration temperature or the inlet concentration is changed and the procedure is started again.

3.2.6 Reproducibility of the experiments

In order to determine whether the adsorption is reproducible, four identical experiments are conducted. The adsorption experiment is conducted until 75% of the inlet CO_2 concentration is measured at the outlet of the adsorber tube. This is equivalent to Step 6 in section 3.2.5. The results are illustrated in Figure 3.9; all curves overlap meaning that the experiments are reproducible.

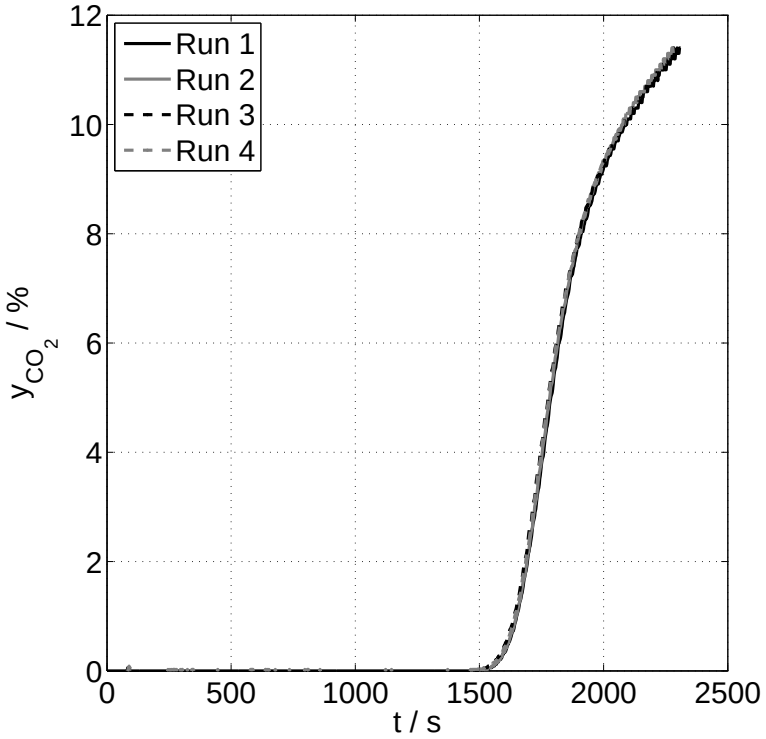

Figure 3.9: Adsorption experiments to prove the reproducibility.

3.2.7 Mass balances and errors

To calculate the recovery of CO_2 and the average purity during the heating step, it is necessary to make a mass balance. The inlet amount of CO_2 can be calculated as follows:

$$N^a_{\mathrm{CO_2,in,cycle}} = \dot{V}_{n,\mathrm{CO_2}} \cdot t_{\mathrm{ads}} \cdot \frac{p_n}{\mathbb{R} \cdot T_n} \tag{3.1}$$

The amount exiting the adsorber during the adsorption step must be calculated using the partial breakthrough curve and the gas meter. Since the gas meter only has a resolution of 0.1 l, it is necessary to assume that the volume flow is constant during the time that it takes to measure 0.1 liter. This is an estimation of the actual volume flow and must be considered a probable error source. The volume flow of CO_2 can then be calculated as follows:

$$\dot{V}_{\mathrm{CO_2,out}} = \begin{pmatrix} \frac{0.1l-0l}{t_{0.1l}-t_0} \cdot y_{\mathrm{CO_2,out}}(t) \;\; \text{for} \;\; t \leq t_{0.1l} \\ \frac{0.2l-0.1l}{t_{0.2l}-t_{0.1l}} \cdot y_{\mathrm{CO_2,out}}(t) \;\; \text{for} \;\; t_{0.1l} < t \leq t_{0.2l} \\ .... \\ .... \end{pmatrix} \tag{3.2}$$

The amount of CO_2 exiting during the adsorption step can be calculated by integrating the volume flow:

$$N^a_{\mathrm{CO_2,out,cycle}} = \frac{p_\infty}{\mathbb{R} \cdot T_\infty} \cdot \int_{t_0}^{t_{\mathrm{ads}}} \dot{V}_{\mathrm{CO_2,out}} \mathrm{d}t \tag{3.3}$$

For the heating step, the same procedure for calculating the outlet CO_2 flow is used, which leads to the following:

$$N^h_{\mathrm{CO_2,out,cycle}} = \frac{p_\infty}{\mathbb{R} \cdot T_\infty} \cdot \int_{t_0}^{t_{\mathrm{des}}} \dot{V}_{\mathrm{CO_2,out,des}} \mathrm{d}t \tag{3.4}$$

The volume flow $\dot{V}_{\mathrm{CO_2,out,des}}$ during the heating step is also calculated using equation (3.2). It has to be kept in mind, that in this case the use of the gas meter represent a possible error source, since during the heating step a non-constant flow is expected. The reason lies in the pressure since the pressure relief valves will only open if the pressure inside the system is increased. This means, that at the beginning of the heating the flow exiting the adsorber will increase. As the temperature reaches the regeneration temperature the magnitude of the pressure rise starts to decrease. This leads to a decrease of the flow at the outlet of the adsorber. When the system reaches a thermal equilibrium just a very small flow will exit the system. Therefore, an error can be made while balancing the CO_2 since the resolution of the gas meter is 0.1 l.

The N_2 flow exiting the experimental setup is quantified as follows:

$$N^h_{\mathrm{N_2,out,cycle}} = \frac{p_\infty}{\mathbb{R} \cdot T_\infty} \cdot \int_{t_0}^{t_{\mathrm{des}}} \dot{V}_{\mathrm{N_2,out,des}} \mathrm{d}t \tag{3.5}$$

with $\dot{V}_{\mathrm{N_2,out,des}}$ as:

$$\dot{V}_{\mathrm{N_2,out}} = \begin{pmatrix} \frac{0.1l-0l}{t_{0.1l}-t_0} \cdot (1 - y_{\mathrm{CO_2,out}}(t)) \ \text{ for } \ t \leq t_{0.1l} \\ \frac{0.2l-0.1l}{t_{0.2l}-t_{0.1l}} \cdot (1 - y_{\mathrm{CO_2,out}}(t)) \ \text{ for } \ t_{0.1l} < t \leq t_{0.2l} \\ .... \\ .... \end{pmatrix} \tag{3.6}$$

The recovery of CO_2 during the heating step can then be calculated as follows:

$$\mathrm{Recovery} = \frac{N^h_{\mathrm{CO_2,out,cycle}}}{N^a_{\mathrm{CO_2,in,cycle}}} \tag{3.7}$$

and the average purity of the recovered CO_2 as:

$$\bar{y}_{\mathrm{CO_2}} = \frac{N^h_{\mathrm{CO_2,out,cycle}}}{N^h_{\mathrm{CO_2,out,cycle}} + N^h_{\mathrm{N_2,out,cycle}}} \tag{3.8}$$

The error caused by balancing the system is going to be quantified in the next section.

3.2.8 Error calculations

As mentioned before, some uncertainties have to be expected because of the measuring instruments used. These uncertainties will influence the calculated values of the experimental CO_2 recovery and average purity. The methodical and statistical uncertainties of the units that have an impact on the calculated values can be taken from Table 3.9. To calculate the total methodical uncertainty the addition of the individual uncertainties can be taken:

$$s_{\mathrm{methodical,total}} = \sum_{i=1}^{N} s_{\mathrm{methodical,i}} \tag{3.9}$$

Table 3.9: Uncertainties of the measuring instruments. The abbreviations m.v. and e.v means current measured value and value of the measurement range

Measuring quantity	Unit	Methodical	Statistical	Reference
CO_2 concentration	TCD	2%	1%	[101]
CO_2,N_2 flow	MFC	±0.5% m.v. ± 0.1% e.v	± 0.2% m.v.	[102]

The total uncertainty for each calculated value is the addition of the methodical and statistical uncertainty:

$$\Delta\text{Recovery}_{\text{tot}} = s_{\text{methodical,total}} + \Delta\text{Recovery} \tag{3.10}$$

$$\Delta\bar{y}_{\text{CO}_2,\text{tot}} = s_{\text{methodical,total}} + \Delta\bar{y}_{\text{CO}_2} \tag{3.11}$$

The calculation of the statistical uncertainty for the recovery and average purity requires first the statistical uncertainties of the individual contributions, meaning the statistical contributions of:

- $N^a_{\text{CO}_2,\text{in,cycle}}$
- $N^h_{\text{CO}_2,\text{out,cycle}}$
- $N^h_{\text{N}_2,\text{out,cycle}}$

The statistical uncertainty of $N^a_{\text{CO}_2,\text{in,cycle}}$ can be calculated using the statistical uncertainty of the MFC:

$$\Delta N^a_{\text{CO}_2,\text{in,cycle}} = 0.002 \cdot \dot{N}_{\text{CO}_2,\text{flow}} \cdot t_{\text{ads}} \tag{3.12}$$

For calculating the uncertainty of $N^h_{\text{CO}_2,\text{out,cycle}}$ and $N^h_{\text{N}_2,\text{out,cycle}}$ first the integration has to be written as a sum. Since the trapezoidal numerical integration in Matlab® has been used the integration can be written as [103]:

$$F = \int_a^b f(x) = \frac{1}{2}\sum_{n=1}^{N}(x_{n+1} - x_n)\left[f(x_n) + f(x_{n+1})\right] \tag{3.13}$$

Using the Gaussian error propagation which can be written as [104]:

$$s = \sqrt{\left(\frac{\partial f}{\partial x_i}\cdot\Delta x_i\right)^2 + ... + \left(\frac{\partial f}{\partial x_n}\cdot\Delta x_n\right)^2} \tag{3.14}$$

and the statistical uncertainty of the TCD leads to the following for $\Delta N^h_{\text{CO}_2,\text{out,cycle}}$ and $N^h_{\text{N}_2,\text{out,cycle}}$:

$$\Delta N^h_{\text{CO}_2/\text{N}_2,\text{out,cycle}} = \frac{p_\infty}{\mathbb{R}\cdot T_\infty} \sqrt{\left(\Delta_1\cdot\frac{1}{2}(t_2 - t_1)\right)^2 + ... + \left(\Delta_N\cdot\frac{1}{2}(t_{N+1} - t_{N-1})\right)^2} \tag{3.15}$$

The uncertainty for each element Δ_i is:

$$\Delta_i = \dot{V}_{\text{CO}_2/\text{N}_2,\text{out,des,i}} \cdot 0.01 \tag{3.16}$$

The uncertainty that would be obtained for the CO_2 recovery and average purity can then be calculated as follows by using equation (3.14):

$$\Delta\text{Recovery} = \sqrt{\left(\frac{\Delta N^h_{\text{CO}_2,\text{out,cycle}}}{N^a_{\text{CO}_2,\text{in,cycle}}}\right)^2 + \left(\frac{N^h_{\text{CO}_2,\text{out,cycle}}}{(N^a_{\text{CO}_2,\text{in,cycle}})^2} \cdot \Delta N^a_{\text{CO}_2,\text{in,cycle}}\right)^2} \tag{3.17}$$

$$\Delta\bar{y}_{\text{CO}_2} = \sqrt{\left(A_3 \Delta N^h_{\text{CO}_2,\text{out,cycle}}\right)^2 + \left(A_4 \Delta N^h_{\text{N}_2,\text{out,cycle}}\right)^2} \tag{3.18}$$

$$A_3 = \frac{1}{N^h_{\text{CO}_2,\text{out,cycle}} + N^h_{\text{N}_2,\text{out,cycle}}} - \frac{N^h_{\text{CO}_2,\text{out,cycle}}}{(N^h_{\text{CO}_2,\text{out,cycle}} + N^h_{\text{N}_2,\text{out,cycle}})^2} \tag{3.19}$$

$$A_4 = \frac{N^h_{\text{CO}_2,\text{out,cycle}}}{(N^h_{\text{CO}_2,\text{out,cycle}} + N^h_{\text{N}_2,\text{out,cycle}})^2} \tag{3.20}$$

The highest calculated uncertainties for the adsorption experiments are listed in Table 3.10. The total uncertainty is between 29% and 31% for the recovery and between 21% and 23% for the average purity. It is clear that the measuring instruments have an impact on the results. As mentioned earlier, the experimental setup that is modified is designed for classical TSA processes at high pressures. The fact that low pressures were used during this investigation leads to uncertainties when measuring, especially the volume flow since the error caused by estimating it will propagate during the numerical integration. Furthermore, during the desorption step no purge flow is used, which leads to a small fluctuating flow caused by the temperature increase. It is difficult to accurately measure this small fluctuating flow. This small flow will also have a significant impact on the TCD. Nevertheless, considering the difficulty that is present for measuring flows at almost ambient pressure and the influence of small flows on the TCD, higher uncertainties must be considered. The obtained results are

Table 3.10: Highest calculated uncertainties. The temperature represents the regeneration temperature T_{Hot}.

Uncertainty	5% CO_2 and 200 °C	15% CO_2 and 200 °C
$s_{\text{methodical,total}}$ in %	6	5
$\frac{\Delta\text{Recovery}}{\text{Recovery}}$ in %	25	24
$\frac{\Delta\bar{y}_{\text{CO}_2}}{\bar{y}_{\text{CO}_2}}$ in %	17	16
Total Recovery in%	**31**	**29**
Total average purity in %	**23**	**21**

therefore acceptable, since the error is below 30%. The experiments can also be used to determine important adsorption parameters, since for the determination the CO_2, concentration profiles and the temperature profiles are only required. These variables are measured continuously and with higher accuracy than the volume flow.

4 Experimental results and simulations

The results of the experimental measurements regarding the heat transfer characteristics, the adsorption characteristics, and the obtained parameters are presented in the following sections. The adsorption isotherm used for the numerical simulations is also discussed.

For the numerical simulations, the commercial software COMSOL Multiphysics® (COMSOL) and LiveLink™ *for* Matlab® (LiveLink) were used. COMSOL is a numerical software which can solve algebraic equations and differential equations; 2D and 3D models can be solved. The LiveLink couples COMSOL with Matlab® (Matlab). This enables the use of the numerical solvers of COMSOL and the functionalities of Matlab.

To investigate the heat transfer and adsorption characteristics, a 2D axial symmetrical model is used. This 2D model represents the tube used during the experiments, which is filled with adsorbent. The entire tube is not represented in the 2D model; only the part filled with the adsorbent. Figure 4.1 shows the geometry that is implemented in COMSOL. In addition to the adsorbent bed the wall is also considered. The model equations that are implemented for the adsorbent bed correspond to the derived model equations for the adsorbent bed and the interstitial gas phase in section 2.3.1.1. No adsorption is considered and only N_2 is used as feed for the investigation of the heat transfer characteristics. To calculate model parameters, the errors of the thermocouples listed in Table 3.8 are used as standard deviation, and only TE5, TE6 and TE7 are considered in the optimization routines. The adsorption of the incoming CO_2 is

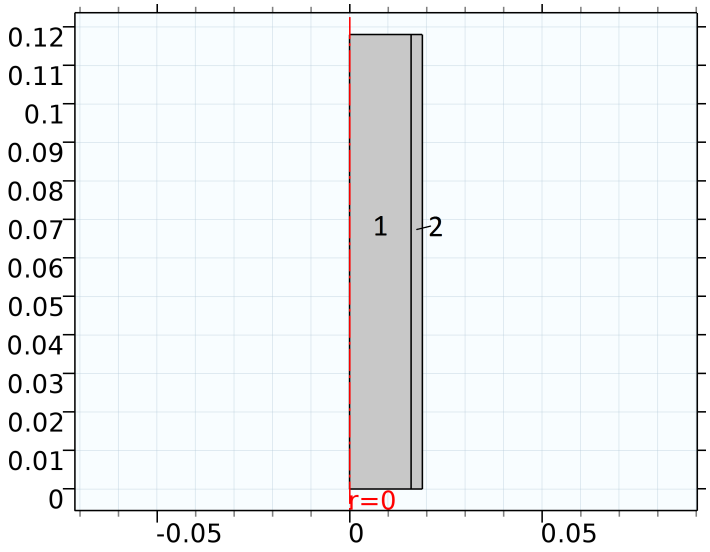

Figure 4.1: Geometry used in COMSOL Multiphysics® for the investigation of the heat transfer and adsorption characteristics. 1 represents the adsorbent bed and interstitial gas phase and 2 represents the tube wall.

considered for the investigation of the adsorption characteristics. The tube wall is modeled using the derived model for the tube wall in section 2.3.1.2. Instead of coupling heat transfer from a fluid to the tube wall, a constant temperature at the exterior surface of the wall is considered as a boundary condition. The temperature that is set at the surface represents the measured temperature of thermocouple TE4, which is the thermocouple at the exterior surface of the experimental tube. To calculate the adsorption parameters, the thermocouples inside the bed (TE5, TE6 and TE7) are used and the concentration profiles are measured by the TCD.

4.1 Heat transfer in packed beds without convection

It is crucial for the indirect heated TSA process to have substantial knowledge about the heat transfer parameters. Therefore, two different boundary conditions are used in order to investigate the heat transfer characteristics in an adsorbent bed without convection. The different boundary conditions are chosen in order to investigate whether the model parameters depend on the boundary condition.

4.1.1 Constant wall temperature

For the experiments with constant wall temperature, the procedure according to section 3.2.4.1 is used. Six different temperatures are chosen and each experiment is conducted twice. The different temperatures used are tabulated in Table 4.1. The temperature profiles for the different experiments of the first run are illustrated in Figure 4.2.

The wall temperature rises relatively fast to the value that is set in the control system. The measured temperatures inside the bed will follow the wall temperature and increase towards the temperature set in the control system. This is also expected since the boundary condition can be compared to a boundary condition of the first kind. Nevertheless, the temperatures inside the adsorbent bed react slowly to the temperature

Table 4.1: Temperatures used for the experiments with constant wall temperature. Each experiment is conducted twice.

Experiment	Wall temperature in K
1	373.15
2	393.15
3	413.15
4	433.15
5	453.15
6	473.15

change at the wall. The higher the distance to the wall, the slower the reaction to the temperature change. Since no convection is used during these experiments the

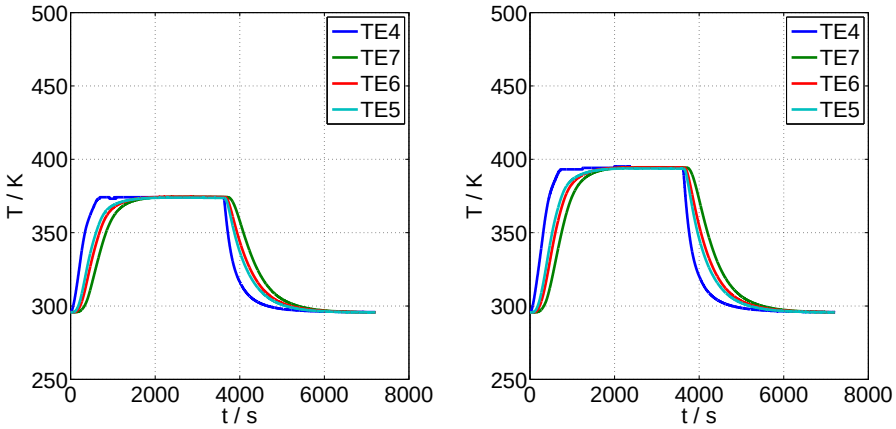

(a) 373.15 K

(b) 393.15 K

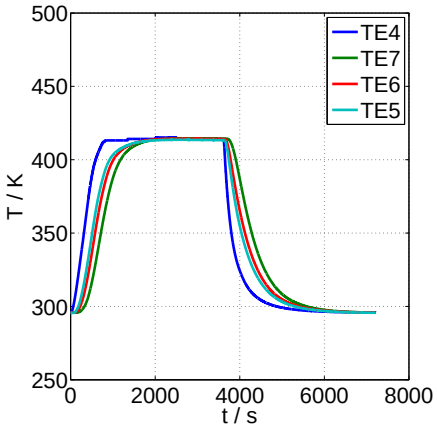

(c) 413.15 K

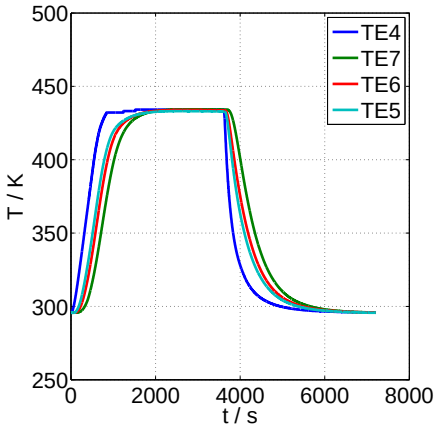

(d) 433.15 K

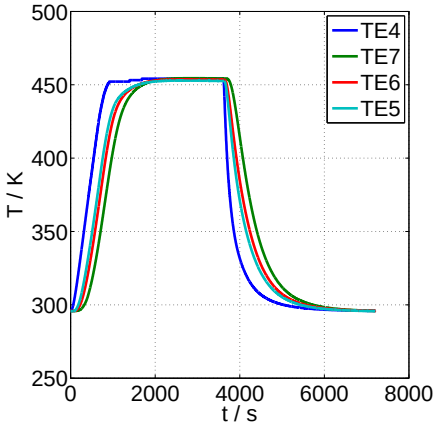

(e) 453.15 K

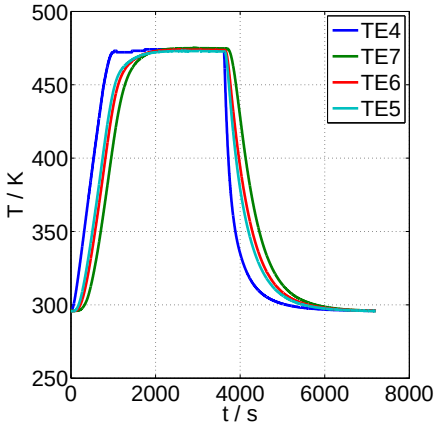

(f) 473.15 K

Figure 4.2: Measured temperature profiles for the experiments of heat transfer without convection and with constant wall temperature.

dominant heat transfer mechanism is heat conduction. From the temperature profiles it is clear that the adsorbent shows a low thermal conductivity.

The low thermal conductivity of the bed can be explained by the morphology of a packed bed. In a packed bed there are void spaces between the solid particles. These void spaces are filled with gas. Gases have a low thermal conductivity since the molecules have a higher degree of freedom compared to solids. Therefore, the transfer of heat due to vibrations is lower than in solids, which is the reason for their low thermal conductivity. The gas in the voids of the bed will therefore transfer the heat slowly. In addition, the solid particles are porous, meaning they are also filled with the gas. Therefore, they will have a lower thermal conductivity compared to non-porous particles of the same material. These two reasons lead to the low thermal conductivity of an adsorbent packed bed.

As mentioned in section 2.2.3 the ZBS-model is the most common and adequate one to describe the effective heat conductivity of a packed bed in a homogeneous model. Since the heat conductivity of the adsorbent particle λ_p is not known accurately, one needs to determine this parameter. Also, since the homogeneous α_w-model is used for the numerical model it is advisable to determine the non-convective Nusselt number $\mathrm{Nu}_{0,\mathrm{w}}$ in order to compare it with correlations in the literature. The reason is that the correlations in literature for the non-convective Nusselt number were not derived using an adsorbent bed. If the correlation of Nilles is observed (see equation (2.26)) a linear dependency of the non-convective Nusselt number to the effective heat conductivity of the bed can be noticed. Since the effective heat conductivity of the bed depends on λ_p one can deduce that $\mathrm{Nu}_{0,\mathrm{w}}$ will also depend on λ_p. Therefore, it is advisable to use the same structure as Nilles for describing $\mathrm{Nu}_{0,\mathrm{w}}$ [58]:

$$\mathrm{Nu}_{0,\mathrm{w}} = \mathrm{Bi}\frac{\lambda_\mathrm{bed}}{\lambda_\mathrm{g}} \tag{4.1}$$

This implies that the Biot number Bi is the actual model parameter that needs to be determined.

4.1.1.1 Estimation of the model parameters

To estimate the model parameters, the LiveLink is used. The PDEs are solved using COMSOL and the results are passed to Matlab where the minimization of the least square error is conducted. The minimization is in this case more demanding, since the problem to be solved is not linear. This is illustrated in Figure 4.3, where the least square error for some combinations of the parameters for the first experiment are plotted as a contour plot. The non-linearity of the problem can be observed since different slopes are obtained depending on the position in the plot. Nevertheless, the parameters can be estimated using optimization routines for nonlinear optimization. The estimated parameters are illustrated in Figure 4.4.

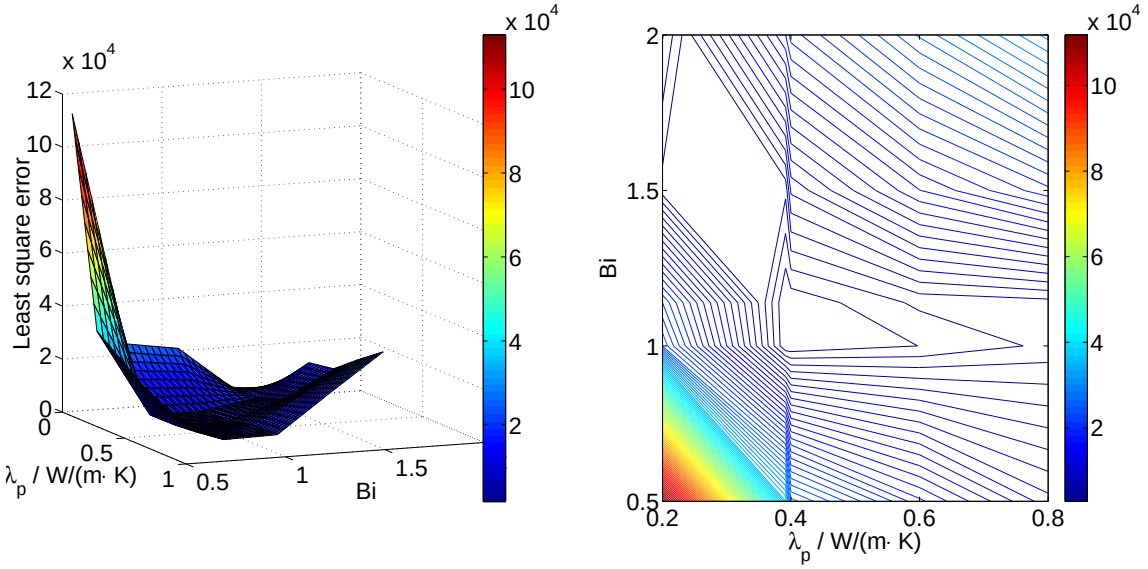

(a) Surface plot (b) Contour plot

Figure 4.3: Contour and surface plot of the least square error for the first experiment.

A small variation of the heat conductivity of the adsorbent particle λ_p can be observed. For the experiments that are conducted twice, the estimated parameter is not exactly the same. This is also expected since the problem is highly nonlinear. Another reason for this is that a small change in λ_p will not have a huge impact on the effective heat conductivity of the bed λ_{bed} which is the actual model parameter. This can be clearly observed in Figure 4.4 where λ_{bed} is plotted against the different experiments. The effective heat conductivity is calculated using the ZBS-model and a heat conductivity of the gas at the mean temperature. The discrepancy can be explained by the increase in the heat conductivity of the gas. Since the mean temperature increases for the different experiments the heat conductivity of the gas is also increased. This increase leads to a slight increase of the effective heat conductivity as can be observed in Figure 4.4. Since the values that were obtained for λ_p are not significantly different and small changes of this value do not change significantly λ_{bed}, one can assume an average value is the most adequate value for λ_p.

The estimated Biot number Bi also varies between the different experiments and when λ_p increases, Bi decreases and when λ_p increases, Bi decreases. This indicates, that both parameters are correlated, which can be expected since Bi is multiplied with λ_{bed} in order to obtain $Nu_{0,w}$ in the model. Nevertheless, similar to λ_p the discrepancy between the different Bi values is not significant, which permits the assumption that the average value is the most adequate value. The obtained values from the parameter estimation are listed in Table 4.2.

Figure 4.5 shows the obtained temperature profiles for each experiment and the measured

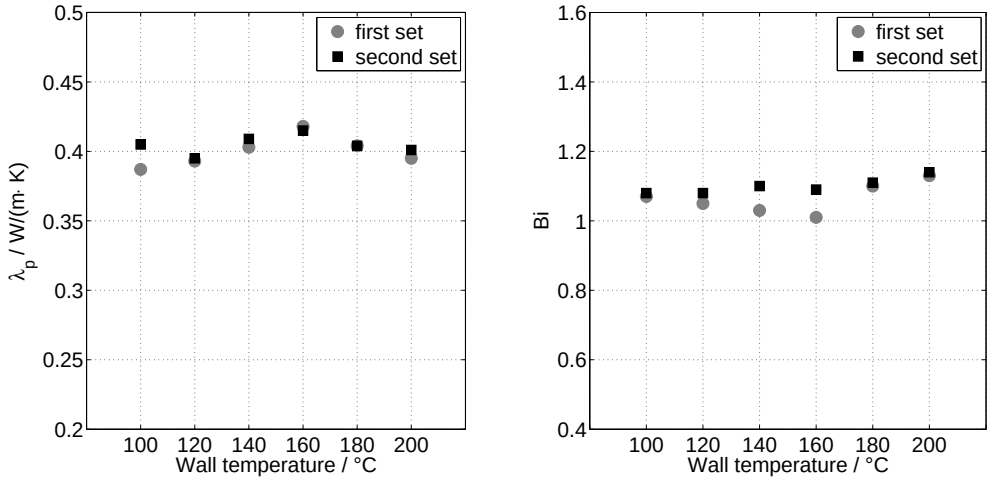

(a) λ_p (b) Bi

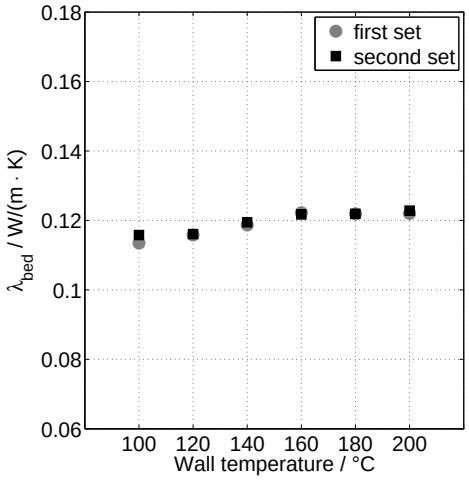

(c) λ_{bed}

Figure 4.4: Estimated values for λ_p, λ_{bed} and Bi for the different experiments with constant wall temperature.

profiles of the first set of experiments. The results of the second set are comparable to those of the first set. One can clearly see the agreement between the experiments and simulations. Figure 4.6 shows the parity plot for the experiment of the first set with a wall temperature of 473.15 K. The agreement between simulation and experiment

Table 4.2: Average estimated parameters for the experiments with constant wall temperature.

Parameter	Estimated value
λ_p	0.402 $^{W}/_{m\cdot K}$
λ_{bed}	0.12 $^{W}/_{m\cdot K}$
Bi	1.08

can again be observed. The parity plots for the different experiments are similar to Figure 4.6, which again indicates the agreement between the model and the experimental measurements.

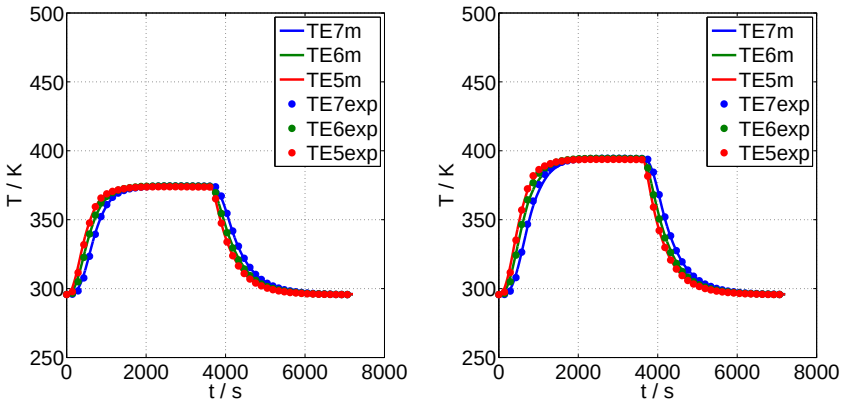

(a) 373.15 K

(b) 393.15 K

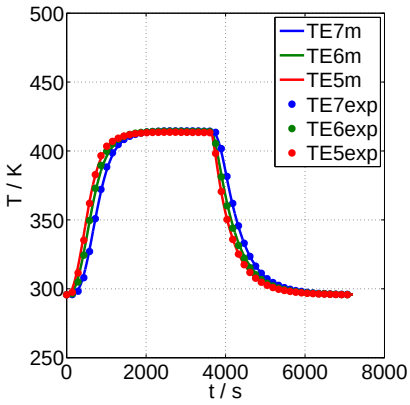

(c) 413.15 K

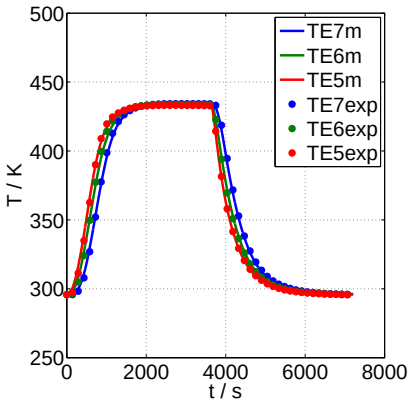

(d) 433.15 K

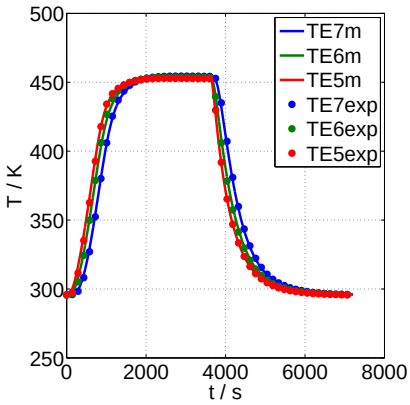

(e) 453.15 K

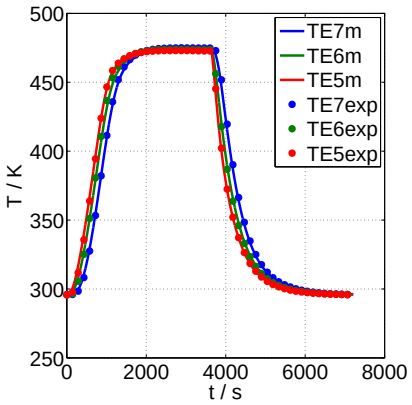

(f) 473.15 K

Figure 4.5: Measured and obtained temperature profiles for the first set of experiments of heat transfer without convection and constant wall temperature. The letters after the name of the thermocouple mean: m for model and exp for measured temperature.

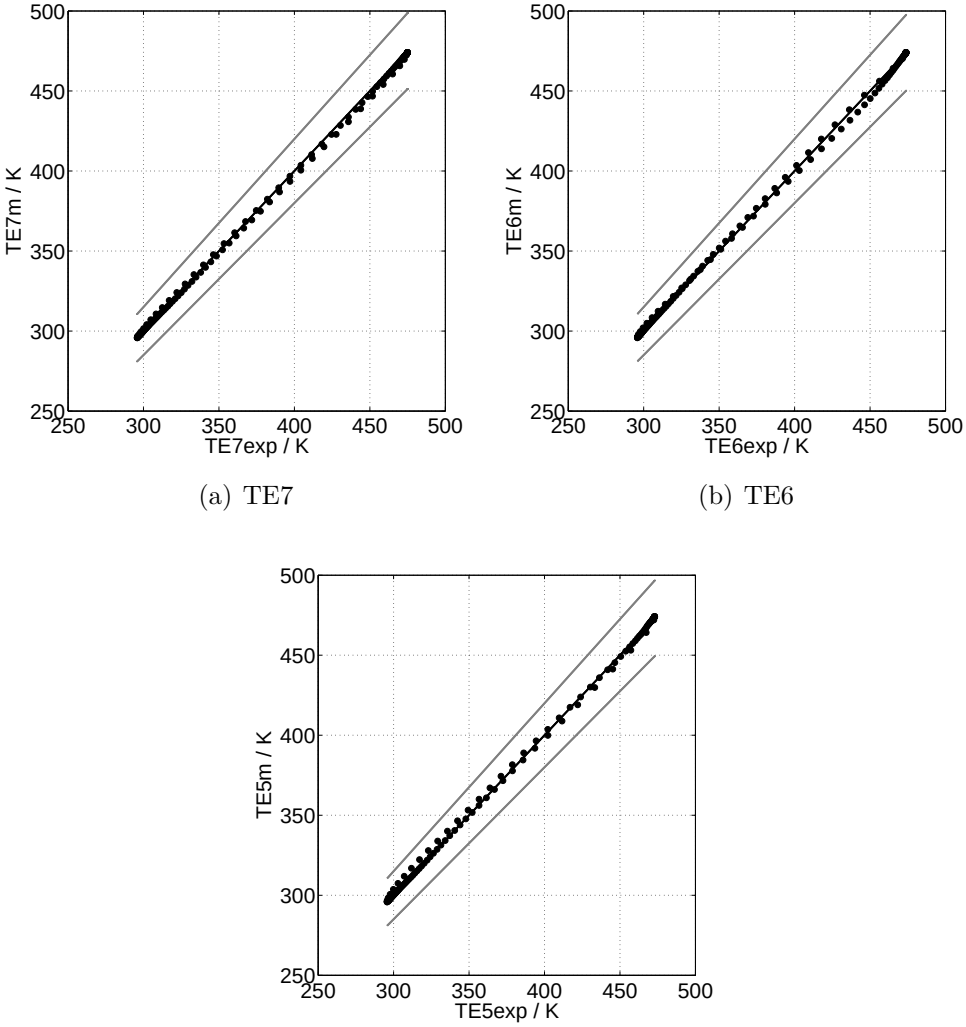

(a) TE7

(b) TE6

(c) TE5

Figure 4.6: Parity plot for experiment with constant wall temperature of 473.15 K. The gray lines represent a ± 5% deviation.

4.1.2 Constant heat duty

The procedure according to section 3.2.4.1 is used for the experiments with constant heat duty. Five different heat duties are chosen. Similar to the experiments with constant wall temperature, the experiments are conducted twice. The different heat duties that are used are shown in Table 4.3; the temperature profiles for the different experiments of the first run are demonstrated in Figure 4.7.

Contrary to the experiments with constant wall temperature, the wall temperature rises slowly and almost linearly with time. This is also expected since in this case, a boundary condition of the second kind is used. Therefore, the temperature increase will be slower since the wall must be heated at a constant heat duty. Since the wall temperature increases over the entire time, it is clear that an equilibrium between the heat losses and

the heat duty is not reached during the given time. The measured temperatures inside of the bed will follow the wall temperature time-delayed and increase almost linearly

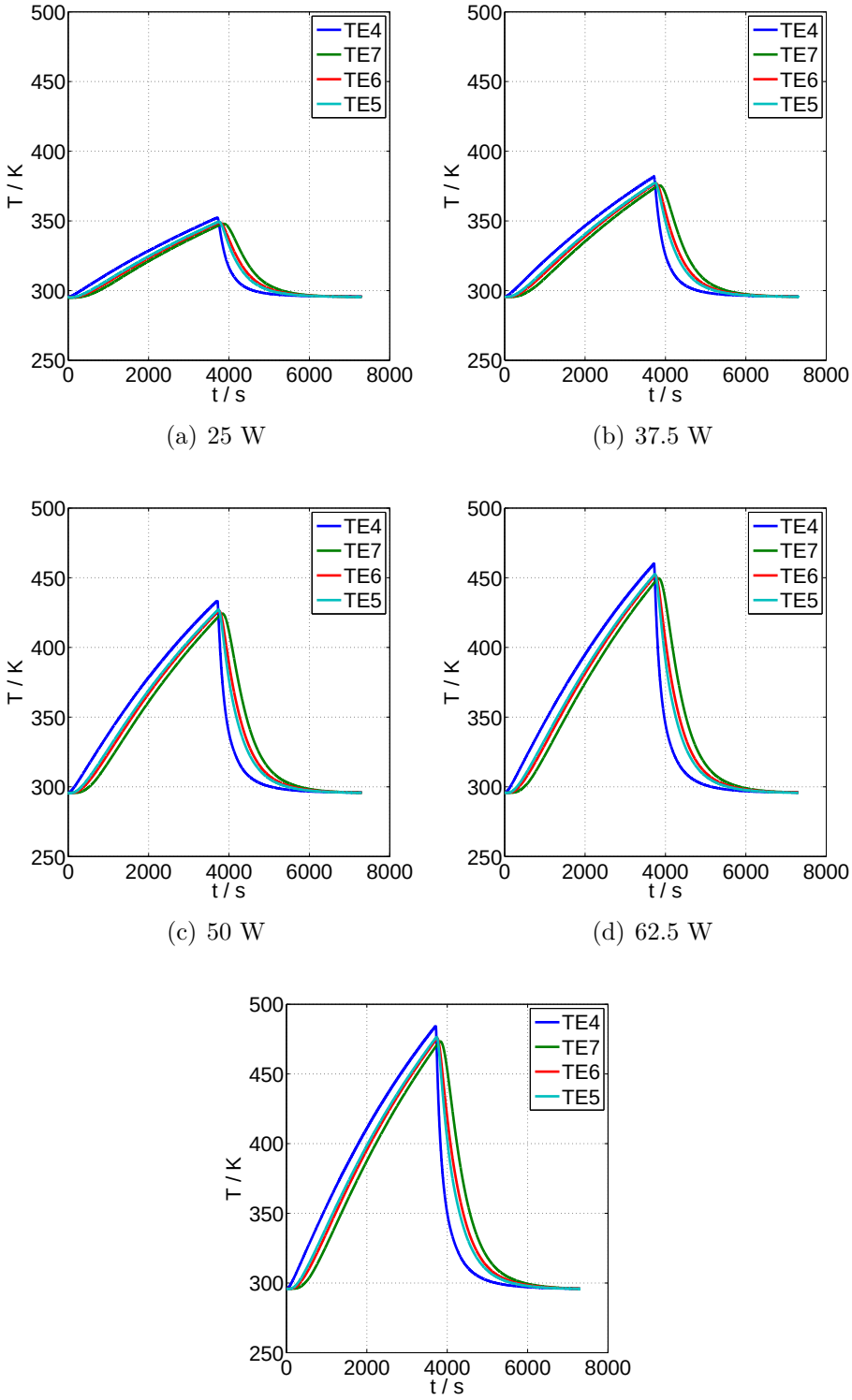

(a) 25 W (b) 37.5 W

(c) 50 W (d) 62.5 W

(e) 75 W

Figure 4.7: Measured temperature profiles for the experiments of heat transfer without convection and with constant heat duty.

Table 4.3: Duties used for the experiments with constant heat duty. Each experiment is conducted twice.

Experiment	Heat duty in W
7	25
8	37.5
9	50
10	62.5
11	75

with time. The higher the distance to the wall, the longer the time-delay. This is clear since TE7 is the thermocouple with the highest time-delay. Similar to the experiments with constant wall temperature, no convection is present, therefore heat conduction is the dominant heat transfer mechanism. Because of the high time-delays it is again clear, that the bed has a low thermal conductivity.

For the parameter estimation the ZBS-model is used again. Similar to the experiments with a constant wall temperature, the heat conductivity of the solid particle λ_p and the Bi number are estimated for the experiments with constant heat duty. The obtained results can be compared with the previous results in order to determine whether there is a dependency of the boundary condition.

4.1.2.1 Estimation of the model parameters

The LiveLink is used in order to estimate the parameters. As in the previous case, the problem to be solved is highly nonlinear and similar contour plots to those in Figure 4.3 are obtained. The obtained parameters are illustrated in Figure 4.8.

The results for the heat conductivity of the adsorbent particle λ_p show a small variation again. As in the previous case, a deviation between the experiments that are conducted twice can be observed. The reason for this, as mentioned before, is the non-linearity of the optimization problem. The small influence of a change in λ_p on λ_{bed}, which is also a reason for the small variation of the results, can be observed in Figure 4.8. The effective heat conductivity is calculted using the ZBS-model and a heat conductivity of the gas at the mean temperature between the maximal and minimal temperature. The slight increase of the effective heat conductivity, as mentioned in the previous section, can be explained by the increase of the heat conductivity of the gas caused by the increase of heat duty. The average value of λ_p is again assumed as the most adequate one.

The correlation between the Bi number and λ_p can also be observed, which as mentioned earlier is also expected. The variation between the estimated parameters is not significant which allows to assume that the most adequate value is the average one. The obtained average values from the parameter estimation are tabulated in Table 4.4.

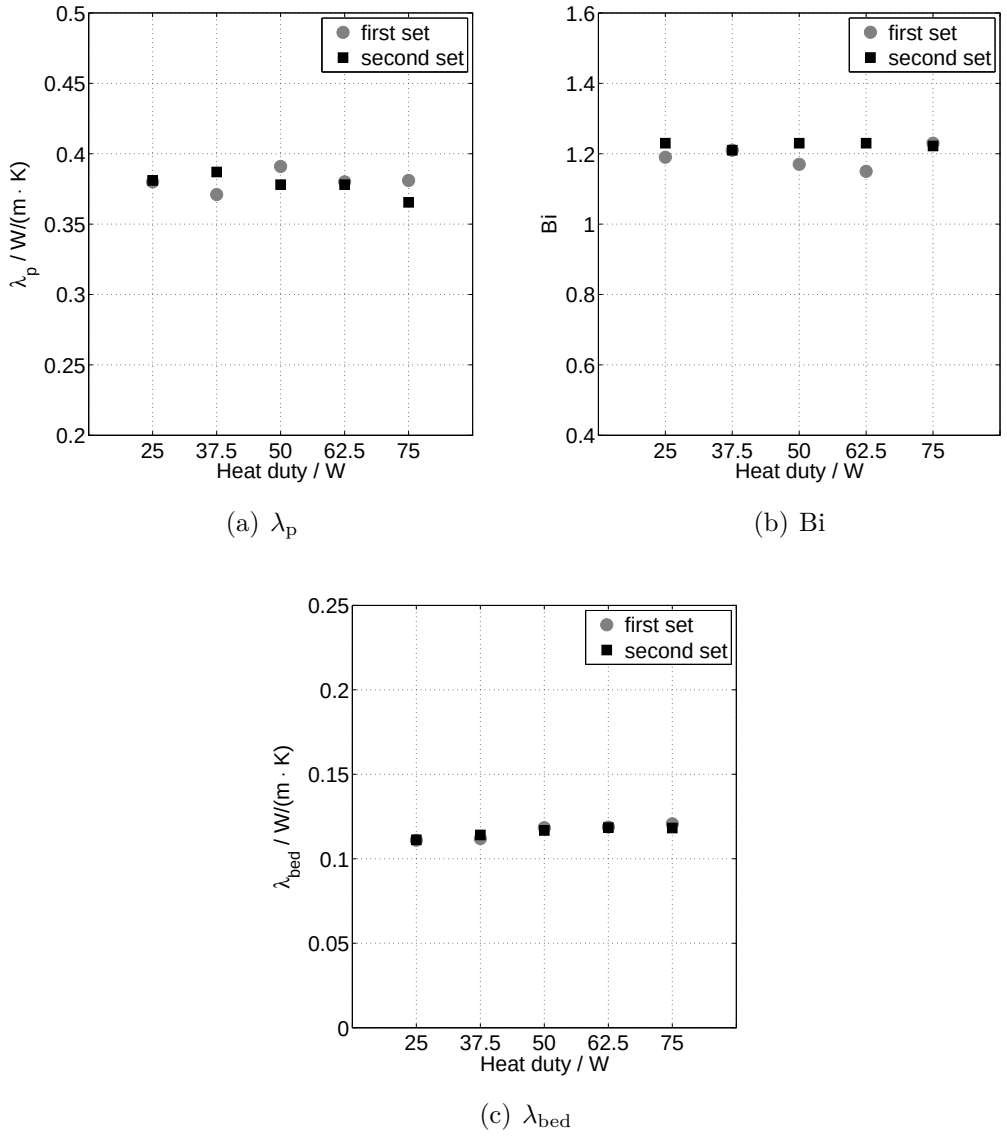

(a) λ_{p}

(b) Bi

(c) λ_{bed}

Figure 4.8: Estimated values for λ_p, λ_{bed}, and Bi for the different experiments with constant heat duty.

Figure 4.9 shows the obtained temperature profiles for each experiment and the measured profiles of the first set of experiments. The results of the second set are comparable to those of the first set. The agreement between the experiments and simulations is

Table 4.4: Average estimated parameters for the experiments with constant heat duty.

Parameter	Estimated value
λ_{p}	0.379 $^{\mathrm{W}}/_{\mathrm{m\cdot K}}$
λ_{bed}	0.12 $^{\mathrm{W}}/_{\mathrm{m\cdot K}}$
Bi	1.21

clear. The parity plots in Figure 4.10 for 75 W confirm the good agreement between simulation and experiment.

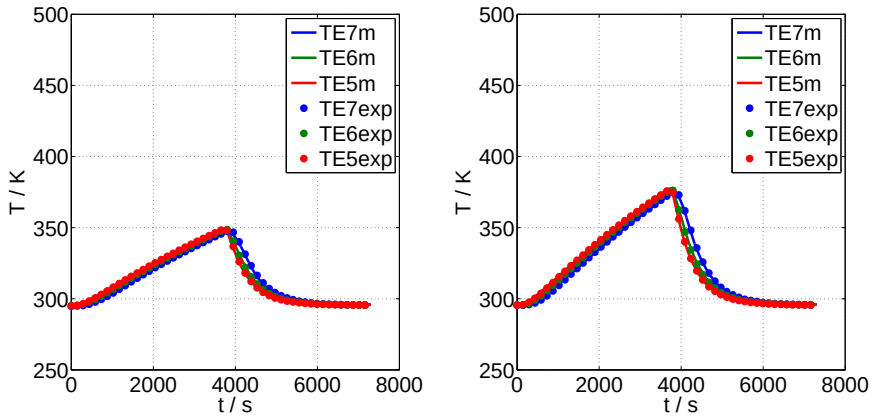

(a) 25 W (b) 37.5 W

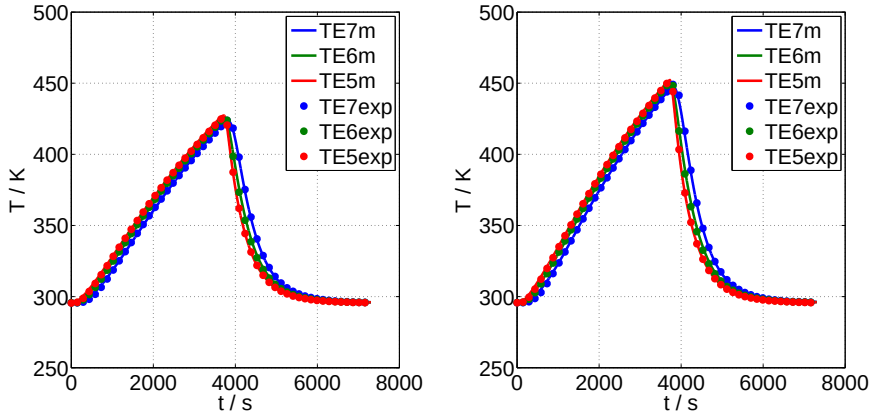

(c) 50 W (d) 62.5 W

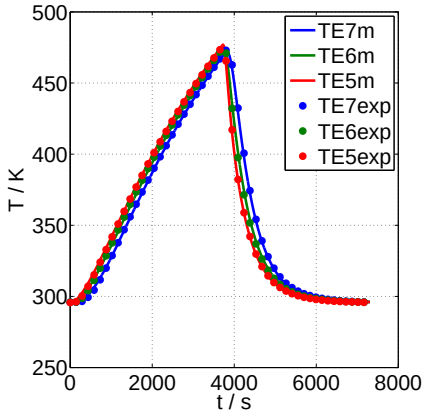

(e) 75 W

Figure 4.9: Measured and obtained temperature profiles for the first set of experiments of heat transfer without convection and constant heat duty. The letters after the name of the thermocouple mean: m for model and exp for measured temperature.

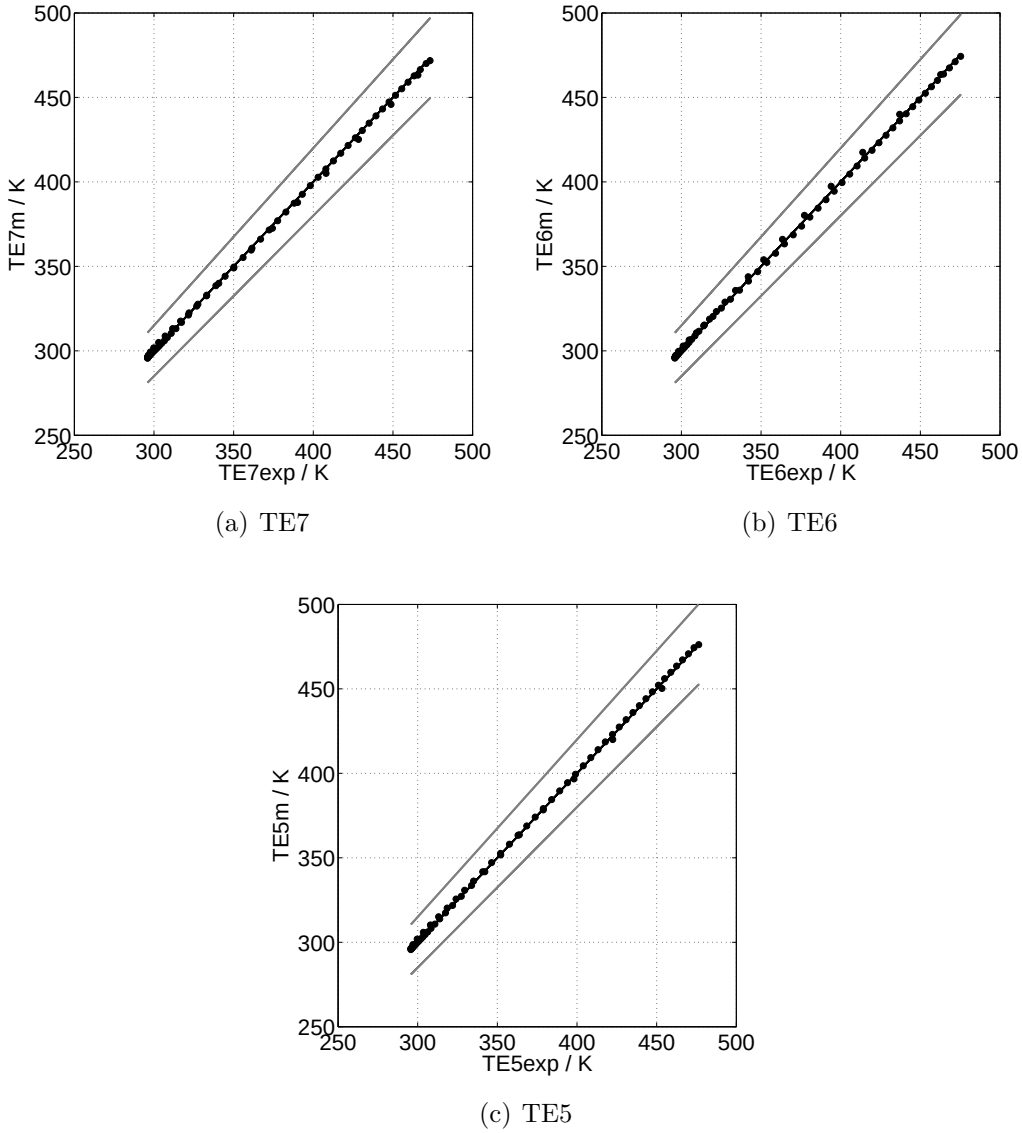

(a) TE7

(b) TE6

(c) TE5

Figure 4.10: Parity plot for experiment with constant heat duty of 75 W. The gray lines represent a ± 5% deviation.

4.1.3 Comparison of the different boundary conditions

A deviation between the average obtained parameters can be observed when comparing Table 4.2 and Table 4.4. Nevertheless, this deviation is not significant. This indicates, that the parameters are not boundary dependent. As mentioned earlier, the parameters are correlated which explains why the Bi number is higher in the constant heat duty case as for the constant wall temperature case, since λ_p is lower. Nevertheless, one can see that the average value of λ_{bed} is equal in both cases. This indicates that the model is more sensitive to a change in λ_{bed} than to a change in the Biot number. In addition, the deviation between both values from the average value is not high. Therefore, it is acceptable to assume that the Biot number and the heat conductivity of the particle are boundary independent and that the most accurate value is an average between

Table 4.5: Average estimated parameters for the non-convective heat transfer experiments and the obtained $Nu_{0,w}$ value and $Nu_{0,w}$ values obtained using the correlations of [58] and [77].

Parameter	Estimated value
λ_p	0.39 $^{W}/_{m\cdot K}$
λ_{bed}	0.12 $^{W}/_{m\cdot K}$
Bi	1.14
$Nu_{0,w,this\ work}$	4.33
$Nu_{0,w,Nilles}$	6.25
$Nu_{0,w,Eurokin}$	3.86

both cases. The average values that were used for the following investigations are displayed in Table 4.5 and the values obtained by using the correlation of Nilles [58] and Eurokin [77] for the non-convective Nusselt number $Nu_{0,w}$. The heat conduction of the gas is calculated using the average temperature of the highest and lowest temperature of the experiments.

Table 4.5 shows, that the value obtained by the correlation of Nilles [58] is much higher than the value obtained from the experiments. On the other hand, the value obtained using the correlation of Eurokin is similar to the value obtained from the experiments. Nevertheless, as mentioned earlier the model seems to be more sensitive towards the effective heat conductivity of the bed, which indicates that it is difficult to estimate the wall Nusselt number with high accuracy. This was also observed by Nilles [58] which indicates that the obtained Nusselt number had a high uncertainty. Nonetheless, the obtained non-convective Nusselt number in this work did not deviate significantly, which indicates that the obtained value can be used for the following investigations. Furthermore, the obtained value is similar to the value obtained using the correlation of Eurokin [77], which indicates its plausibility.

4.2 Heat transfer in packed beds at low Péclet numbers

In order to achieve different Péclet numbers, the velocity is changed as well as the pressure because high velocities would move the homogeneous measuring range (see Figure 3.5) in the flow direction, meaning that inlet effects would be measured. Therefore, the pressure is used to vary the Péclet number. The idea of the indirectly heated and cooled TSA process is to use small streams or no stream at all during the regeneration. In addition, during the adsorption step of CO_2 from a flue gas emitted from a coal fired power plant using the proposed indirectly heated and cooled TSA process, the Péclet number will not be high ($30<Pe<50$) because of the low pressure and pressure drop limitations. The correlations for the convective contribution found in the literature

were derived by investigating higher Péclet numbers (Pe>50). It is therefore necessary to investigate the convective contribution to the effective radial heat conductivity and to the wall Nusselt number for small Péclet number in order to accurately describe the heat transfer characteristics during this process.

The parameters in the previous section showed no significant influence on the boundary condition. Therefore, only a constant heat duty was used for the experiments with convective heat transfer. Since the reproducibility of the experiments in the previous section was satisfactory only one set of experiments was conducted. The conducted experiments are listed in Table 4.6. Experiments 12 to 15 have similar conditions, meaning they have similar Péclet numbers. The same is valid for experiments 16 to 19 and experiments 20 to 22. Therefore, the experiments can be categorized into three different Péclet numbers.

The experimental measurements for the first Péclet number are illustrated in Figure 4.11. Similar to the experiments with constant heat duty and no convection, the wall temperature increases during the heating almost linearly with time and the different thermocouples follow with a time delay. If Figure 4.11 is compared with Figure 4.7, almost no difference is noted. This indicates that under the given conditions the influence of convection on the heat transfer is not significant. In this case, the non-convective heat transfer is the dominating mechanism and not the heat transfer due to a cross mixing caused by convection. This can also be expected since the Reynolds number is low (Re<10) and therefore no significant mixing of the fluid will occur. Therefore, the convective contribution to the radial heat transfer is negligible.

Table 4.6: Experiments conducted for the investigation of convective heat transfer in packed beds at low Péclet numbers.

Experiment	Heat duty in W	Pressure in bar	Superficial velocity in cm/s	Average particle Reynolds number
12	37.5	5	1	7.4
13	50	5	1	7.4
14	62.5	5	1	7.4
15	75	5	1	7.4
16	37.5	5	3	18.7
17	50	5	3	18.7
18	62.5	5	3	18.7
19	75	5	3	18.7
20	50	7.5	3	27.6
21	62.5	7.5	3	27.6
22	75	7.5	3	27.6

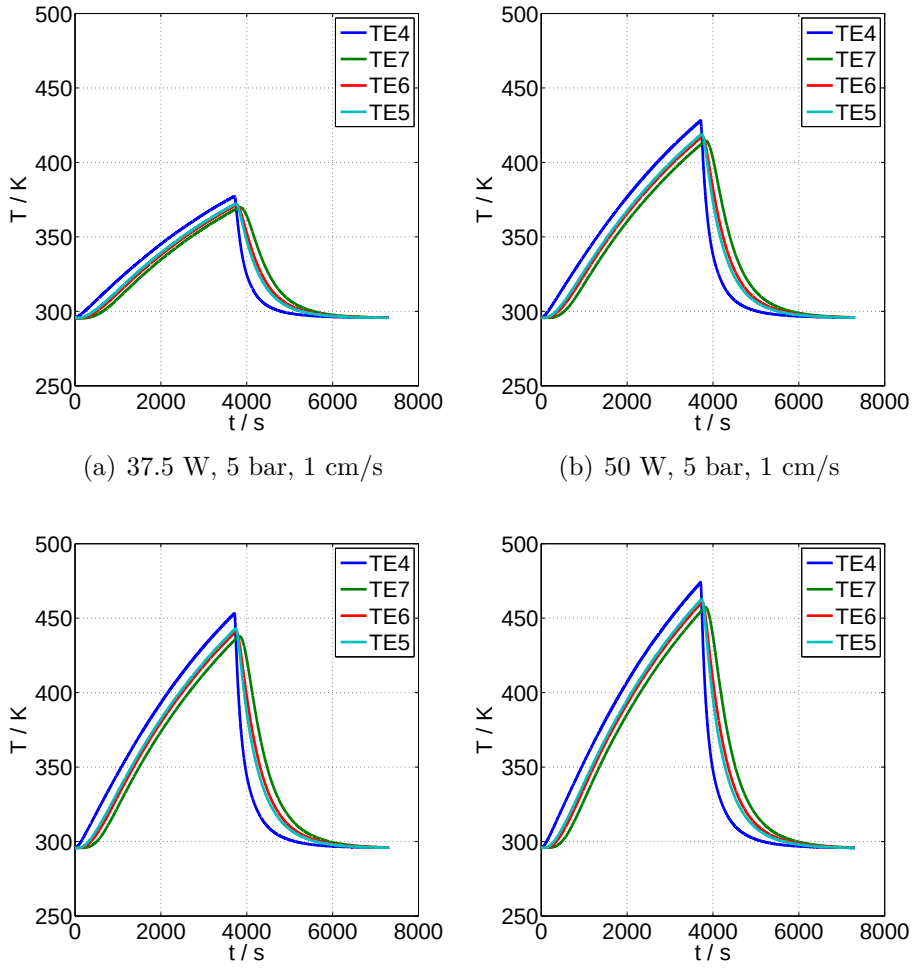

(a) 37.5 W, 5 bar, 1 cm/s

(b) 50 W, 5 bar, 1 cm/s

(c) 62.5 W, 5 bar, 1 cm/s

(d) 75 W, 5 bar, 1 cm/s

Figure 4.11: Measured temperature profiles for the first Péclet number and for the different heat duties.

Figure 4.12 illustrates the measured temperature profiles for the second Péclet number. In this case a clear influence was observed. The wall temperature increases linearly at the beginning, but close to the end of the heating step, a change in the slope was observed. A similar trend is observed for the temperature inside the bed. The temperatures are further apart than in the case of the first Péclet number and the profiles are not linear. This can be explained by the fact that in this case, the convective contribution has an influence on the heat transport. Since the boundaries of the system are open and since the velocity is three times higher than in the previous case, the convective transport is also increased significantly. This leads to a higher energy output of the system. Since the Péclet number is still not high (Pe<20), meaning that the radial heat transfer is still dominated by the non-convective mechanism, the radial heat transfer is still slow compared to the convective output. Therefore, the time delay of the temperature profiles is increased, especially in the middle of the bed. For the cooling step on the other hand, one can clearly see that the temperature profiles get closer. This again can be explained by the increase in energy output, since in this case the fluid can transport

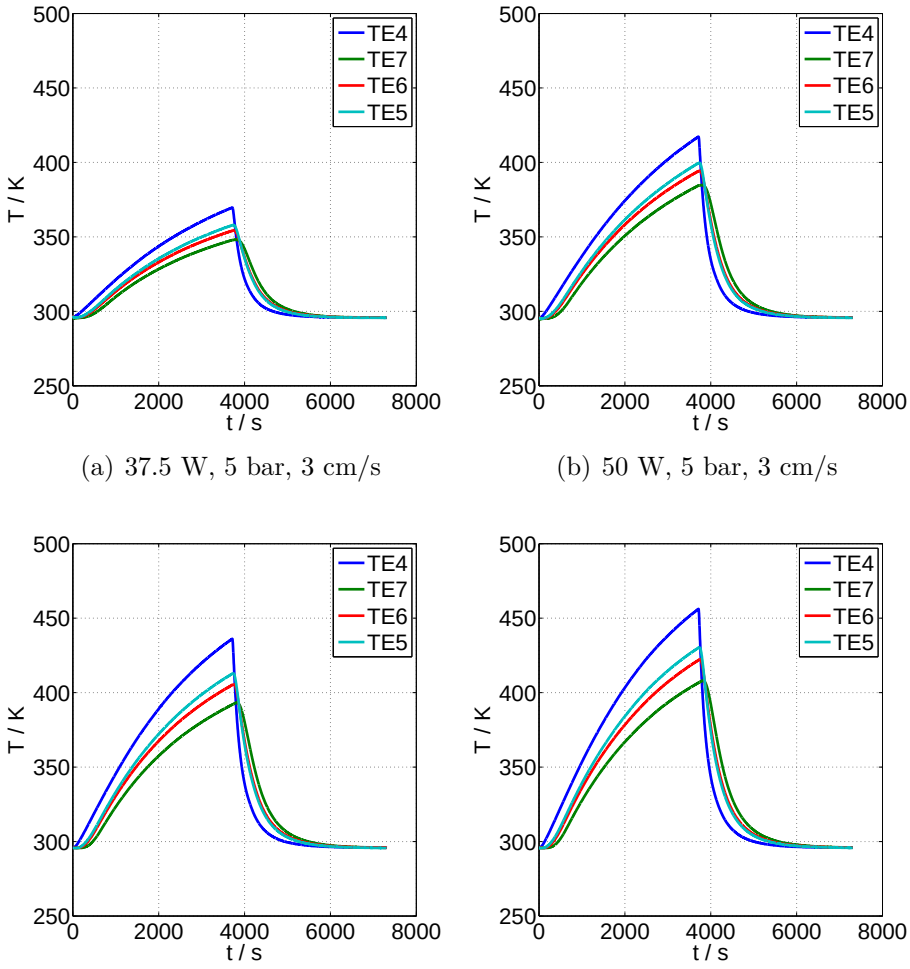

(a) 37.5 W, 5 bar, 3 cm/s

(b) 50 W, 5 bar, 3 cm/s

(c) 62.5 W, 5 bar, 3 cm/s

(d) 75 W, 5 bar, 3 cm/s

Figure 4.12: Measured temperature profiles for the second Péclet number and for the different heat duties

more heat out of the system. Therefore, the bed is also cooled directly with the gas.

In Figure 4.13 the temperature profiles for the third Péclet number can be observed. In this case, the pressure is increased which increases the density of the fluid and therefore the convective transport. Similar to the previous case, the Péclet number is low (Pe≈ 20) in this case and the convective transport is increased which increases the time delay during the heating step. For the cooling step it is clear that the temperature profiles get closer because of the increase in the convective transport.

The experiments show, especially for the heating step, that a tradeoff between radial heat transport and convective transport exists. This is also expected since, if the axial convective heat transport is increased and the radial heat transport is not increased significantly, the heat will not be transported radially fast enough. For short tubes such as the tube that is used in this work, this influence is noticeable. Nevertheless, it is expected that for long tubes, this influence will only be noticed in a short segment

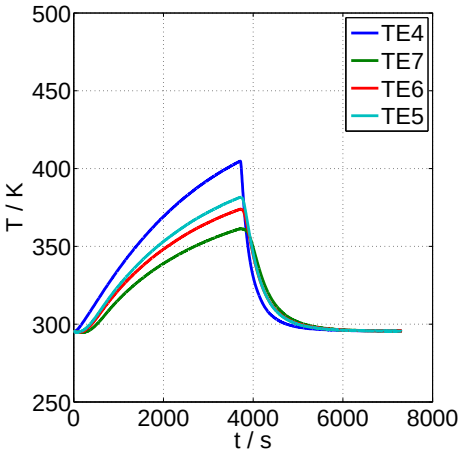

(a) 50 W, 7.5 bar, 3 cm/s

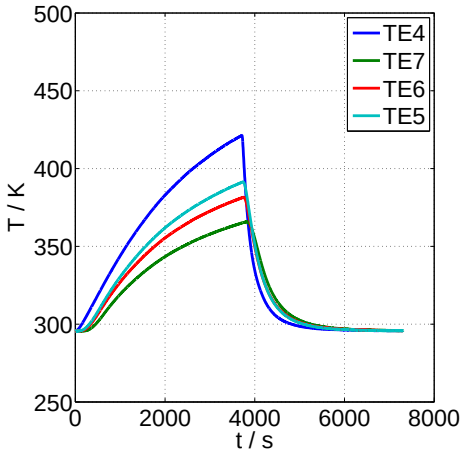

(b) 62.5 W, 7.5 bar, 3 cm/s

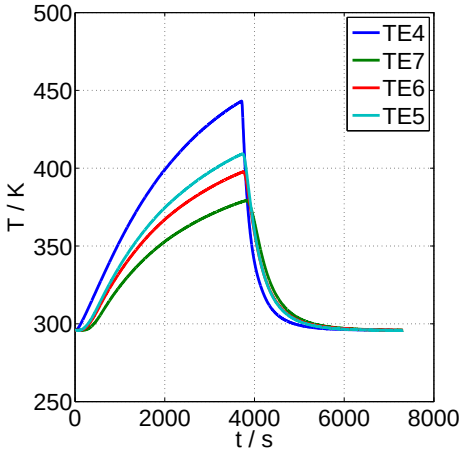

(c) 75 W, 7.5 bar, 3 cm/s

Figure 4.13: Measured temperature profiles for the third Péclet number and for the different heat duties

at the inlet of the tube. To reduce this influence, either the inner diameter of the tube must be reduced in order to increase the radial transport or the residence time of the fluid must be increased, meaning longer tubes. For the cooling step on the other hand, an increase in tube length will reduce the positive contribution of the fluid to the cooling process, since this contribution will again only be noticeable in a short segment at the inlet.

4.2.1 Estimation of the model parameters

Since the model used in Comsol also considers convection a parameter estimation can be conducted. The parameters that are estimated using the LiveLink are the dimensionless convective contribution to the radial heat conductivity $A_{\text{heat conductivity}}$

and the convective contribution to the Nusselt number $\mathrm{Nu}_{\mathrm{convective}}$. The effective radial heat conductivity is written as;

$$\frac{\lambda_{\mathrm{eff,Rad}}}{\lambda_{\mathrm{g}}} = \frac{\lambda_{\mathrm{bed}}}{\lambda_{\mathrm{g}}} + \mathrm{A}_{\mathrm{heat\ conductivity}} \tag{4.2}$$

in the model and the wall Nusselt number is written as:

$$\mathrm{Nu}_{\mathrm{w}} = \mathrm{Bi} \cdot \frac{\lambda_{\mathrm{bed}}}{\lambda_{\mathrm{g}}} + \mathrm{Nu}_{\mathrm{convective}} \tag{4.3}$$

For λ_{p} and Bi the estimated values in the previous section are used (see Table 4.5).

The model optimization problem is again highly nonlinear as shown in the contour plot in Figure 4.14. Therefore, nonlinear optimization routines are used.

The estimated parameters can be observed in Figure 4.15. It is clear that there are three groups of values for $\mathrm{A}_{\mathrm{heat\ conductivity}}$. Each group of values represents a different Péclet number. This is also expected since convection will cause a cross mixing of the fluid inside the bed and therefore increase the radial heat transfer. The higher the cross mixing, meaning the higher the Péclet number, the higher the increase of the radial heat transfer. If each group of values is observed individually, the values show some deviation, especially the last group. For the first and second group, the deviation between the results is not high, but for the third group the first value is significantly lower than the others. If the convective Nusselt contribution $\mathrm{Nu}_{\mathrm{convective}}$ for that experiment is observed, it is clear that this value is higher than the others. This indicates that both parameters are correlated. Therefore, the optimization routine tried

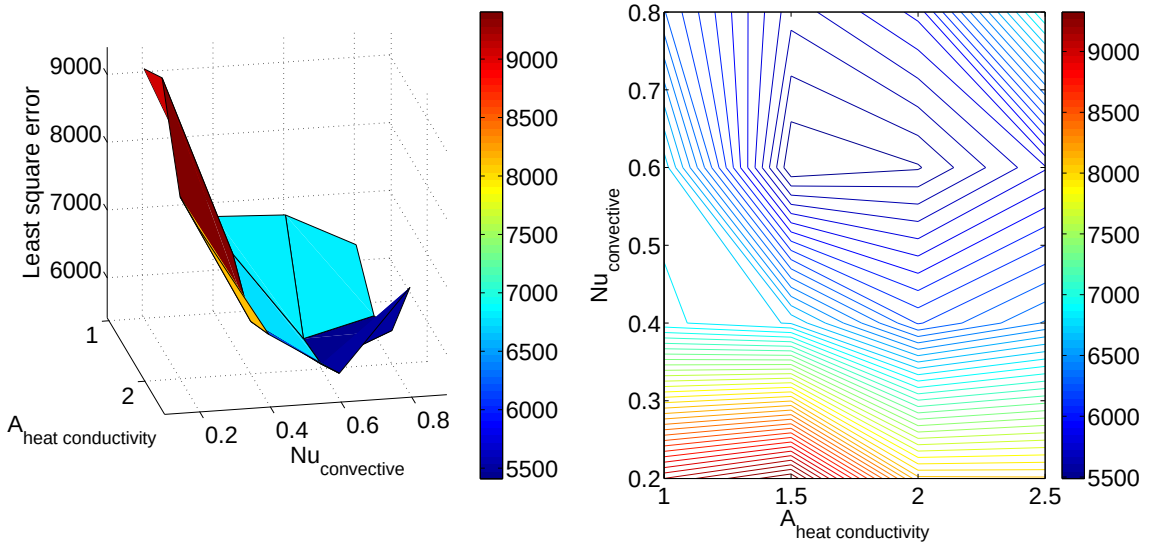

(a) Surface plot (b) Contour plot

Figure 4.14: Contour and surface plot of the least square error for the first experiment.

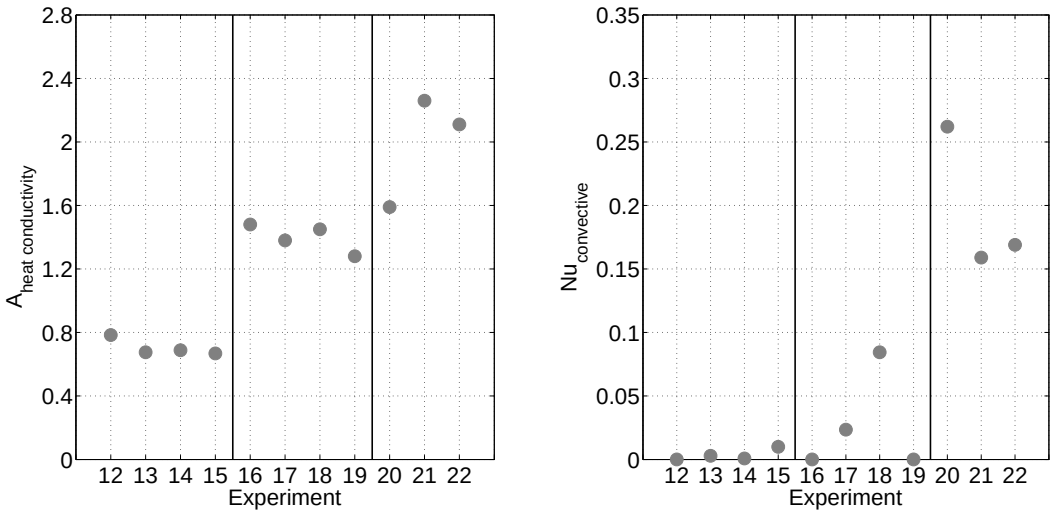

(a) $A_{\text{heat conductivity}}$ (b) $Nu_{\text{convective}}$

Figure 4.15: Estimated parameters for the experiments with convective heat transfer.

to compensate the lower convective contribution to the heat conductivity by increasing $Nu_{\text{convective}}$. Since the other values do not show a very high deviation one can assume that this value is not estimated accurately.

In order to investigate the relationship between the Péclet number and $A_{\text{heat conductivity}}$ the obtained results are plotted against the respective Péclet number as illustrated in Figure 4.16. The three different groups of values are shown. If the value that deviates

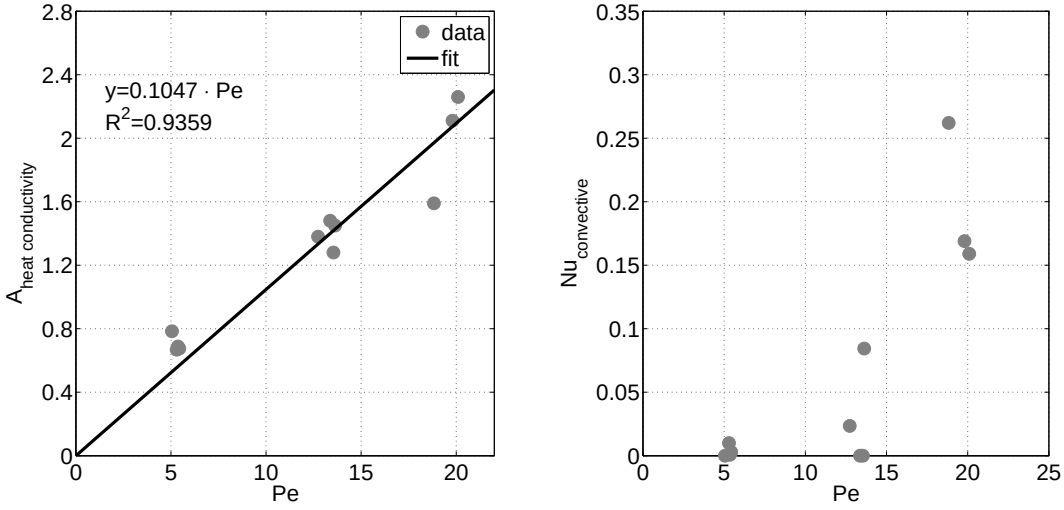

(a) $A_{\text{heat conductivity}}$ (b) $Nu_{\text{convective}}$

Figure 4.16: Estimated values of $A_{\text{heat conductivity}}$ and $Nu_{\text{convective}}$ plotted against the Péclet number.

significantly from the other values in the third group is neglected, one can assume there is a linear relationship between $A_{\text{heat conductivity}}$ and the Péclet number. As mentioned in section 2.2.4, the radial heat conductivity in packed beds depends linearly on the Péclet number for high Péclet numbers. From the slope of the linear regression curve, one can calculate the value of K_{Rad} (see equation 2.39):

$$K_{\text{Rad,exp}} = \frac{1}{0.1047} = 9.55 \tag{4.4}$$

Comparing this value with the value obtained using equation (2.40), which was derived using higher Péclet numbers (Pe>50):

$$K_{\text{Rad,lit}} = 8.79 \tag{4.5}$$

both values do not deviate significantly. This indicates, that for low Péclet numbers, a linear correlation between $\lambda_{\text{eff,Rad}}$ and the Péclet number can also be assumed.

The convective contribution to the Nusselt number does not show any significant functional relationship, as shown in Figure 4.15. This can also be observed in Figure 4.16 where $\text{Nu}_{\text{convective}}$ is plotted against the Péclet number. The reason for the unsatisfying estimation can be explained by the fact, that since the model is more sensitive towards the radial heat conductivity, it is difficult to obtain satisfactory results for $\text{Nu}_{\text{convective}}$. This was also observed by Nilles [58] as mentioned in the previous section. If the values for the non-convective contribution are observed in Table 4.5, this value is orders of magnitude higher than the estimated convective contribution. This indicates that the non-convective contribution is the dominating contribution in the model and since the model does not seem to be sensitive towards $\text{Nu}_{\text{convective}}$ it is difficult to accurately estimate the convective contribution for the given Péclet numbers. Figure 4.17 illustrates

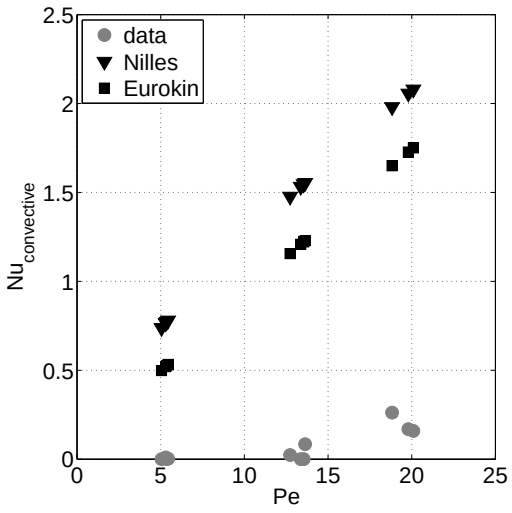

Figure 4.17: Estimated values of $\text{Nu}_{\text{convective}}$ and literature values plotted against the Péclet number.

the estimated values of $\mathrm{Nu}_{\mathrm{convective}}$ and the values obtained using the correlation of Nilles [58]:

$$\mathrm{Nu}_{\mathrm{convective,Nilles}} = 0.19 \cdot \mathrm{Re}^{0.75} \cdot \mathrm{Pr}^{0.33} \tag{4.6}$$

and the correlation of Eurokin [77]:

$$\mathrm{Nu}_{\mathrm{convective,Eurokin}} = 0.0835\mathrm{Re}^{0.91} \left(\frac{\mathrm{Pr}}{\mathrm{Pr}_{\mathrm{air,80°C}}} \right)^{1/3} \tag{4.7}$$

The literature values are significantly higher than the obtained values. As mentioned before, it is difficult to obtain accurate values for the investigated Péclet numbers. Therefore, it is advisable to use the correlation from the literature for the coming adsorption simulations. The model does not seem to be sensitive to this parameter; therefore, a small impact can be deduced if the correlation from literature is used. Moreover, the non-convective contribution will dominate over the range of investigated Péclet numbers. The correlation of Eurokin will be used for the convective contribution in the coming simulations since a similar value to the estimated value for the non-convective contribution is obtained using the Eurokin correlation.

The agreement between the experiments and the simulations for the convective experiments is demonstrated in Figure 4.18, where the results for the different Péclet numbers and for 75 W are plotted. This agreement can also be observed in Figure 4.19 were the parity plots of TE7 for the different Péclet numbers and for 75 W are illustrated. The fact that the numerical results are in agreement with the experimental measurements show the validity and accuracy of the developed model.

The non-convective and the convective experiments allowed the estimation of important radial heat transfer model parameters. These model parameters are mandatory in order

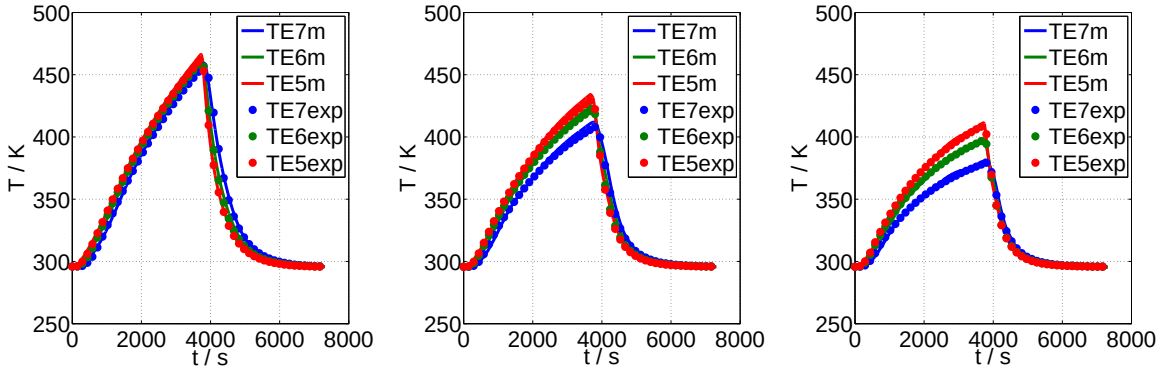

(a) 75 W, 5 bar, 1 cm/s (b) 75 W, 5 bar, 3 cm/s (c) 75 W, 7.5 bar, 3 cm/s

Figure 4.18: Obtained and measured temperature profiles for the convective experiments. Only the results for 75 W and the different Péclet number are plotted

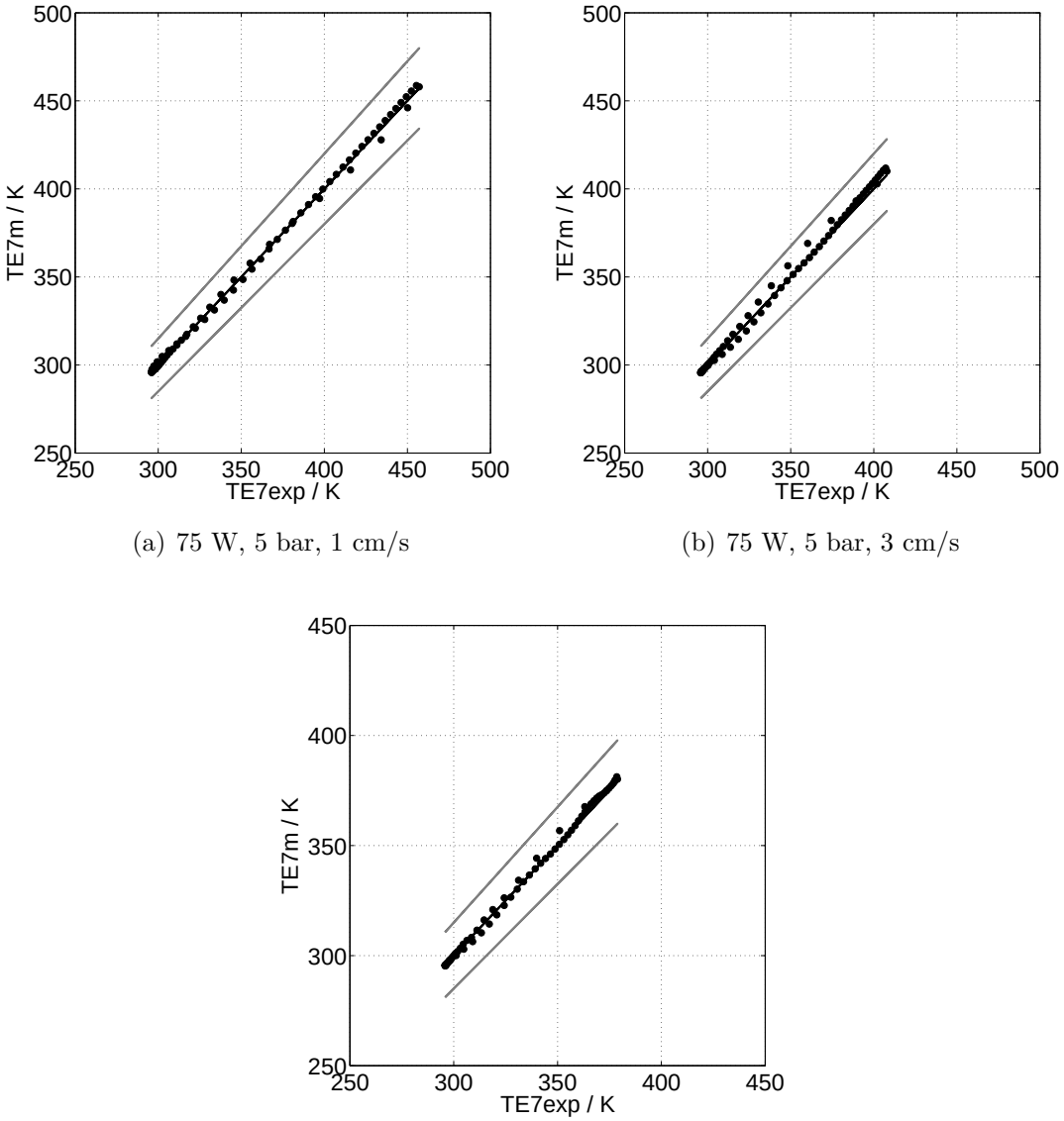

(a) 75 W, 5 bar, 1 cm/s

(b) 75 W, 5 bar, 3 cm/s

(c) 75 W, 7.5 bar, 3 cm/s

Figure 4.19: Parity plot of TE7 for the different Péclet numbers and 75 W. The gray lines represent a ± 5% deviation.

to investigate the adsorption characteristics of the indirect heated TSA process. Therefore, the gained knowledge regarding radial heat transfer was used for the investigation of the adsorption characteristics that is described in the following sections.

4.3 Adsorption isotherm

The adsorption isotherm is required in order to determine the loading of CO_2 on 13X and therefore to simulate the adsorption process. Since the adsorbent bed had to be activated in situ, a breakthrough curve for an experiment of 15% CO_2 in N_2 is measured

in order to determine the experimental loading and compare it to the theoretical loading given by the adsorption isotherm, which is supplied by *Linde Engineering*. The experimental loading is estimated using the following correlation [57, 104]:

$$q^{\mathrm{eq}}_{\mathrm{CO_2,exp}} = \frac{y_{\mathrm{CO_2,in}}}{(1-\epsilon)\rho_{\mathrm{p}}} \left(\frac{\dot{n}_{\mathrm{in}} \tau_{\mathrm{exp}}}{V_{\mathrm{adsorbent}}} - \frac{\epsilon \cdot p}{\mathbb{R} \cdot T} \right) \tag{4.8}$$

$$\tau_{\mathrm{exp}} = \int_0^{t_{\mathrm{final}}} \left(1 - \frac{y_{\mathrm{CO_2,out}}(1 - y_{\mathrm{CO_2,in}})}{y_{\mathrm{CO_2,in}}(1 - y_{\mathrm{CO_2,out}})} \right) dt \tag{4.9}$$

The comparison between the loading obtained by the isotherm and the measured loading shows a deviation of approximately 9%.

$$\frac{q^{\mathrm{eq}}_{\mathrm{CO_2,exp}}}{q^{\mathrm{eq}}_{\mathrm{CO_2,}\mathit{Linde}}} \approx 0.91 \pm 0.03 \tag{4.10}$$

The reason for the deviation is the different procedures for activating the adsorbent, since the temperature that is used for the in situ activation is lower than the temperature that is used for measuring the adsorption isotherm. Higher temperatures than the temperature used for the in situ activation could not be used since 230°C is the maximal allowable temperature in the experimental setup. Therefore, the adsorption isotherm is scaled by the factor in equation 4.10. The scaled isotherm at different temperatures is shown in Figure 4.20. The temperature influence is clear; the higher the temperature, the lower the loading. The scaled isotherm will be used for the numerical simulations in the next section. The scale factor is determined by measuring one point at one temperature, which can be a source of uncertainty when comparing the numerical results with the experimental measurements.

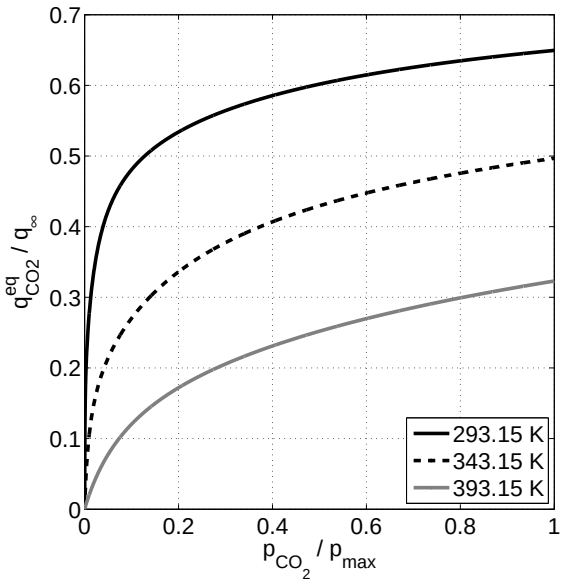

Figure 4.20: Scaled and normalized adsorption isotherm for different temperatures.

4.4 Adsorption characteristics

As mentioned in the previous section the adsorption isotherm is scaled in order to better reproduce the adsorption capacity of the adsorbent in the experimental setup. Therefore, a deviation between the scaled adsorption isotherm and the actual capacity in the experimental setup cannot be excluded. In order to minimize the influence of external factors (e.g. time-delay of TCD) on the comparison between the numerical simulations and the experimental measurements, the time parameter will be normalized. In addition, the first of the multiple cycles was used since the regeneration of the bed before the first cycle starts is equal for all experiments. This allows a comparison between the profiles at the same time scale and under equal conditions, which leads to a better comparison of the adsorption kinetics and the numerical model. The average purity of the recovered CO_2 and the CO_2 recovery will be calculated using the last cycle. As mentioned in section 4.2 the results obtained during the investigation of the heat transfer characteristics were used for the simulation of the adsorption process that is described in the following sections.

4.4.1 Flue gas 1

The Bosanquet equation (see equation 2.8) is used for describing the adsorption kinetics for the first simulated dry flue gas (15.2% CO_2). The following discussion only considers the results obtained from the experiment with a regeneration temperature of 180 °C. The results obtained for the remaining temperatures show a similar agreement with the experimental measurements (see appendix A). Figure 4.21 illustrates the results for the regeneration temperature of 180 °C. During adsorption the simulated concentration profile is slightly flatter at the beginning than the measurement. This small deviation could be explained by the adsorption kinetics, meaning the calculated kinetics in the numerical model is slower than the actual kinetics. The temperature peaks calculated by the numerical model are in agreement with the experimental measurements. Nevertheless, the temperature peaks of TE6 and TE5 are slightly shifted in the simulation. This small shift could be explained by flow disturbances, which can cause thermal effects, since low pressures and low velocities are used during the experiments, indicating low Péclet numbers (Pe<5). Therefore, a maldistribution of the flow could be expected. Since the homogeneous model is used for the numerical model, a plug flow is assumed across the bed and therefore radial flow disturbances cannot be accounted for explicitly. Nevertheless, in an industrial plant the superficial velocity would be higher, which would minimize these effects since the Péclet number would be higher (Pe>30). If the error of the thermocouples is taken into account (± 2.5 K), the deviation between the model and the experiments is small. Therefore, the agreement between the model and the experiments is strong. Figure 4.21 also shows that the shape of the partial breakthrough curve is not symmetrical. This may indicate that during the adsorption step, a significant thermal influence exists. This can also be deduced by the temperature profiles, since they show a long tailing after the temperature peak.

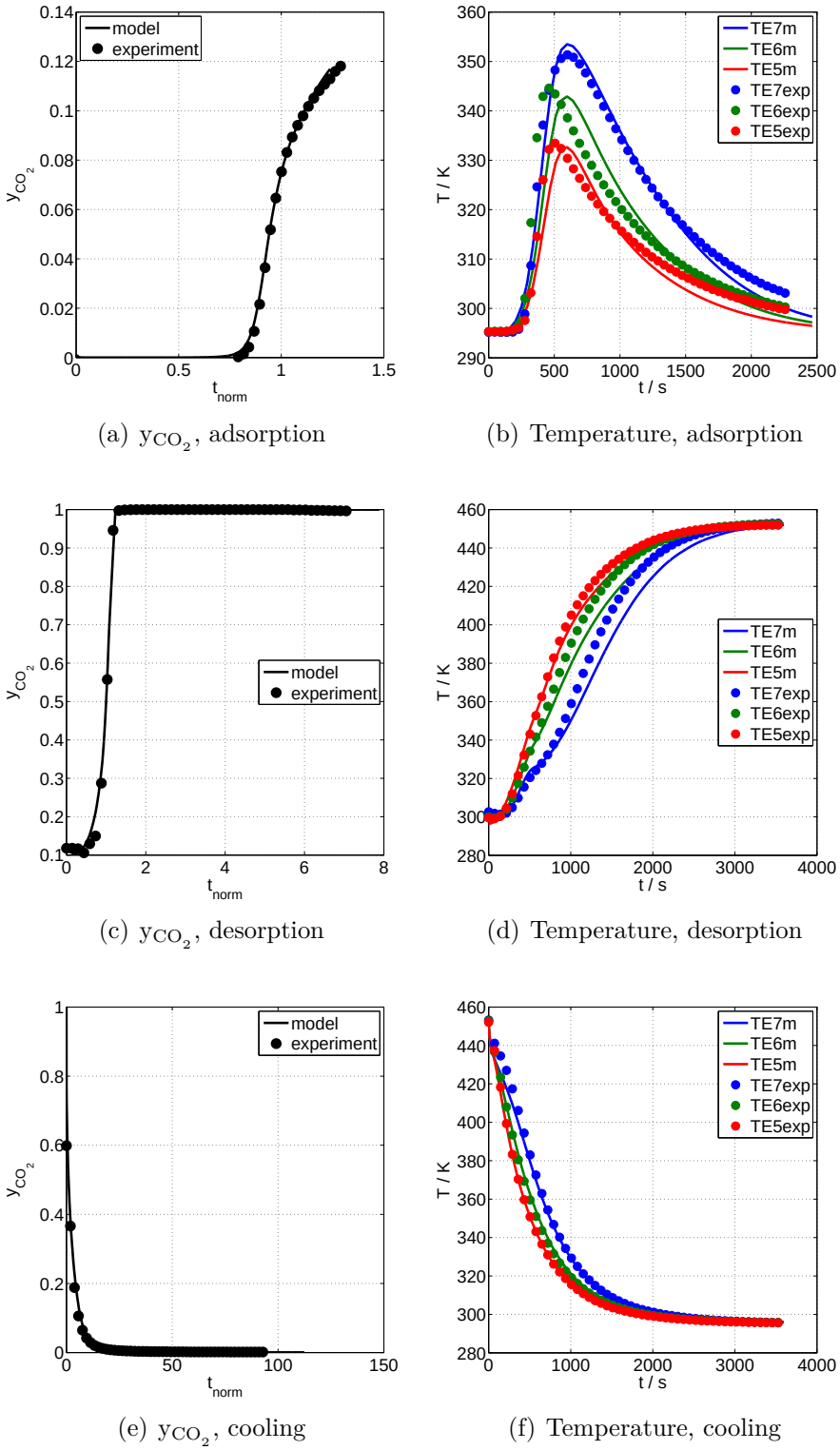

(a) y_{CO_2}, adsorption

(b) Temperature, adsorption

(c) y_{CO_2}, desorption

(d) Temperature, desorption

(e) y_{CO_2}, cooling

(f) Temperature, cooling

Figure 4.21: Concentration and temperature profiles for the first simulated dry flue gas using a regeneration temperature of 180 °C. The adsorption time is normalized by the time in which 50% of the inlet concentration is measured at the outlet. For the desorption and cooling, the time is normalized by the time in which the concentration at the outlet is equal to 50%.

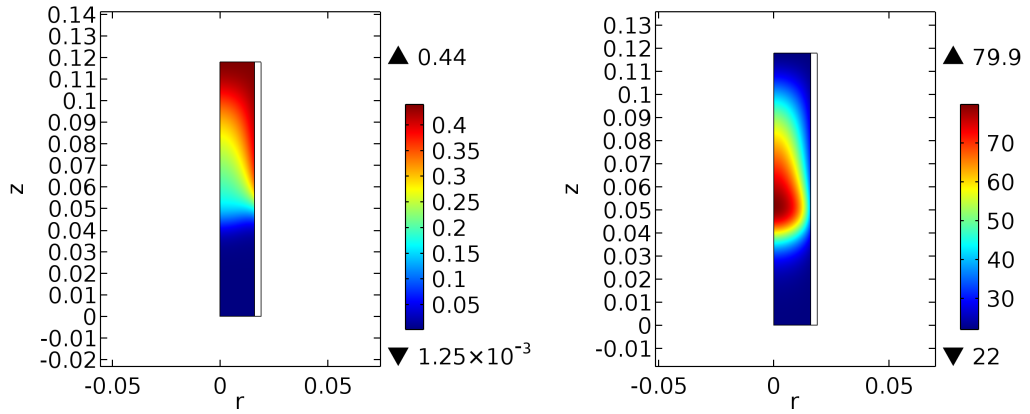

(a) CO_2 relative loading (b) Temperature

Figure 4.22: CO_2 loading and temperature during the adsorption step after 1000 s.

This indicates, that the heat is not being removed effectively. In order to prove the thermal influence, the 2D CO_2 loading profile is calculated using the numerical model. The thermal influence can be clearly observed in Figure 4.22, since the loadings of CO_2 are higher in the vicinity of the wall than at the center of the tube. If the 2D temperature profile is observed, the heat is not being removed effectively. This indicates, that because of the low Péclet number in the experimental setup the radial effective thermal conductivity is not high enough to remove the heat caused by adsorption fast enough, which leads to reduction of the CO_2 loading capacity. Nevertheless, for higher Péclet numbers, which will be the case on an industrial or pilot scale, an increase in the radial effective heat conductivity can be expected and therefore, the radial energy output will be more effective and the thermal influence will be reduced significantly. The fact that the numerical model is capable of predicting this phenomenon shows the validity of the model.

During desorption, there is a steep increase in the CO_2 concentration, which the numerical model can also predict as observed in Figure 4.21. The reason for the steep increase can be explained because of the absence of a purge gas. The fact that the numerical model predicts the steep increase indicates that in this case the desorption kinetics is predicted accurately in the numerical model. One can therefore assume, that the temperature dependency of the kinetic parameter is being calculated correctly. The desorption temperature profiles show a strong agreement at the beginning of the desorption step. Afterwards, the numerical model shows a slower increase in temperature, especially TE7. This slower increase could be explained by the desorption energy or the amount of CO_2 that desorbs. As mentioned earlier, the fact that the adsorption isotherm is scaled leads to uncertainties, especially at high temperatures because of extrapolation between the actual loading of CO_2 and the calculated one. Therefore, a discrepancy is expected which will lead to a deviation in the amount recovered during the desorption step, and therefore influence the temperature profiles during the desorption step. Nevertheless, the agreement between the model and the

measurements is strong considering the uncertainty caused by the isotherm.

The agreement of the CO_2 concentration during the cooling step between the model and the measurement is illustrated in Figure 4.21. The numerical model shows a good agreement. The temperature during the cooling step on the other hand shows a small discrepancy at the beginning of the cooling step. This small discrepancy can be explained by the inlet boundary condition in the model since it is assumed that the gas enters the bed with a homogeneous temperature, which is not the case in the experimental setup. The actual temperature profile will show a radial profile in which the temperature at the center will be colder than in the vicinity of the wall. Nevertheless, this influence is small as illustrated in Figure 4.21.

In general, the numerical model shows good results regarding its agreement with the experimental measurements, since it is capable of predicting the shape of the concentration and the temperature profiles with a high degree of accuracy.

In order to increase the agreement of the numerical model and the experimental measurements regarding the CO_2 concentration during the adsorption step, the Bosanquet equation is scaled:

$$D_{\text{model}} = m_{\text{scale}} \cdot D_{\text{overall,1}} \tag{4.11}$$

The obtained results if for the scaling parameter m_{scale}=1.5 is used can be observed in Figure 4.23. The improvement of the agreement between the CO_2 concentration of the model and the measurements at the beginning of the breakthrough during the adsorption step is illustrated in Figure 4.23. The increase in kinetic causes a slight

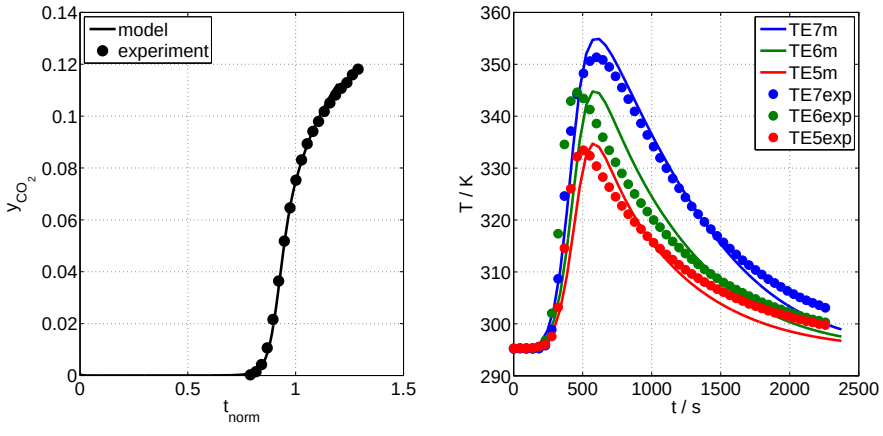

(a) y_{CO_2}, adsorption (b) Temperature, adsorption

Figure 4.23: Concentration and temperature profiles for the adsorption step of the first simulated dry flue gas using a regeneration temperature of 180 °C and scaling the adsorption kinetic parameter by 1.5. The adsorption time is normalized by the time in which 50% of the inlet concentration is measured at the outlet.

increase in the temperature peaks. Nevertheless, the agreement is still strong and did not change significantly from the previous case (see Figure 4.21). Since only the adsorption kinetics are changed, no significant change is observed during desorption and cooling.

The CO_2 recoveries during the desorption step and the average purities of the recovered CO_2 can be observed in Figure 4.24. The recovery increases as the regeneration temperature increases. This is also expected since high regeneration temperatures lead to low CO_2 loadings, meaning more CO_2 can be desorbed and recovered. On the other

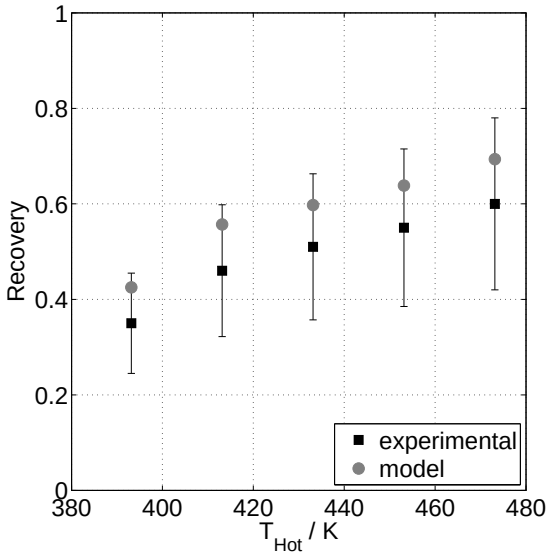

(a) Recovery

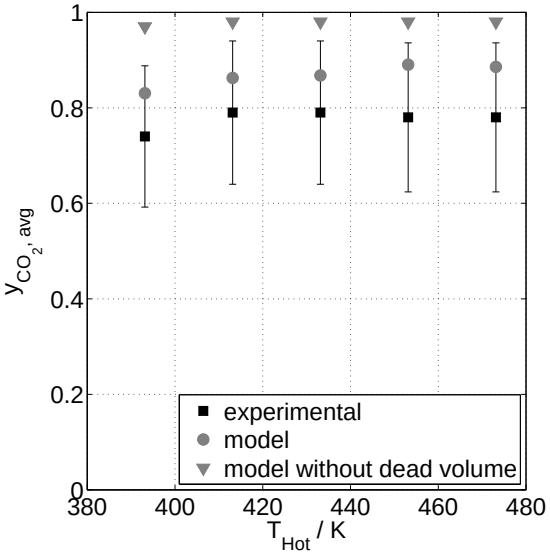

(b) Average recovered CO_2 purity

Figure 4.24: Recovery and average purity of the recovered purity for the different regeneration temperatures of the first simulated dry flue gas.

hand, no significant increase in the average purity of the recovered CO_2 can be observed with increasing regeneration temperature. The reason for this is that compared to the amount of N_2 that is in the voids of the bed, the adsorbed amount of CO_2 is orders of magnitude higher. Therefore, since no purge gas is used, the amount that is released even for the lowest temperature is significantly higher than the amount of N_2 in the voids of the bed.

The model predictions deviate from the experimental measurements. As mentioned earlier, the fact that no high pressure is available during the measurements and that no purge flow is used during the desorption leads to a higher uncertainty, which must be taken into account. As mentioned in section 3.2.8, although it is difficult to measure with a high degree of certainty, the errors are below 30% and can be considered tolerable. On the other hand, the uncertainties reflect a statistical error. The calculated recovery is within the range of the experimental error and shows the increasing tendency with increasing regeneration temperature. Since only a fraction (12 cm) of the adsorber tube is filled with adsorbent, a large dead volume must be considered, which is mainly filled with N_2. Therefore, the ratio of adsorbent mass to dead volume is high. In order to keep the numerical effort tolerable, the dead volume is not explicitly considered in the model. Instead, the amount of N_2 that is filled in the dead volume is added to the amount of gas that exits the adsorber tube during the regeneration step. The calculated average CO_2 purities show a small discrepancy to the measured values, but lie within the experimental error as illustrated in Figure 4.24. On an industrial or pilot scale, the influence of dead volume will be significantly lower since the ratio of adsorbent mass to dead volume will decrease considerably. If the amount of N_2 that is filled in the dead volume is not added to the gas that exits the adsorber tube during the regeneration step, meaning if the dead volume is not considered, higher purities than those measured can be achieved, as illustrated in Figure 4.24. This indicates that on an industrial or pilot scale significantly higher purities can be expected than those measured in this work.

4.4.2 Flue gas 2

The scaled Bosanquet equation (m_{scale}= 1.5) is used to describe the adsorption kinetics for the second flue gas (5% CO_2).The following discussion is conducted using only the results obtained from the experiment with a regeneration temperature of 180 °C since the results for the remaining experiments show similar agreements (see appendix B). Figure 4.25 illustrates the agreement between the simulation and the experiments; the agreement between the model and the measurements is accurate for the CO_2 concentration at the outlet during the adsorption step. This good agreement shows that the model is able to predict the kinetics over a wide range of CO_2 concentrations. The temperature profiles during adsorption on the other hand show a deviation between the model and the measurements. The model predicts lower temperature peaks than the measured ones.

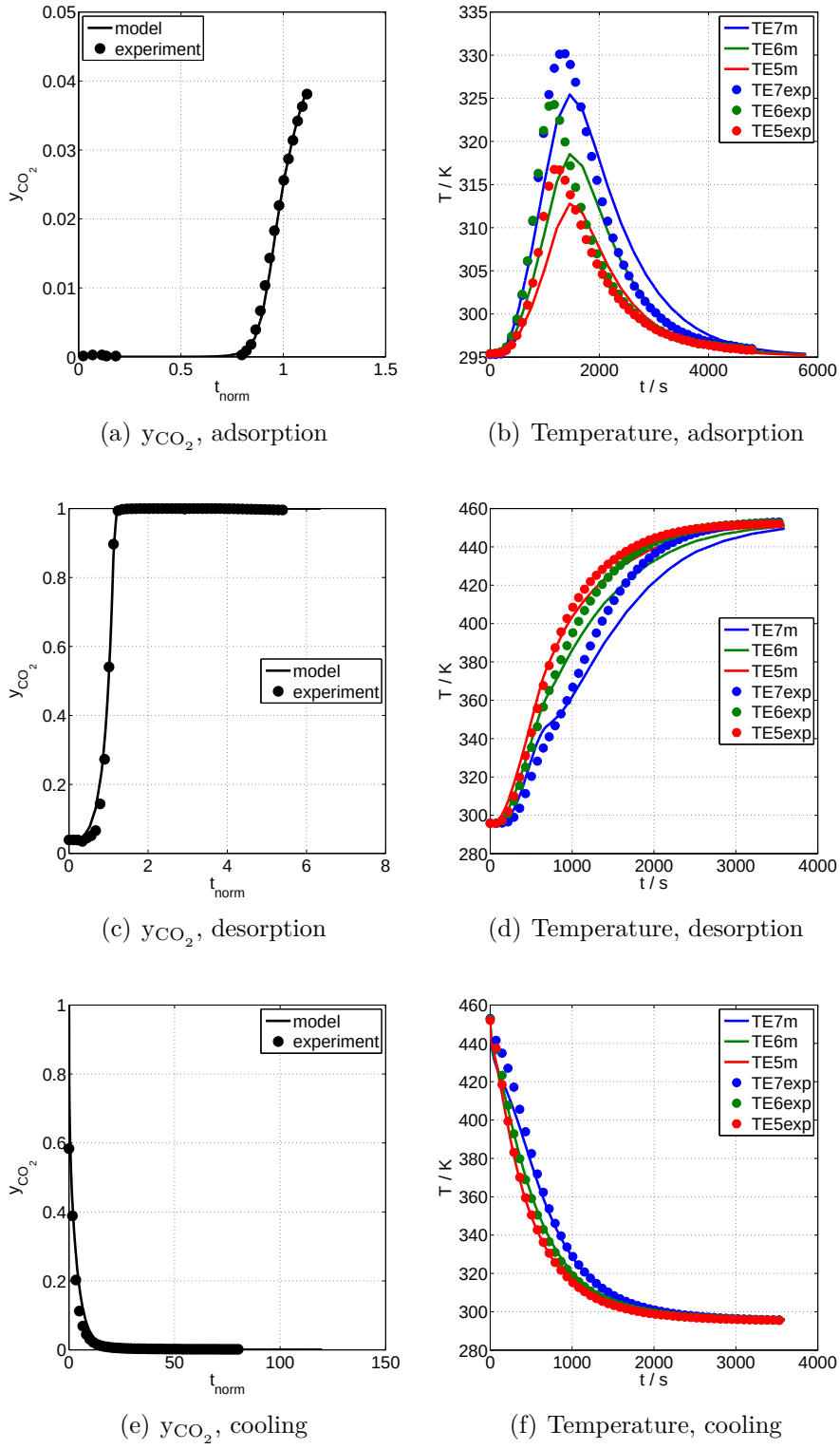

(a) y_{CO_2}, adsorption

(b) Temperature, adsorption

(c) y_{CO_2}, desorption

(d) Temperature, desorption

(e) y_{CO_2}, cooling

(f) Temperature, cooling

Figure 4.25: Concentration and temperature profiles for the second simulated dry flue gas using a regeneration temperature of 180 °C. The adsorption time is normalized by the time in which 50% of the inlet concentration is measured at the outlet. For the desorption and cooling, the time is normalized by the time in which the concentration at the outlet is equal to 50%.

This deviation can be explained by the uncertainty of the isotherm, which will also influence the adsorption enthalpy. Therefore, it is likely that the model under predicts the temperature peaks. Nevertheless, the discrepancy is maximal 5 K and can be considered as minimal if the error of the thermocouples is considered. The temperature profiles during adsorption also show that the peaks are slightly shifted. This shift can again be explained by possible flow disturbances because of the low Péclet number (Pe<5). Nevertheless as mentioned earlier, on an industrial or pilot scale, higher Péclet numbers (Pe>30) are envisioned which would minimize these effects. Another reason for the shift of the temperature peaks may be the scale factor of the isotherm. The scaling of the isotherm though necessary, is a source of uncertainty which has to be kept in mind. Therefore, a combination of the low Péclet number and the uncertainty of the isotherm can explain the small shift of the temperature peaks. Nonetheless, despite the existing uncertainties, the agreement between the model and the measurement can be considered strong since the deviation can be considered tolerable. The model and the measurement show a smaller tailing of the temperature after the peak is reached during adsorption. This would indicate, that the thermal effects, because of adsorption, are lower than in the previous case. The fact that the amount to be separated in this case is three times lower than in the previous case explains the lower thermal effects. To validate this, the 2D loading and temperature profiles are calculated in the numerical model, as is illustrated in Figure 4.26. It is clear that there are still thermal effects since the loadings show lower capacities at the center than at the vicinity of the wall. Nevertheless, compared to the previous case, one can clearly observe that these effects are reduced. This can also be seen by the experimental partial breakthrough curves as illustrated in Figure 4.27. If the thermal effects are similar, the shape of the normalized concentration profiles would have to be similar. Nevertheless, Figure 4.27 shows that the profile of the first flue gas shows a longer tailing at the end. This clearly indicates that the thermal effects are lower for the second flue gas than for the first flue gas.

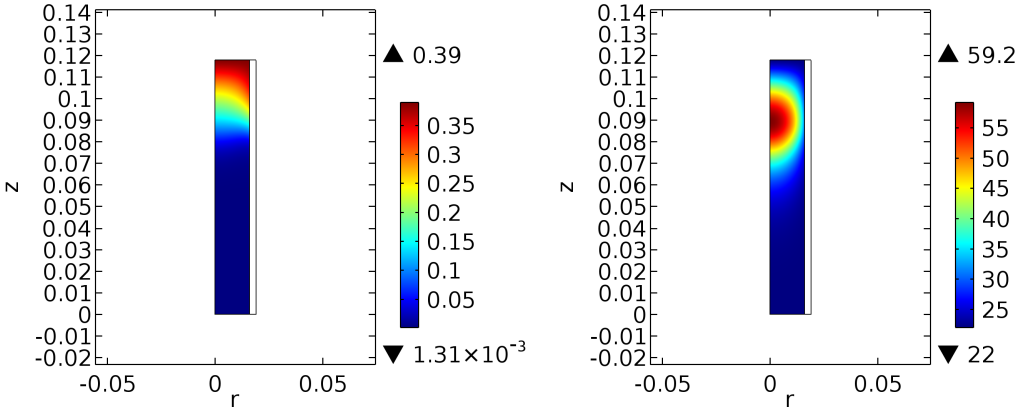

(a) CO_2 relative loading (b) Temperature

Figure 4.26: CO_2 loading and temperature during the adsorption step after 1000 s for the second simulated dry flue gas.

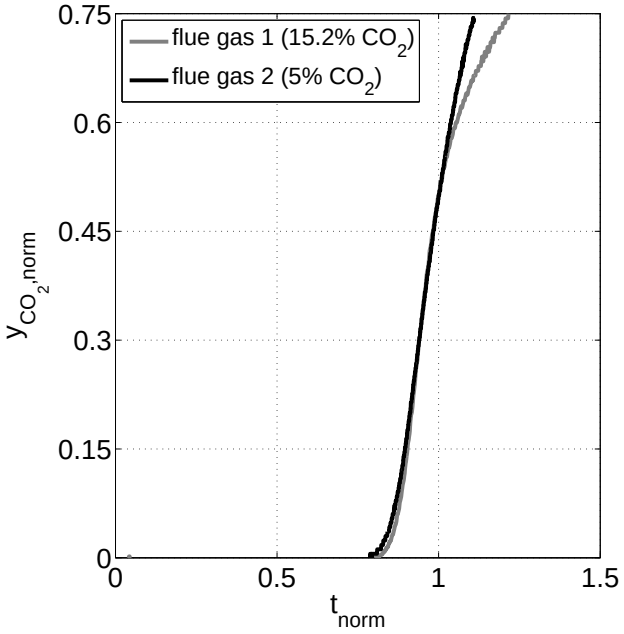

Figure 4.27: Normalized experimental partial breakthrough curves for both flue gases.

During the desorption step, a steep increase in the concentration can again be observed, which is predicted accurately by the model. As mentioned earlier, this steep increase can be explained by the absence of a purge gas. Similar to the previous case, the temperature profile during the desorption step shows a strong agreement at the beginning, and afterwards it shows a higher discrepancy. As mentioned previously, the uncertainty caused by scaling the isotherm can explain this discrepancy. Nevertheless, the agreement between the model and the measurements is satisfactory considering the uncertainties caused by the isotherm.

The model predicts the concentration profiles during the cooling step accurately as illustrated in Figure 4.25. The temperature profiles on the other hand show a small deviation at the beginning of the cooling step. As mentioned earlier, this deviation can be explained by the boundary condition, since it is assumed, that the gas enters the bed with a homogeneous temperature which is not the case during the measurement. Nevertheless, as in the previous case, the influence is small and the agreement between the model and the measurements can be considered good.

The CO_2 recoveries and the average purity of the recovered CO_2 can be observed in Figure 4.28. Similar to the previous case, the recovery increases as the regeneration temperature increases, since high regeneration temperatures lead to low CO_2 loadings, indicating that more CO_2 can be desorbed and recovered. If the recoveries are compared to the previous case, one can see that similar results are obtained. This is due to the experimental procedure since in both cases the adsorption step is finished as soon as 75% of the inlet concentration is measured at the outlet. Therefore, the recoveries have to be similar in both cases. On the other hand, a small increase in the average

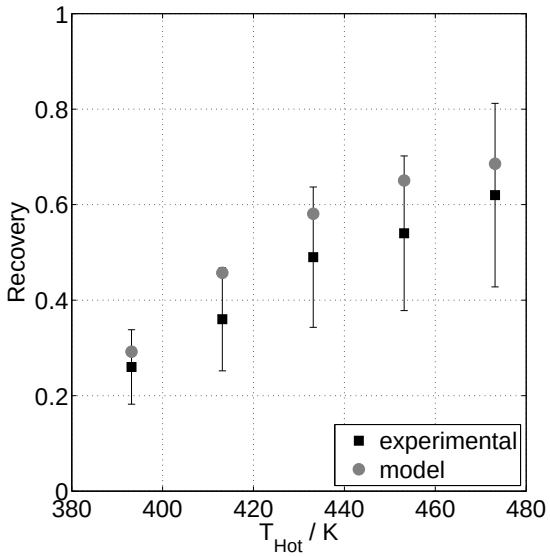

(a) Recovery

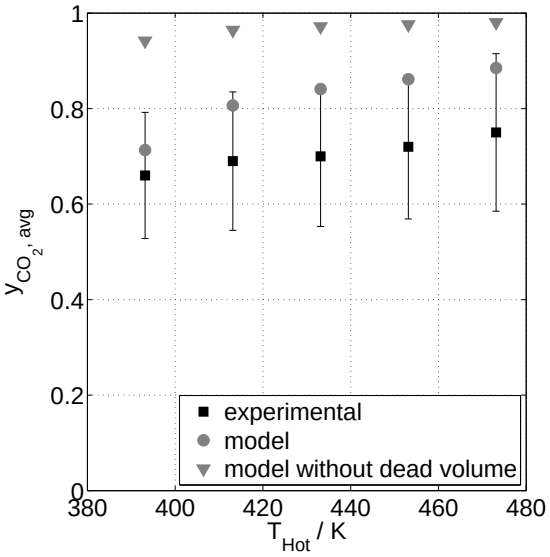

(b) Average recovered CO_2 purity

Figure 4.28: Recovery and average purity of the recovered purity for the different regeneration temperatures of the second simulated dry flue gas.

purity of the recovered CO_2 can be observed with increasing regeneration temperature. If these results are compared with the previous case, one can see that this increase in purity is more evident in this case than in the previous case. The reason is that less CO_2 is adsorbed on the adsorbent and the amount of N_2 in the voids is increased slightly. Therefore, the amount of N_2 will have a higher impact on the purity than in the previous case. Nevertheless, the amount of CO_2 that desorbs is still higher than the amount of N_2 in the voids and therefore, high purities are still achievable, especially at higher regeneration temperatures. Nonetheless, it is clear that the lower the inlet concentration, the higher the impact of the N_2 in the voids. Therefore, higher average

purities of the recovered CO_2 during the desorption step will be achieved if the inlet concentration is high and the same process scheme is used: adsorption, desorption with no purge gas, and cooling.

Similar to the previous case, the recoveries deviate from the calculated values from the experiments because of the uncertainty that is caused by the absence of purge gas and the measuring instruments. In this case the calculated recovery lies within the range of the experimental error and shows the increasing tendency with increasing regeneration temperature. A discrepancy between the measured average purity of the recovered CO_2 and the calculated average purity by the model with dead volume can be observed as in the previous case. Nevertheless, the calculated values lie within the experimental error. If the dead volume is not considered, meaning the conditions on an industrial or pilot scale are simulated, higher purities than the measured purities can be achieved, as can be observed in Figure 4.28.

5 Simulation of the indirectly heated adsorption process for capturing CO_2 from a coal fired power plant

In the previous section, the applicability of the derived model with the estimated parameters was confirmed. Therefore, the industrial process can be simulated with a high degree of accuracy using the derived model since the diameter of the tube used during the experimental measurements is the same as the proposed diameter for the tubes in the industrial process. The influence of dead volume is significantly lower on an industrial scale and will therefore be neglected in the coming numerical study. As shown in the previous section where the influence of the dead volume was illustrated, high purities of the recovered CO_2 can be expected. On an industrial or pilot scale a thermal fluid will be flowing through the shell of the tube bundle. Therefore, the boundary condition used during the experimental measurements, constant wall temperature, will not be equivalent. During the investigation of the heat transfer characteristics of the adsorbent bed without convection it was observed that the estimated parameters do not significantly depend on the boundary condition. Therefore, one can assume that the obtained results from the simulations will be predicted accurately. The boundary condition used for the coming simulation is the condition described in section 2.3: heat transfer from a heat transfer fluid.

A flue gas emitted from a coal fired power plant was considered in the numerical study.

In order to characterize the quality or performance of the CO_2 capture process using the indirect heated and cooled adsorption process, three different key performance indicators are used. The first indicator is the purity of the recovered CO_2 during the heating step since high purities (>95%) reduce the sequestration costs [9].

$$\text{Purity} = \frac{\int_0^{t_{\text{des}}} \left(\int_A (u_z c_{\text{CO}_2})|_{z=0} \mathrm{d}A \right) \mathrm{d}t}{\int_0^{t_{\text{des}}} \left(\int_A (u_z c)|_{z=0} \mathrm{d}A \right) \mathrm{d}t} \tag{5.1}$$

The second indicator is the CO_2 recovery during the heating step since it delivers information about the quality of the capturing process,

$$\text{Recovery} = \frac{\int_0^{t_{\text{des}}} \left(\int_A (u_z c_{\text{CO}_2})|_{z=0} \mathrm{d}A \right) \mathrm{d}t}{\int_0^{t_{\text{ads}}} \left(\int_A (u_z c_{\text{CO}_2})|_{z=0} \mathrm{d}A \right) \mathrm{d}t + \int_0^{t_{\text{cool+press}}} \left(\int_A (u_z c_{\text{CO}_2})|_{z=\text{H}} \mathrm{d}A \right) \mathrm{d}t} \tag{5.2}$$

and the last indicator is the required specific energy since this gives information about the energetic efficiency of the capturing process. The specific energy is determined from the heat exchanger between the "hot" and "cold" tube bundle vessel as illustrated in Figure 5.1.

$$\mathrm{Q_{specific}} = \frac{\int_0^{t_{\mathrm{cool+press}}} \left(\dot{M}_{\mathrm{HEX}} \cdot c_{\mathrm{p,HEX}}\right)|_{z=0} \left(T_{\mathrm{Hot}} - T_{\mathrm{HEX}}(z=0)\right) \mathrm{d}t}{\mathrm{CO_2\ recovered}} \left| \frac{\mathrm{MJ}}{\mathrm{kg_{CO_2,rec}}} \right| \tag{5.3}$$

For the numerical study, the co-adsorption of N_2 is neglected since under adsorption

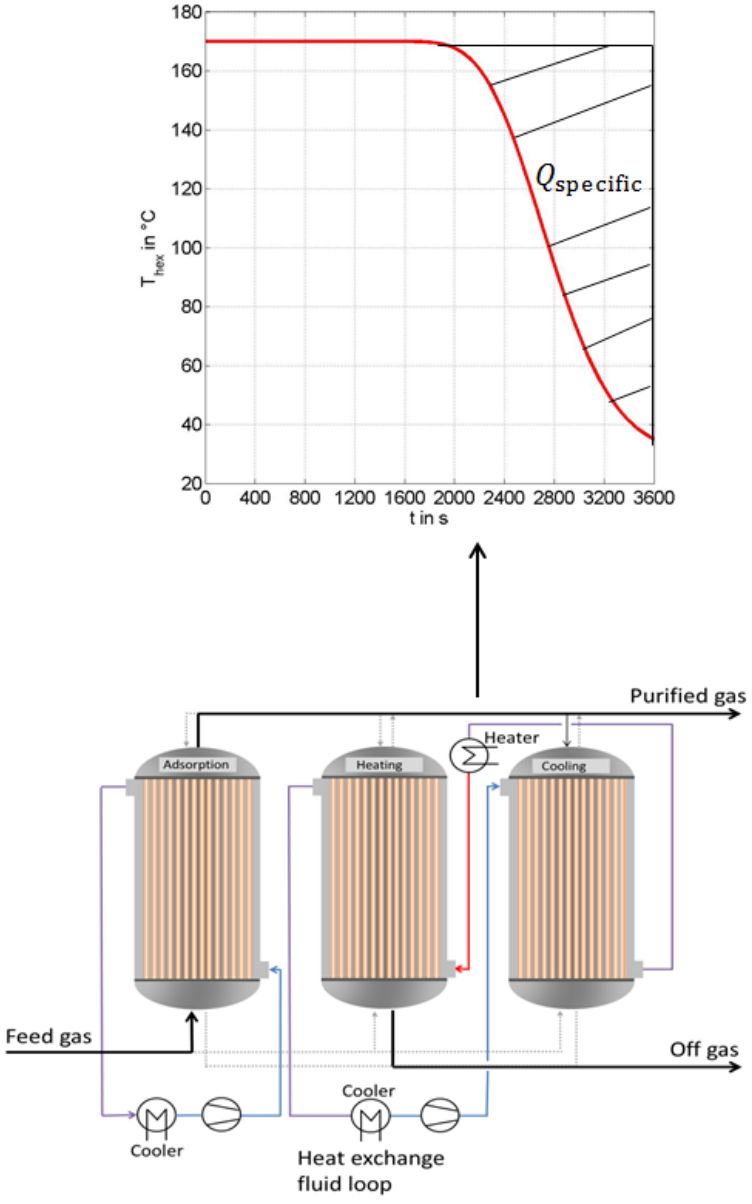

Figure 5.1: Estimation of the specific energy.

and desorption conditions, 99% of the total adsorbed amount would be CO_2 according to the Ideal Adsorption Solution Theory (IAST) [44]. This study was conducted using Comsol and the LiveLink. A triangular mesh with 60048 volume elements and 7526 surface elements was used for the 2D geometry (adsorbent bed and interstitial gas phase, tube wall). For the 1D geometry 5000 volume elements were used. Only one tube from the tube bundle is modeled under the assumption that all tubes behave equally in the tube bundle [105]. This simplifies the simulation as it reduces the computational time significantly. Table 5.1 illustrates the values used for the tube geometry and for the separation process.

The performance of the process measured by the three key performance indicators using the estimated parameters (e.g. λ_p) and assuming a fixed value for the outer heat transfer coefficient (see Table 5.1) can be taken from Table 5.2. It can be observed, that a high purity (>98%) and a satisfactory recovery can be achieved. Nevertheless, the recovery is below the target value for CCS (90% [8]). The specific energy demand is similar to that obtained by Clausse et al. [40] during their numerical investigation of

Table 5.1: Geometry values and process values used in this study and parametrical field.

Parameter	Value	Variation field
Geometry		
H in m	5	
d_o in cm	d_i+0.5	
d_i in cm	3.2	2 / 3.2/ 4.4
Process		
T_0 in °C	30	
T_{Hot} in °C	180	120/140/160/180/200
p_∞ in bar	1.013	
$\dot{V}_n$ in $^{Nm^3}/_{h\cdot tube}$	0.95	
$y_{CO_2,in}$ in %	15	
$y_{N_2,in}$ in %	85	
Adsorbent	13X	
λ_p in $^{W}/_{m\cdot K}$	0.39	0.2/0.4/0.6/0.8/1
Bi	1.14	
K_{Rad}	9.55	
$D_{overall}$ in $^{m^2}/_{s}$	equation 2.8	
Adsoprtion isotherm	see section 4.3	
$\dot{M}_{HEX,z}$ (adsorption) in $^{g}/_{s\cdot tube}$	5.1	
$\dot{M}_{HEX,z}$ (heating) in $^{g}/_{s\cdot tube}$	1.7	
$\dot{M}_{HEX,z}$ (cooling+pressurization) in $^{g}/_{s\cdot tube}$	1.7	
α_{HEX} in $^{W}/_{m^2\cdot K}$	500	150/250/350/450/550

Table 5.2: Process performance.

Key perfromance indicator	Value
Purity in %	98.6
Recovery in %	82.5
$Q_{specific}$ in $^{MJ}/_{kg_{CO_2,rec}}$	3.25

a coaxial heat exchanger with fins for carbon capture. Comparing the obtained value with the benchmark process, the amine wash (≈ 2.7 $^{W}/_{m^2 \cdot K}$ [17]), it is clear that the specific energy demand is still higher.

Since neither the recovery nor the specific energy demand satisfy the process requirements, a parametrical sweep is conducted in order to investigate the influence of several parameters on the process performance, measured by the key performance indicators. Geometrical, process, and physical properties are chosen for the parametrical study. The different parameters and the variation field are shown in Table 5.1.

5.1 Variation of the outer heat transfer coefficient

The influence on the key performance indicators by varying α_{HEX} are illustrated in Figure 5.2. The CO_2 purity is not influenced strongly due to the absence of a purge gas. Since no purge gas is used, the desorbed CO_2 will not be diluted. Furthermore, since the highest expected thermal resistance is inside the bed, a relatively good heat transfer to the wall during the heating step can be achieved even for the lowest outer heat transfer coefficient. Therefore, one can assume, that the regeneration is acceptable

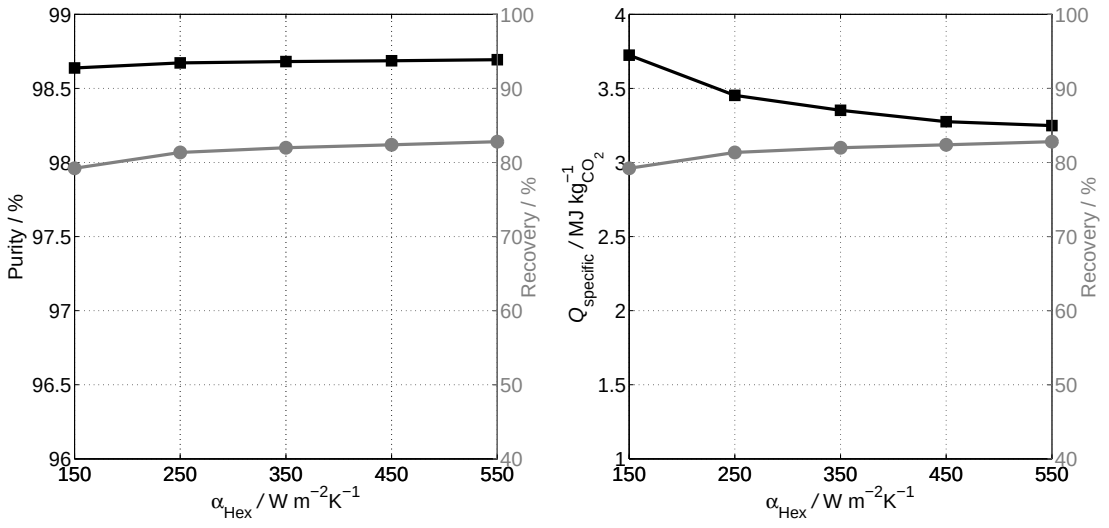

(a) Purity and recovery

(b) required specific energy and recovery

Figure 5.2: Influence on the key performance indicators by varying α_{HEX}.

in all cases, which implies that the amount of desorbed CO_2 is high. Since the amount of N_2 in the voids of the bed is small compared to the amount of CO_2 adsorbed one can assume that no significant dilution of the desorbed CO_2 occurs.

It can be observed from Figure 5.2 that the influence of the outer heat transfer coefficient on the recovery is small. This can be explained by the fact that since the packed bed is the main thermal resistance an increase in the outer heat transfer coefficient will not lead to a noticeable improvement. In order to increase the recovery, meaning reduce the thermal resistance, an improved heat transfer inside the packed bed would have to be achieved. Therefore, no significant influence on the purity or recovery is observed by varying the outer heat transfer coefficient.

On the other hand, the specific energy requirement decreases by increasing the outer heat transfer coefficient. This influence can be explained by the fact that the higher the outer heat transfer coefficient is, the sharper the outlet temperature is during the cooling+pressurization step. This phenomenon is illustrated in Figure 5.3. This sharpening of the temperature front can also be expected since the convective heat transfer is kept constant and the heat transfer from the wall is increased. Therefore, if for a given time a control volume is observed the heat transferred to the fluid can heat the fluid more before it exits that control volume. To further illustrate this phenomenon a simulation is made in which the packed bed is at a high temperature and a fluid is flowing through the shell of the tube bundle to cool the bed inside the tubes. Inside the tubes adsorption is neglected and it is assumed that N_2 is the interstitial gas. Also, no flow inside or outside the tubes is assumed. The obtained profiles can be seen in Figure 5.4 where the described phenomena can be seen more markedly. Rezaei et al. [33] made similar observations for their hollow fiber system, which can be compared to a

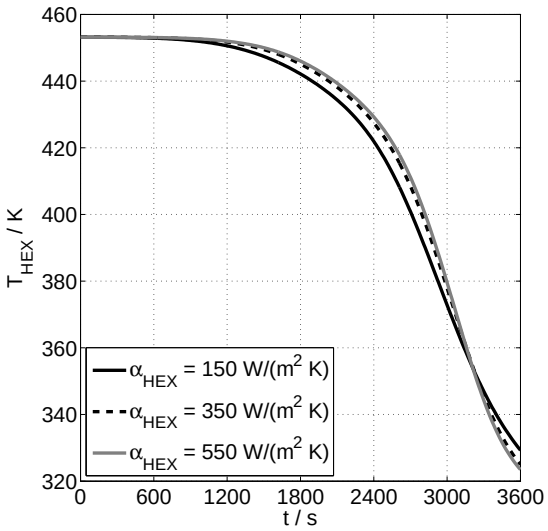

Figure 5.3: Heat exchanging fluid temperature profile at the outlet of the adsorber for different outer heat transfer coefficients α_{HEX}.

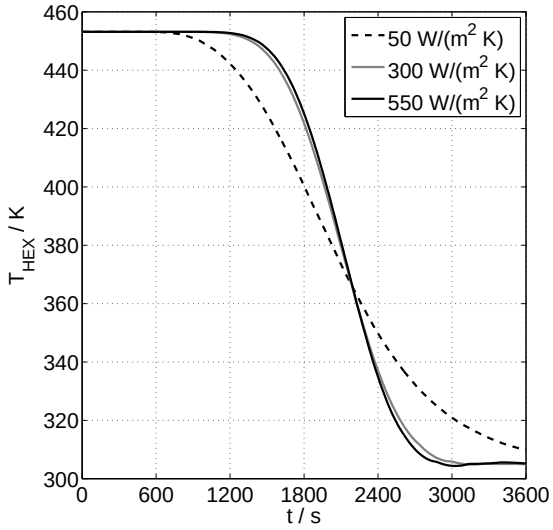

Figure 5.4: Sharpening effect of the temperature profile of the heat exchanging fluid at the outlet during a cooling step by increasing the outer heat transfer coefficient α_{HEX}.

heat exchanger, regarding the interaction between convective heat transfer and heat transfer from a body.

5.2 Variation of the heat conductivity of the solid particle

An increase or decrease in the heat conductivity of the solid particle λ_{p} would influence the effective heat conductivity of the bed λ_{bed} directly. An increase in λ_{p} would lead to an increase in λ_{bed}, which means that the radial thermal resistance will be decreased. On the other hand, if λ_{p} is decreased the thermal resistance of the bed is increased since λ_{bed} is decreased. Figure 5.5 illustrates the influence of the heat conductivity of the solid particle λ_{p} on the key performance indicators. The purity is not influenced significantly. As mentioned in the last section, this result can be explained by the absence of a purge gas. Moreover, since an increase in λ_{p} will lead to a reduction in the radial thermal resistance, an equal or better regeneration can be expected. Therefore, either more or equal amounts of CO_2 can be desorbed during the heating step, keeping the high average purity of the recovered CO_2.

It can be expected, that the amount of CO_2 that can be recovered increases by increasing λ_{p}, since the radial thermal resistance would be reduced. This is demonstrated in Figure 5.5. The fact that the increase in CO_2 recovery by increasing λ_{p} is not considerably high indicates that either the increase in λ_{p} has a small influence on the thermal resistance or that the regeneration temperature is more dominating. If the values for λ_{p} are inserted in equation (2.31) using a mean temperature of 105 °C and it

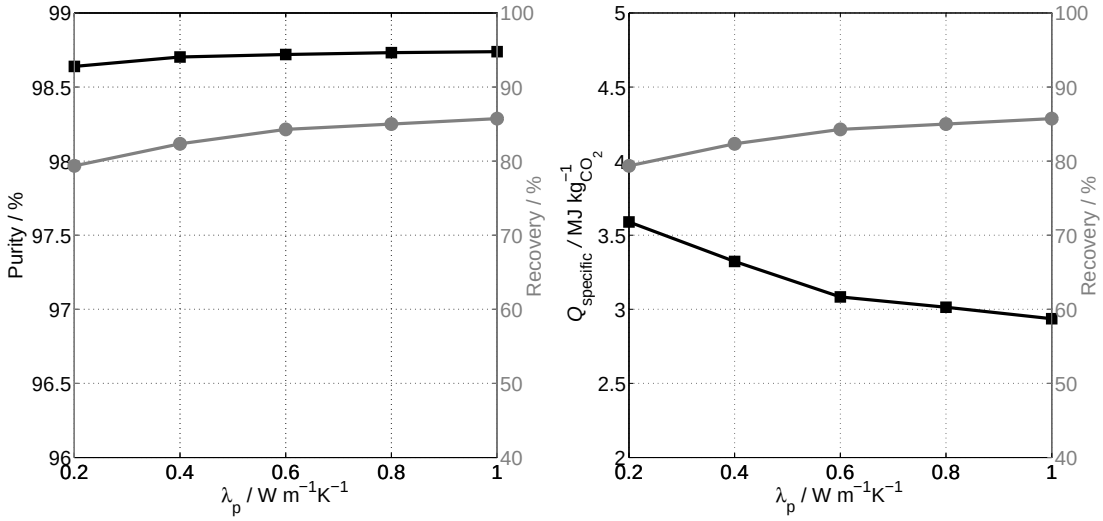

(a) Purity and recovery

(b) required specific energy and recovery

Figure 5.5: Influence on the key performance indicators by varying λ_p.

is assumed that the gas phase consists only of CO_2, one will observe that an increase in a factor of five in λ_p will cause an increase of around two in λ_{bed}. It is therefore clear that an increase in λ_p will have a significant influence on λ_{bed}. Nevertheless, a marked improvement in the recovery is not observed, which indicates that the bed is being regenerated satisfactorily even with the lowest value for λ_p. Therefore, an increase in λ_p will have a small influence on the recovery under the given process and boundary conditions. In order to confirm this, the average temperature of the adsorbent bed is tabulated for the different values of λ_p in Table 5.3. It is clear that the temperature change is not substantial, which confirms that even for the lowest value a good regeneration is achieved. On the other hand, if the regeneration temperature is changed, a significant influence would have to be observed.

Because of the reduction in the radial thermal resistance by increasing the heat conductivity of the solid particle, the specific energy requirement during the cooling + pressurization step is reduced as can be observed in Figure 5.5. The decrease in energy

Table 5.3: Average temperature of the adsorbent bed after the cooling step for the different values of λ_p.

Parameter value for λ_p	Adsorbent bed average temperature after cooling
0.2 $^{W}/_{m \cdot K}$	160 °C
0.4 $^{W}/_{m \cdot K}$	162 °C
0.6 $^{W}/_{m \cdot K}$	163 °C
0.8 $^{W}/_{m \cdot K}$	164 °C
1 $^{W}/_{m \cdot K}$	164 °C

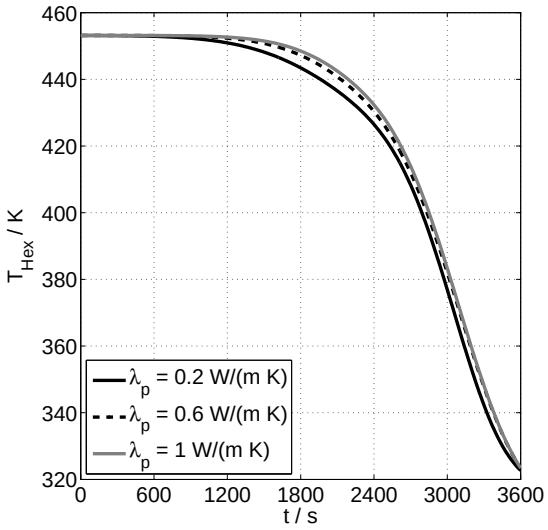

Figure 5.6: Heat exchanging fluid temperature profile at the outlet of the adsorber for different solid heat conductivities λ_p.

requirement by increasing λ_p can be explained by the sharpening of the temperature profile of the heat exchanging fluid at the outlet, as is illustrated in Figure 5.6. Since the heat transfer to the fluid is faster than the convective heat transfer and the heat conduction from the bed to the wall is also increased, the heat transfer fluid temperature profile at the outlet of the adsorber during the cooling + pressurization step is sharpened, which leads to a reduction of the energetic demand.

5.3 Variation of the heating temperature

The influence of T_{Hot} on the average recovered CO_2 purity can be observed in Figure 5.7. The average purity is reduced as the regeneration temperature is decreased. Low regeneration temperatures will lead to high CO_2 residual loadings as illustrated in Figure 5.8, meaning that less CO_2 can be recovered. Therefore, the influence of the interstitial N_2 on the average purity will increase since less CO_2 can be desorbed, but the amount of interstitial N_2 remains almost the same. Nevertheless, it can also be observed that even for the lowest regeneration temperature, high CO_2 average purities can be achieved. This can also be explained by the fact, that the amount of CO_2 adsorbed by the adsorbent is much higher than the amount of the interstitial gas and since no purge gas is used during the heating step. Therefore, even for the lowest regeneration temperature large amounts, compared to the interstitial gas, can be recovered.

Because of the increase of the residual loading after the heating step by decreasing the regeneration temperature lower recoveries are expected. This can also be seen in Figure 5.7. Even though high purities are achieved, the amount of CO_2 that can be recovered is not high at lower temperatures. It is therefore clear that high

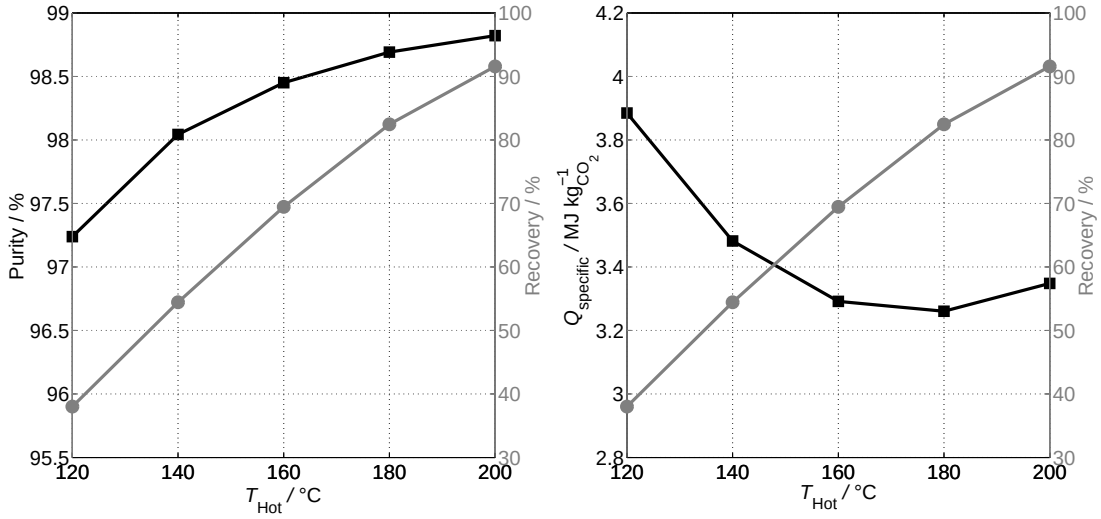

(a) Purity and recovery

(b) required specific energy and recovery

Figure 5.7: Influence on the key performance indicators by varying the regeneration temperature T_{Hot}.

temperatures (T_{Hot}>150°C) have to be chosen in order to obtain acceptable CO_2 recoveries during the heating step. The reason for the high temperatures is the high adsorption enthalpy of CO_2 on 13 X.

Figure 5.7 illustrates, that the specific energy requirement decreases to a minimum as the temperature increases. The existence of this minimum can be explained by the

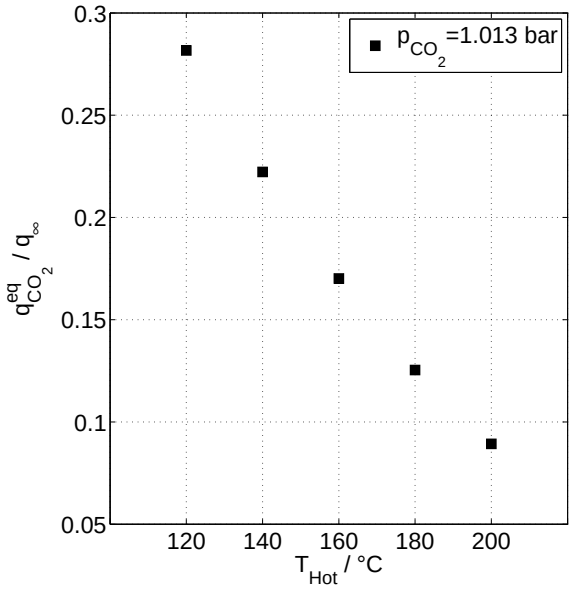

Figure 5.8: Influence of the regeneration temperature on the residual loading. The CO_2 partial pressure is 1.013 bar.

shape of the recovery curve since this curve does not increase linearly, meaning that the amount of CO_2 that can be recovered does not increase linearly with temperature. This can also be observed in Figure 5.8 since the CO_2 loading does not decrease linearly as the temperature is increased. Therefore, an increase in temperature above the optimal temperature will not lead to a significant improvement on the amount of CO_2 that can be recovered to compensate for the increase in energy input. This indicates that high temperatures will not lead to an improvement of the process since the specific energy requirement would increase.

5.4 Variation of the inner diameter

If the inner diameter is changed, then the ratio of incoming CO_2 to adsorbent mass will be changed. By changing the inner diameter, the outer diameter is changed, which will have a direct influence on $A_{\mathrm{HEX,tube}}$. An increase of the inner diameter will lead to a decrease in $A_{\mathrm{HEX,tube}}$ and hence reduce the axial velocity if the mass flow is kept constant. On the other hand, a reduction of the inner diameter would increase the axial velocity if the mass flow is kept constant. In order to keep the ratio of incoming CO_2 to adsorbent mass, which is important in order to compare the results and in order to have the same velocity for all cases, the following relations are used:

$$\frac{\text{Incoming } CO_2}{\text{Adsorbent mass}} = \left(\frac{d_i^2}{(3.2\text{ cm})^2}\right) \cdot \frac{\dot{V}_{\mathrm{n}} \cdot y_{\mathrm{CO_2,in}}}{(1-\epsilon)\rho_{\mathrm{p}} \cdot A_{\mathrm{tube}} \cdot H} \tag{5.4}$$

$$u_{\mathrm{HEX},z} = \left(\frac{d_o^2}{(3.7\text{ cm})^2}\right) \cdot \frac{\dot{M}_{\mathrm{HEX},z}}{\rho_{\mathrm{HEX}} \cdot A_{\mathrm{HEX,tube}}} \tag{5.5}$$

An increase in the inner diameter will also increase the void volume of the packed bed. This means more interstitial N_2 after the adsorption step which can dilute the desorbing CO_2 during the heating step. Moreover, since the radial length would be increased, a higher thermal resistance would exist, which leads to a lower regeneration during the heating step. This would also affect the average purity of the desorbed CO_2. Nevertheless, as can be observed in Figure 5.9, the influence on the average purity is not extensive due to the high amount of CO_2 that can be adsorbed compared to the amount of interstitial gas. Therefore, even if the thermal resistance is increased, the amount of CO_2 that is desorbed during the heating step is much higher than the interstitial N_2 and therefore the influence on the purity is not extensive.

As illustrated in Figure 5.9, the recovery is decreased by increasing the inner diameter due to the increase in the thermal resistance, which leads to a lower regeneration quality. This is reflected in the recovery since lower amounts of CO_2 can be desorbed during the heating step. On the other hand, reducing the inner diameter would reduce the radial thermal resistance which implies a better regeneration and therefore a higher CO_2 recovery. Nevertheless, it is important to keep in mind that decreasing the inner diameter can also lead to a significant influence of the bypass flow in the vicinity of

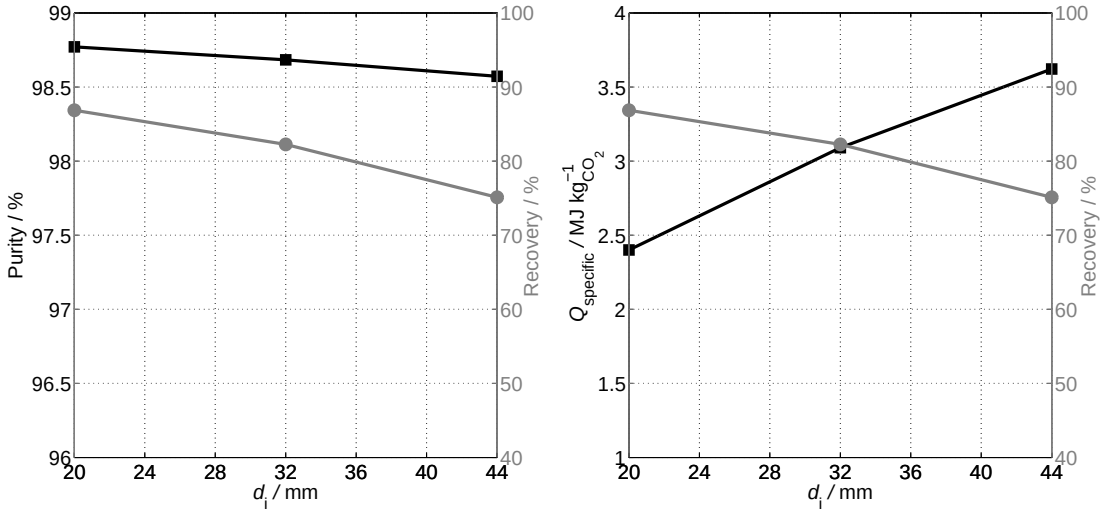

(a) Purity and recovery

(b) required specific energy and recovery

Figure 5.9: Influence on the key performance indicators by varying the inner diameter d_i.

the tube wall. This can lead to a negative influence on the process since more CO_2 can breakthrough during the adsorption step which reduces the CO_2 recovery. For the lowest value of the inner diameter, the d-to-d_p is slightly lower than the critical one (>10 [75]). Therefore, the question arises as to whether the α_w-model is still adequate. Nevertheless, the discrepancy between the d-to-d_p for the lowest investigated inner diameter and the critical one is not extensive which allows for the assumption that the α_w-model is still adequate. Nonetheless, the influence of a bypass flow in the vicinity of the wall for low d-to-d_p must be kept in mind when designing or investigating the indirect heated TSA process.

The specific energy requirement increases by increasing the inner diameter as can be observed in Figure 5.9. This can be explained by the increase in the thermal resistance, which leads to a slower heat transport from the center of the tube to the wall. This slower heat transport will spread the temperature front of the heat exchanging fluid and hence reduce the specific energy requirement. Moreover, the surface to volume ratio ϕ is decreased by increasing the inner diameter, which has an impact on the heat transfer to the heat exchanging fluid. This also spreads the temperature front of the heat transfer fluid and increases the specific energy requirement.

Changing the inner diameter will not only have an impact on the key performance parameters but it will also have an impact on the investment costs, since smaller tube diameters will lead to more tubes and bigger tube diameters to less tubes. This has to be kept in mind when designing the indirect heated TSA process.

5.5 Optimized parameters

The parametrical study showed that if the radial thermal resistance is reduced recoveries above the target value can be achieved. In addition, comparable specific energy requirements to the benchmark process can be envisioned. In order to determine how efficient this process can be a simulation is conducted using optimal parameters. The optimal parameter values used for this simulation and the obtained results for the key performance indicators are given in Table 5.4. As mentioned before it must be kept in mind that by using low d-to-d_p ratios, the influence of a bypass flow can have an influence on the results. Assuming that this influence is not significant since the d-to-d_p is not extensively lower than the critical one, it can be seen that high average purities and recoveries above the target value can be achieved. This can be explained by the significant reduction in the radial thermal resistance since the inner diameter is reduced and the heat conductivity of the solid particle is increased. Furthermore, a specific energy requirement lower than the reference value, which is around 2.7 $^{\mathrm{MJ}}/_{\mathrm{kg_{CO_2}}}$ [17], can be achieved. This reduction in the specific energy requirement can be explained by the fact that the reduction in the radial thermal resistance will lead to a better heating and cooling of the bed and a sharpening of the temperature front of the heat exchanging fluid at the outlet. Therefore, lower energy requirements can be achieved while keeping a high average purity and recovery of the CO_2 during the heating step.

Nevertheless, values as high as 1 $^{\mathrm{W}}/_{\mathrm{m\,K}}$ for the heat conductivity of standard 13 X particles are not realistic as can be deduced from section 4.1. In order to obtain such high heat conductivity enhanced materials such as structured adsorbents would have to be designed with high heat conductivity and high CO_2 capacity. Another possibility to reduce the radial thermal resistance is to use internal fins.

This numerical study shows that the indirect heated and cooled TSA process can

Table 5.4: Parameter values used for the optimized simulation and obtained results for the key performance indicators.

Parameter	Value
Parameter for simulation	
T_Hot in °C	180
d_i in cm	2
λ_p in $^{\mathrm{W}}/_{\mathrm{m\,K}}$	1
α_HEX in $^{\mathrm{W}}/_{\mathrm{m^2\,K}}$	550
Results	
Average purity in %	98.8
Recovery in %	91.3
Q_specific in $^{\mathrm{MJ}}/_{\mathrm{kg_{CO_2,rec}}}$	2.2

be an alternative for CCS if the adequate parameters are chosen. This would imply the development of new advanced material or advanced tube geometries (e.g. internal fins). The indirect heated and cooled TSA process opens the possibility of a new technology for CCS and for further material developments.

6 Conclusions and outlook

6.1 Summary

Indirect heated and cooled temperature swing adsorption processes offer the advantage of faster cycling and therefore a higher throughput. In addition, a bulk separation can be envisioned since the adsorbent bed is cooled indirectly during the adsorption step. Therefore, the indirect heated and cooled TSA process using a tube bundle adsorber could be applied to capture CO_2 from fossil fueled power plants. In this work, the heat transfer characteristics and the adsorption characteristics were investigated. A multidimensional mathematical model was derived to simulate the indirect heated and cooled TSA process.

In order to investigate the heat transfer and the adsorption characteristics, an existing experimental setup was modified. A new adsorber tube with an electrical heating and a cooling coil at the wall was designed. For the investigation of the heat transfer characteristics two different experimental procedures were chosen. The first one consisted of investigating the heat transfer without convection and the second one consisted of investigating the influence of convection at low Péclet numbers on the heat transfer.

To describe the heat transfer in a packed bed the homogeneous α_w-model was used. The effective heat conductivity of the bed without convection was modeled using the Zehner/Bauer/Schlünder-model. Two parameters were chosen to fit the model to the experimental measurements: The Biot number Bi and the heat conductivity of the solid particle λ_p. In order to investigate whether these parameters depend on the boundary condition, two different boundary conditions were chosen: constant wall temperature and constant heat duty. It was observed that both parameters are correlated. Moreover, small changes in λ_p lead to almost no change in the effective heat conductivity of the bed λ_{bed}, which is the actual model parameter. These observations were made for both boundary conditions. Even though the Biot number showed higher deviations than λ_p the model is more sensitive to a change in λ_p. Therefore, and since the values of λ_p and Bi did not change significantly between both boundary conditions, it can be assumed that these values are boundary independent. The most adequate values for the investigation of convection on the heat transfer and for the coming simulations were the mean values: λ_p=0.39 $^{W}/_{m\,K}$ and for Bi=1.14. Both values differ from the values in the literature. Using the correlation of Nilles, a value for the Bi number of 1.64 was obtained, which is higher than the estimated value. The correlation of Eurokin on the other hand gives a value closer to the measured one ($\approx$1). In the literature, no consistent value for the heat conductivity of the solid particle (molecular sieve 13 X) was found but the estimated value is between the range given in the literature (0.13-0.58 $^{W}/_{m\,K}$) [43].

The investigation of the influence of convection with low Péclet numbers was conducted only under one boundary condition since it was shown in the previous investigation that the boundary condition did not show a significant influence on the parameters. For the investigation, low velocities had to be chosen in order to avoid thermal inlet problems. To vary the Péclet number, the pressure of the system was changed. Three different Péclet numbers were achieved. The α_w-model was extended in order to consider the contributions of convection on the effective radial and axial heat conductivity. A convective contribution on the wall heat transfer coefficient α_w was also considered and both contributions were estimated using the experimental measurements. A correlation between both parameters was observed and a linear relationship between the convective contribution of the radial heat conductivity and the Péclet number was observed. This relationship is also demonstrated in the literature for higher Péclet numbers (Pe>50). For low Péclet numbers, no information regarding the correlation between the Péclet number and the convective contribution of the radial heat conductivity was found in the literature. The slope of the curve was compared with the slope obtained for higher Péclet numbers in literature ($K_{\mathrm{Rad,lit}}$=8.79) and similar results were obtained: $K_{\mathrm{Rad,exp}}$=9.55. For the convective contribution of the wall heat transfer coefficient no noticeable relationship could be identified. This is because of the strong sensitivity of the system towards $\lambda_{\mathrm{eff,Rad}}$ and not towards the convective contribution of the wall heat transfer coefficient. This makes it difficult to accurately estimate the parameter, especially at low Péclet numbers. Furthermore, it was observed that the non-convective contribution dominates at the low Péclet numbers. Therefore, the convective contribution was not estimated accurately. For the adsorption experiments and the parametrical sweep, the obtained value for K_{Rad} was used. For the convective contribution of the wall heat transfer coefficient, the correlation of Eurokin was used since this correlation gives a similar value for the non-convective contribution.

To investigate the adsorption characteristics, an isotherm provided by *Linde* Engineering was used. Since the activation procedure could not be reproduced during the in situ activation of the bed a breakthrough curve was measured and the experimental loading was calculated. The experimental loading was compared to the loading obtained by the isotherm and the isotherm was then scaled in order to reproduce the actual capacity of the bed. Afterwards, two different dry flue gases were investigated: 15.2% CO_2 in N_2 and 5% CO_2 in N_2. The regeneration temperature was varied from 120 °C to 200 °C in order to investigate the influence on the recovery and purity of the recovered CO_2. The measurements were then compared with the developed 2D model in order to validate the model and to determine kinetic parameters for the adsorption, desorption, and cooling step. The model showed a good agreement with the measured quantities, especially the CO_2 concentration. Therefore, adequate kinetic parameters could be identified that agreed with literature. The temperature profiles on the other hand showed a small discrepancy between the model and the measurements. This discrepancy was explained by the uncertainty caused by scaling the isotherm with only one reference value, since for higher temperatures it can be expected that the uncertainty will be

higher. On the other hand, only a low Péclet number (Pe<5) could be achieved in the experimental setup. Therefore, flow disturbances that are caused by bypass flows can cause thermal effects. Nevertheless, on an industrial or pilot scale these flow disturbances would be minimized since higher Péclet number (Pe>30) would be envisioned. The measured recoveries and average purities of the recovered CO_2 were compared with those obtained by the numerical model. A discrepancy was observed which can be explained by the uncertainty that is caused by the measuring instruments because of the absence of a purge flow during desorption. The absence of a purge flow makes the analytics difficult and therefore are a source of uncertainty. Nevertheless, the calculated values for the recoveries are within the experimental error and also show the same tendency of the recovery with the regeneration temperatures. The obtained purities of the recovered CO_2 are also within the experimental error. It was observed that the influence of dead volume was significant during the experimental measurements since the obtained purities were not high (<80%). On an industrial or pilot scale, the influence of the dead volume would be significantly lower which would lead to higher purities (>95%) as was shown by the simulations without the dead volume.

Using the derived model and the estimated model parameters (heat conductivity of solid particle 13X, wall Biot number, adsorption kinetics), a simulation was conducted for the industrial case considering a dry flue gas emitted from a coal fired power station. The process performance was measured by three different key performance indicators: The average purity of the recovered CO_2, the CO_2 recovery, and the specific energy demand. For the simulation, only one tube of the tube bundle was considered and it was assumed that all tubes in the bundle behave equally. The results showed that high purities (>98%) could be achieved and satisfactory recoveries ($\approx$ 82%). Nevertheless, the recovery is still below the target value (90%). The calculated specific energy requirement was similar to the one obtained by Clausse et al. ($\approx$ 3.2 $^{W}/_{m^2 \cdot K}$) during his numerical investigation of the indirect heated TSA process using coaxial tubes. Nevertheless, comparing the specific energy demand with the benchmark process, the amine wash, the obtained value is still higher. Therefore, a parametrical study was conducted in order to study the influence of several process, geometry, and physical parameters: Inner diameter, outer heat transfer coefficient, heat conductivity of the solid particle, and regeneration temperature. It was shown that high purities can be achieved using the three tube bundle adsorber system with solid sorbents. In addition, high recoveries were achieved by decreasing the inner radial thermal resistance. The reduction of the radial thermal resistance can be realized either by increasing the effective heat conductivity of the bed or by reducing the inner diameter of the tubes. Since the three tube bundle adsorber system offers the possibility of heat integration, the required energy could be significantly reduced. A further reduction of the energy requirement can be achieved by reducing the inner thermal resistance and by having a fast heat transfer from the tube wall to the heat exchanging medium. The numerical study also revealed that if the investigated parameters were chosen adequately then a suitable process for carbon capture with high purities and recovery can be obtained with an energy requirement lower than the benchmark process, the amine wash.

6.2 Critical review of own work

During the experimental work it was observed that small tubes led to some problems. Therefore, larger tubes would be recommended in order to reduce the influence not only of heat losses but also of thermal inlet effects. Using longer tubes would allow to measure a wider range of Péclet numbers during convective experiments. This was one of the major problems that were observed during the experimental work, since the small tube limited the range of possible Péclet numbers. Nevertheless, for the non convective experiments the length of the tube was not an issue. Therefore, the obtained results for the non-convective experiments can be taken as a solid basis for further investigations. For the convective experiments a wider range of Péclet numbers must be investigated. That is only possible if longer tubes are used.

The estimation of the Bi number was conducted using only one d-to-d_p ratio. Even though this ratio is a realistic ratio at industrial scale, a wider range of ratios would have made a more accurate estimation possible. Nevertheless, the obtained value can be taken as a basis for further investigations and as an indication of which correlation in literature is more accurate when using tubes packed with solid sorbents.

The adsorption experiments were conducted using pure gases. Therefore, the influence of water was not considered. It is known that water will have a negative impact on the CO_2 adsorption capacity on zeolites. Nevertheless, the main goal of this work was to investigate the applicability of an indirect heated TSA process to CO_2 capture. The obtained results can therefore be taken as an indication of its applicability, but it has to be kept in mind that water will have to be removed on an industrial scale using either a TSA-unit, a layered bed inside of the tube bundle, or another method.

It is worth mentioning that the numerical study was conducted under several simplifying assumptions. Also, some of the values used during the parametrical study for the heat conductivity of the solid particle do not represent values that can be achieved with standard adsorbents. Therefore, the obtained results have to be taken as an indication of the system behavior and what parameters can be improved in order to enhance the process using tube bundle adsorbers.

6.3 Outlook

This work showed that the indirect heated and cooled TSA process represents a promising alternative for CO_2 capture. Nevertheless, some optimization of the process is still required. For example, the proposed process scheme: 3 bed system with a cycle time of 3 hours, represents only one viable option and different advanced schemes could improve the process. The numerical sweep showed that a reduction of the radial thermal resistance leads to better results. Therefore, different adsorbents should be investigated,

such as structured adsorbent. The use of structured adsorbent could lead to higher effective thermal conductivities and therefore reduce the radial thermal resistance. This would also reduce the cycle time. Another advantage of using structured adsorbents would be a reduction of the pressure drop (around 90 mbar in this work), which is a main issue when capturing CO_2 from a source with low pressure such as flue gas or air. In order to be utilized or to improve the process, these structured adsorbents would need to have a high adsorption capacity that is comparable to 13 X and a higher effective heat conductivity. If these adsorbents would tolerate water by, for example, using amine groups, a further advantage would be achieved. Another possibility for reducing the radial thermal resistance would be the use of fins inside the tube. The improvement in the effective heat conductivity would need to be investigated and the bypass flows that could be caused because of the form of the fins. Nonetheless, bypass flows would not be problematic as long as the recovery is not altered significantly. In addition to the reduction of the radial thermal resistance, the heat integration between the tube bundle adsorbers must be investigated in detail since this is one of the major advantages of this system. The influence of water on the process performance should also be investigated in detail.

Indirect heated and cooled TSA processes offer a new alternative for CO_2 capture. This process can be further improved since it is a new technology in the development stage.

A Flue gas 1

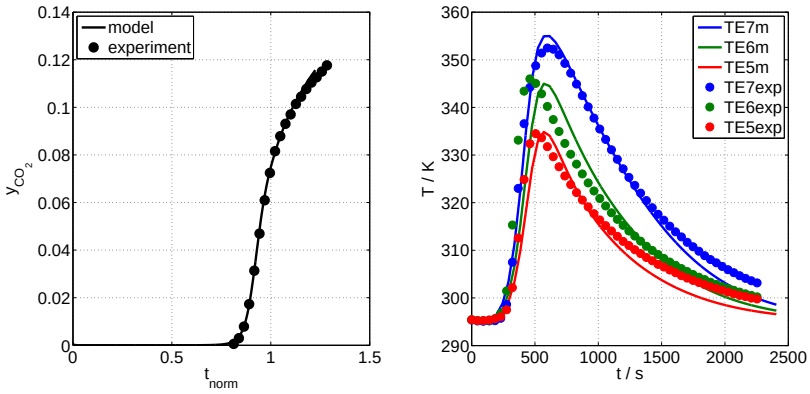

(a) y_{CO_2}, adsorption (b) Temperature, adsorption

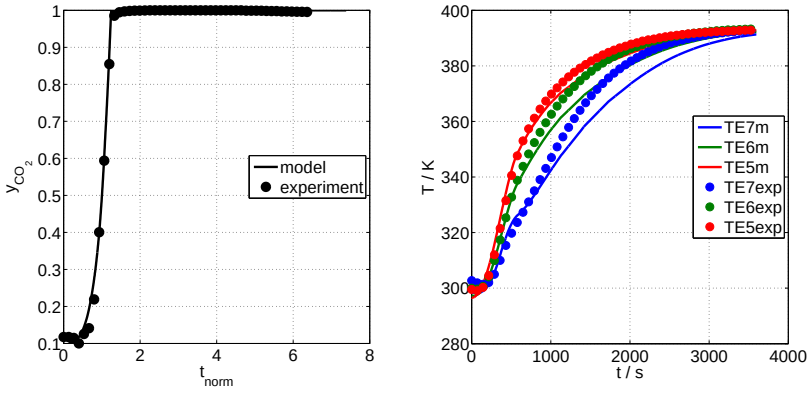

(c) y_{CO_2}, desorption (d) Temperature, desorption

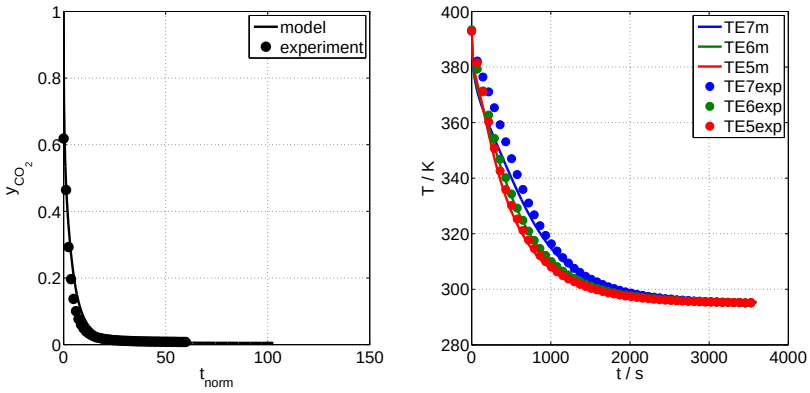

(e) y_{CO_2}, cooling (f) Temperature, cooling

Figure A.1: Concentration and temperature profiles for the first simulated dry flue gas using a regeneration temperature of 120 °C.

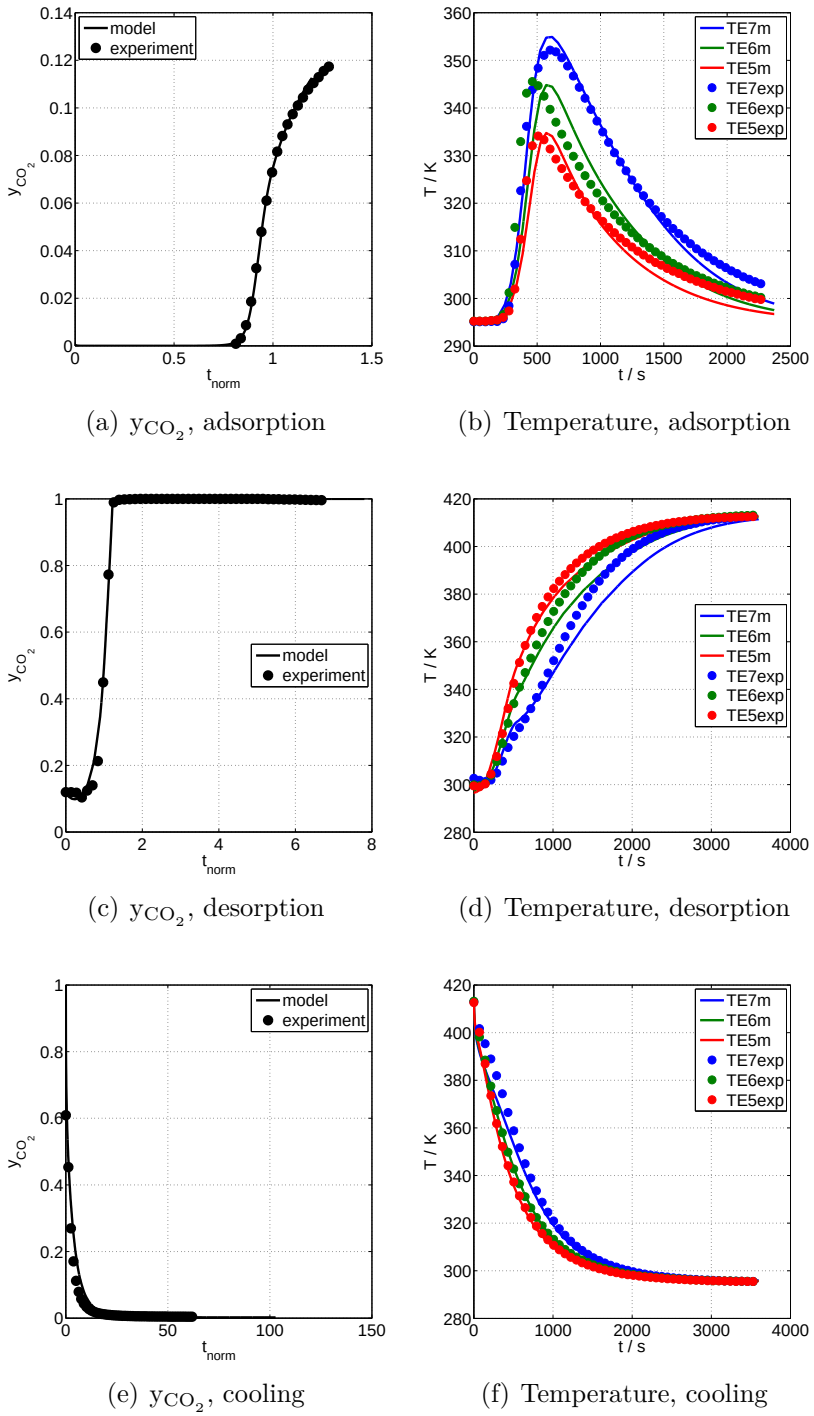

(a) y_{CO_2}, adsorption (b) Temperature, adsorption

(c) y_{CO_2}, desorption (d) Temperature, desorption

(e) y_{CO_2}, cooling (f) Temperature, cooling

Figure A.2: Concentration and temperature profiles for the first simulated dry flue gas using a regeneration temperature of 140 °C.

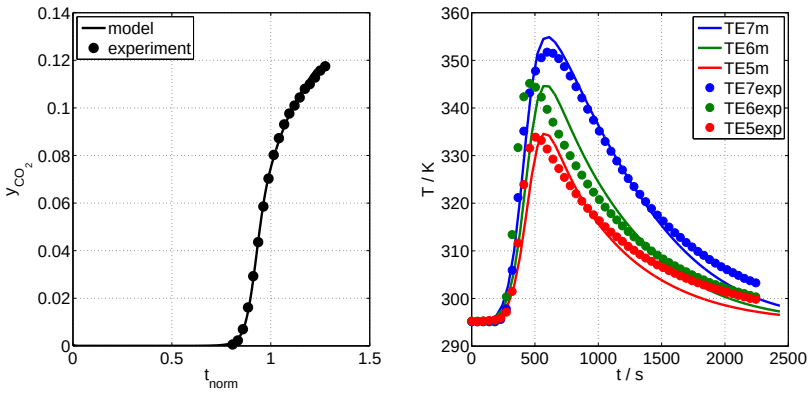

(a) y_{CO_2}, adsorption (b) Temperature, adsorption

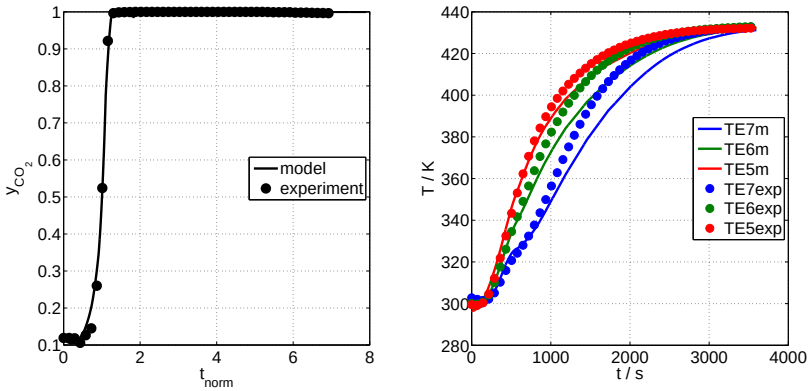

(c) y_{CO_2}, desorption (d) Temperature, desorption

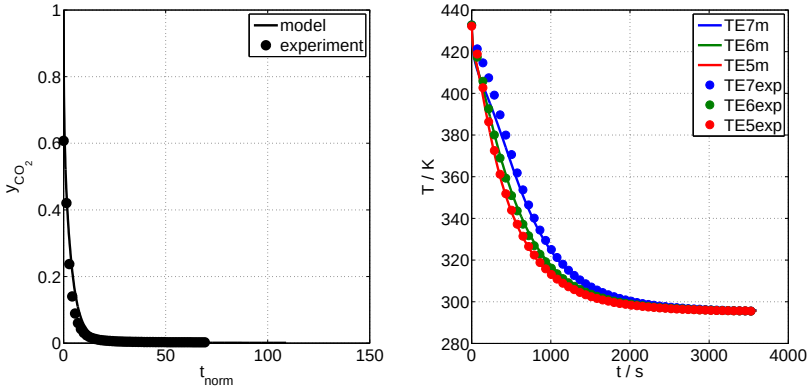

(e) y_{CO_2}, cooling (f) Temperature, cooling

Figure A.3: Concentration and temperature profiles for the first simulated dry flue gas using a regeneration temperature of 160 °C.

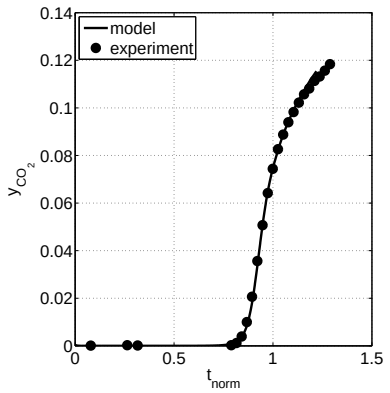

(a) y_{CO_2}, adsorption

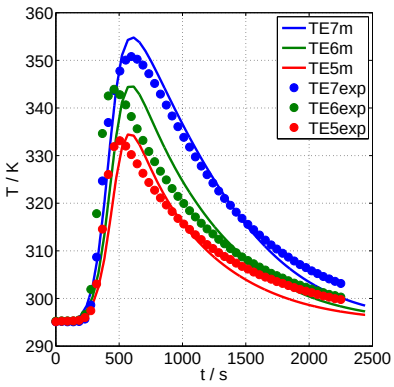

(b) Temperature, adsorption

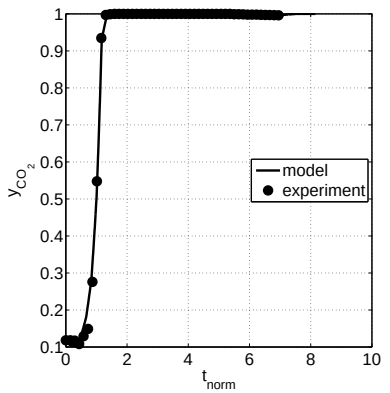

(c) y_{CO_2}, desorption

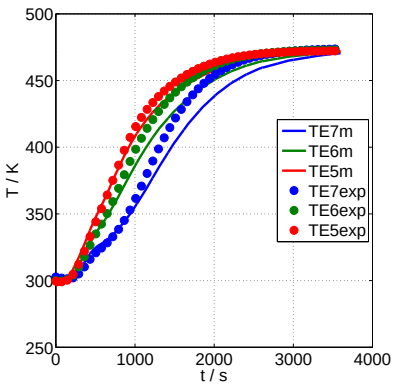

(d) Temperature, desorption

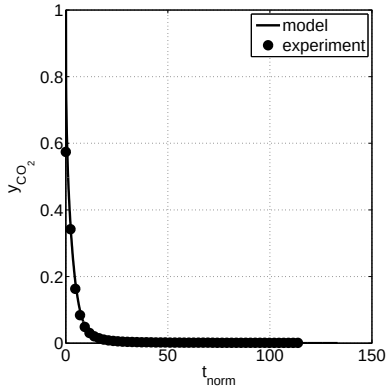

(e) y_{CO_2}, cooling

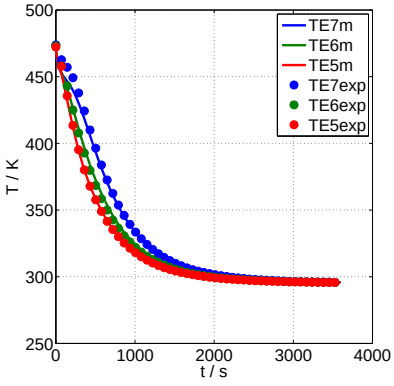

(f) Temperature, cooling

Figure A.4: Concentration and temperature profiles for the first simulated dry flue gas using a regeneration temperature of 200 °C.

B Flue gas 2

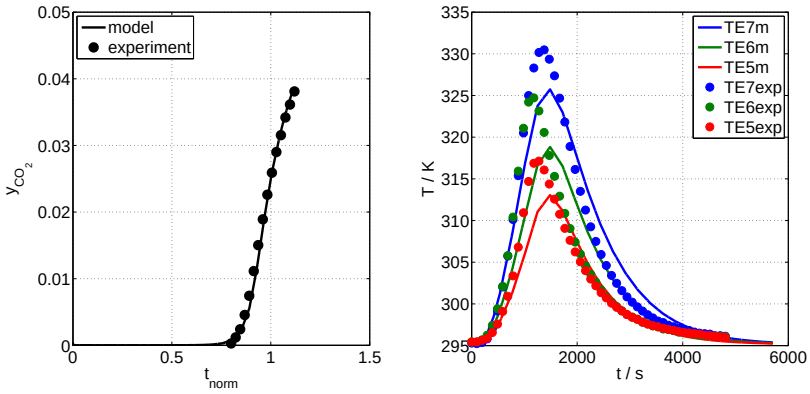

(a) y_{CO_2}, adsorption (b) Temperature, adsorption

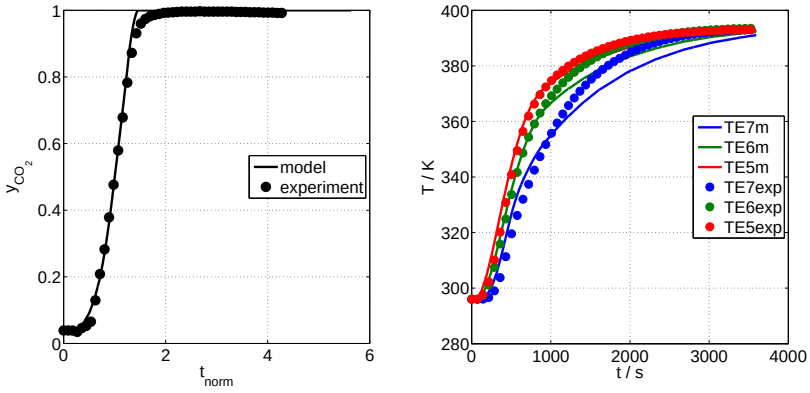

(c) y_{CO_2}, desorption (d) Temperature, desorption

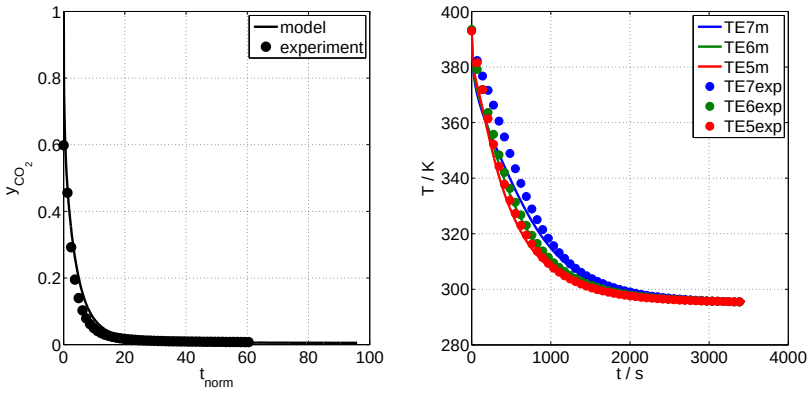

(e) y_{CO_2}, cooling (f) Temperature, cooling

Figure B.1: Concentration and temperature profiles for the second simulated dry flue gas using a regeneration temperature of 120 °C.

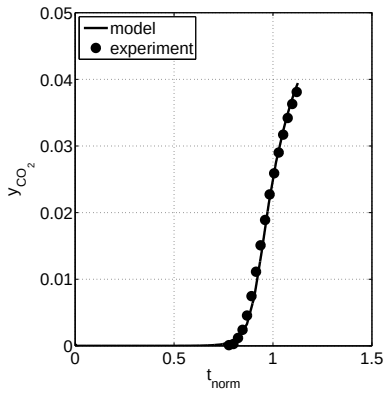

(a) y_{CO_2}, adsorption

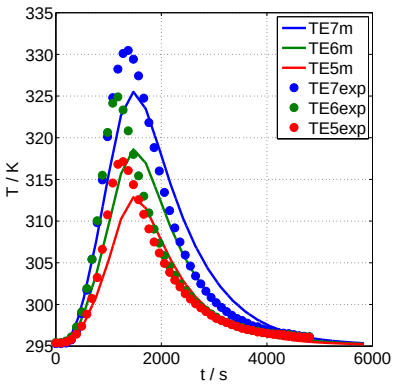

(b) Temperature, adsorption

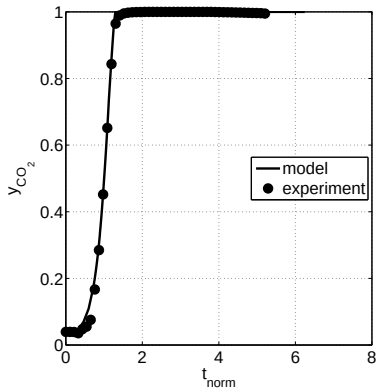

(c) y_{CO_2}, desorption

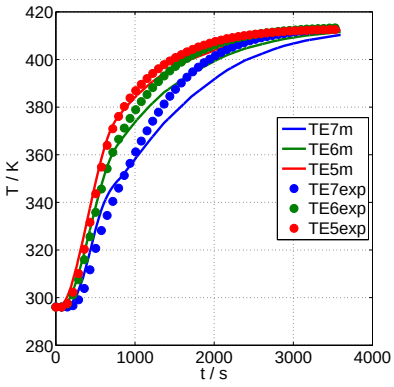

(d) Temperature, desorption

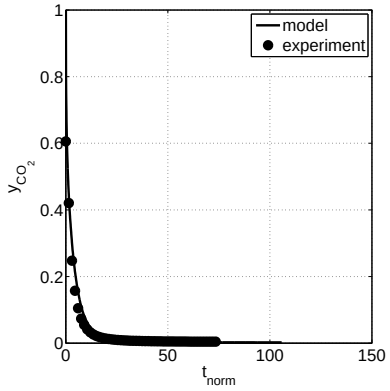

(e) y_{CO_2}, cooling

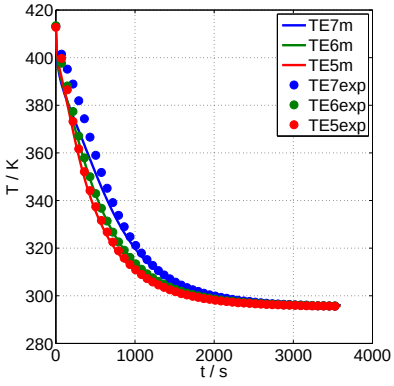

(f) Temperature, cooling

Figure B.2: Concentration and temperature profiles for the second simulated dry flue gas using a regeneration temperature of 140 °C.

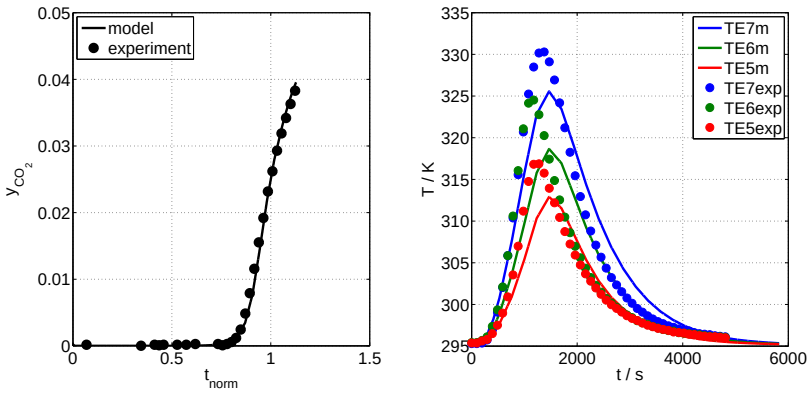

(a) y_{CO_2}, adsorption (b) Temperature, adsorption

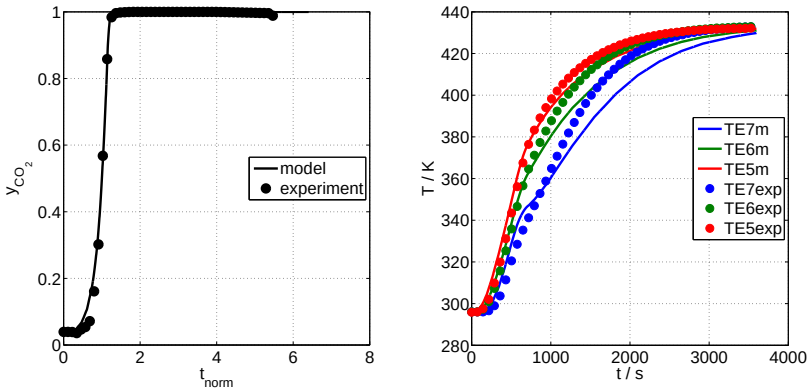

(c) y_{CO_2}, desorption (d) Temperature, desorption

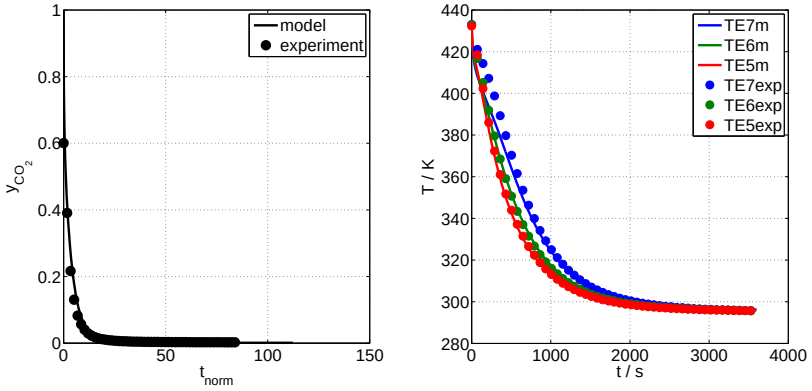

(e) y_{CO_2}, cooling (f) Temperature, cooling

Figure B.3: Concentration and temperature profiles for the second simulated dry flue gas using a regeneration temperature of 160 °C.

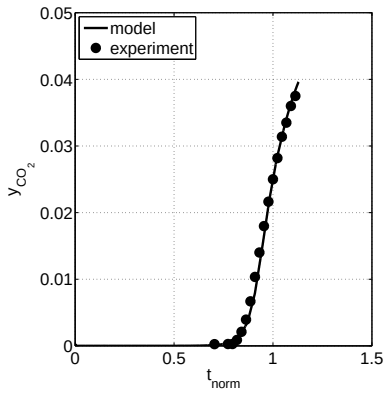

(a) y_{CO_2}, adsorption

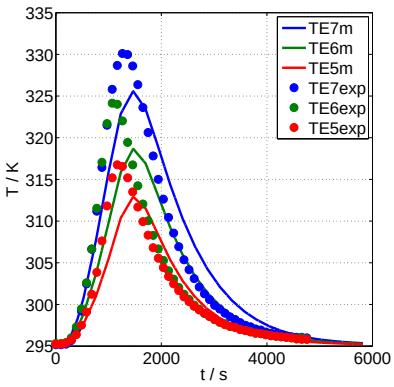

(b) Temperature, adsorption

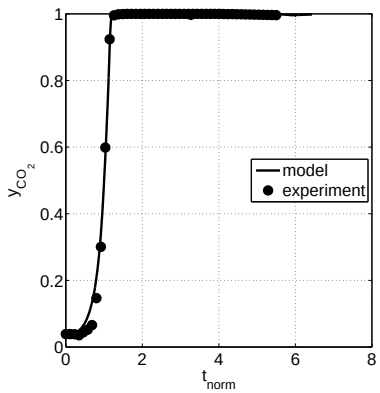

(c) y_{CO_2}, desorption

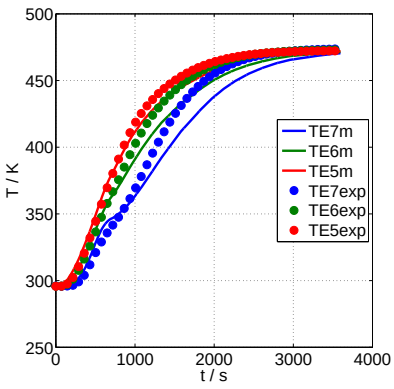

(d) Temperature, desorption

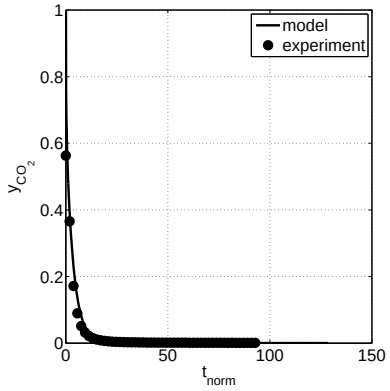

(e) y_{CO_2}, cooling

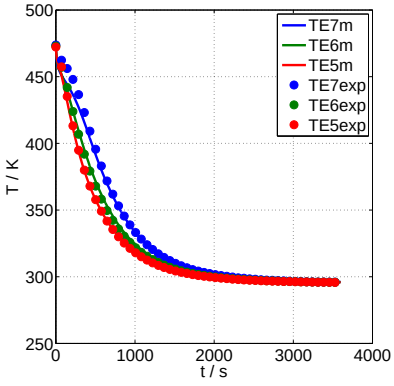

(f) Temperature, cooling

Figure B.4: Concentration and temperature profiles for the second simulated dry flue gas using a regeneration temperature of 200 °C.

Bibliography

[1] Xiaohui Zhang. Studies on Multphase CO_2 Capture Systems. In *Fortschritt-Bericht VDI, Reihe 3: Verfahrenstechnik, Nr. 884*. VDI-Verlag, 2007.

[2] Eugene S. Genkin, Hoanh Nang Pham, Xiaoguang Zhang, and Keith Alan Ludwig. Process and Apparatus for Producing Hydrogen and Carbon Monoxide. Patent, 2014. US 8808425 (B2).

[3] Shivaji Sircar. Rapid thermal swing adsorption. Patent, 2003. US 20030037672 (A1).

[4] International Energy Agency. *World Energy Outlook 2012*. IEA Publishing, 2012.

[5] Zero Emissions Platform. *Recommendations for Research to Support CCS Deployment in Europe beyond 2020: Update on CO_2 Capture*. European Technology Platform for Zero Emission Fossil Fuel Power Plants, 2013.

[6] Zero Emissions Platform. *CO_2 Capture and Use (CCU): The Potential to Reduce CO_2 Emissions and Accelerate CCS Deployment in Europe*. European Technology Platform for Zero Emission Fossil Fuel Power Plants, 2013.

[7] Zero Emissions Platform. *Biomass with CO_2 Capture and Storage (Bio-CCS)*. European Technology Platform for Zero Emission Fossil Fuel Power Plants, 2012.

[8] Christopher W. Jones. CO_2 Capture from Dilute Gases as a Component of Modern Global Carbon Management. *Annual Review of Chemical and Biomolecular Engineering*, 2:31–52, 2011.

[9] Ryan P. Lively, Daniel P. Leta, Bruce A. DeRites, Ronald R. Chance, and William J. Koros. Hollow fiber adsorbents for CO_2 capture: Kinetic sorption performance. *Chemical Engineering Journal*, 171(3):801–810, 2011.

[10] www.epa.gov/cleanpowerplan/clean-power-plan-existing-power-plants, [Accesed 11.01.2016].

[11] http://www.cop21.gouv.fr/en/, [Accesed 11.01.2016].

[12] Zero Emissions Platform. *The Costs of CO_2 Capture*. European Technology Platform for Zero Emission Fossil Fuel Power Plants, 2011.

[13] Ryan P. Lively. *Hollow fiber sorbents for post-combustion CO_2 capture*. PhD thesis, Georgia Institute of Technology, 2011.

[14] Paula Galindo, Anke Schäffer, Kevin Brechtel, Sven Unterberger, and Günter Scheffknecht. Experimental research on the performance of CO_2-loaded solutions of MEA and DEA at regeneration conditions. *Fuel*, 101:2–8, 2012.

[15] Jose D. Figueroa, Timothy Fout, Sean Plasynski, Howard McIlvried, and Rameshwar D. Srivastava. Advances in CO_2 capture technology - The U.S. Department of Energy's Carbon Sequestration Program. *International Journal of Greenhouse Gas Control*, 2:9–20, 2008.

[16] Gary T. Rochelle. Amine Scrubbing for CO_2 Capture. *Science*, 325:1652–1654, 2009.

[17] C. Kandziora. New solvent based post combustion CO_2 capture in power plants: A joint development and commercial application. In *COAL-GEN EUROPE Conference*, 2012.

[18] Mai Bui, Indra Gunawan, Vincent Verheyen, Paul Feron, Erik Meuleman, and Sam Adeloju. Dynamic modelling and optimisation of flexible operation in post-combustion CO_2 capture plants - A review. *Computers and Chemical Engineering*, 61:245–265, 2014.

[19] Hailong Li, Geir Haugen, Mario Ditaranto, David Berstad, and Kristin Jordal. Impacts of exhaust gas recirculation (EGR) on the natural gas combined cycle integrated with chemical absorption CO_2 capture technology. *Energy Procedia*, 4:1411–1418, 2011.

[20] Monika Vogt, Ralf Goldschmidt, Dieter Bathen, Bernhard Epp, and Hans Fahlenkamp. Comparison of membrane contactor and structured packings for CO_2 absorption. *Energy Procedia*, 4:1471–1477, 2011.

[21] Tim C. Merkel, Haiqing Lin, Xiaotong Wei, and Richard Baker. Power plant post-combustion carbon dioxide capture: An opportunity for membranes. *Journal of Membrane Science*, 359:126–139, 2010.

[22] Reza Haghpanah, Ricky Nilman, Arvind Rajendran, Shamsuzzaman Farooq, and Iftekhar A. Karimi. Cycle Synthesis and Optimiztion of a VSA Process for Postcombustion CO_2 Capture. *AIChE Journal*, 59(12):4735–4747, 2013.

[23] Shreenath Krishnamurthy, Vemula Rama Rao, Sathishkumar Guntuka, Paul Sharratt, Reza Haghpanah, Arvind Rajendran, Mohammad Amanullah, Iftekhar A. Karimi, and Shamsuzzaman Farooq. CO_2 Capture from Dry Flue Gas by Vacuum Swing Adsorption: A Pilot Plant Study. *AIChE Journal*, 60(5):1830–1841, 2014.

[24] Minh T. Ho, Guy W. Allinson, and Dianne E. Wiley. Reducing the Cost of CO_2 Capture from Flue Gases Using Pressure Swing Adsorption. *Ind. Eng. Chem. Res.*, 47:4883–4890, 2008.

[25] Alan L. Chaffee, Gregory P. Knowles, Zhijian Liang, Jun Zhang, Penny Xiao, and Paul A. Webley. CO_2 capture by adsorption: Materials and process development. *International Journal of Greenhouse Gas Control*, 1(1):11–18, 2007.

[26] Lu Wang, Zhen Liu, Ping Li, Jin Wang, and Jianguo Yu. CO_2 capture from flue gas by two successive VPSA units using 13XAPG. *Adsorption*, 18(5-6):445–459, 2012.

[27] Ermano Filippi. Process for removing carbon dioxide from a gas stream. Patent, 2013. EP 2638949 (A1).

[28] Ryan P Lively, Ronald R. Chance, B. T. Kelley, Harry W. Deckman, Jeffery H. Drese, Christopher W. Jones, and William J. Koros. Hollow Fiber Adsorbents for CO_2 Removal from Flue Gas. *Ind. Eng. Chem. Res.*, 48:7314–7324, 2009.

[29] Ryan P. Lively, Ronald R. Chance, and William J. Koros. Enabling Low-Cost CO_2 Capture via Heat Integration. *Industrial and Engineering Chemistry Research*, 49(16):7550–7562, 2010.

[30] Ryan Lively, R. Chance, William J. Koros, Harry W. Deckman, and Bruce T. Kelley. Sorbent fiber compositions and methods of temperature swing adsorption. Patent, 2012. US 8257474 (B2).

[31] Fateme Rezaei, Ryan P. Lively, Ying Labreche, Grace Chen, Yanfang Fan, William J. Koros, and Christopher W. Jones. Aminosilane-Grafted Polymer/Silica Hollow Fiber Adsorbents for CO_2 Capture from Flue Gas. *ACS Appl. Mater. Interfaces*, 5(9):3921–3931, 2013.

[32] Fuyue Stephanie Li, Ryan P. Lively, Jong Suk Lee, and William J. Koros. Aminosilane-Functionalized Hollow Fiber Sorbents for Post-Combustion CO_2 Capture. *Industrial & Engineering Chemistry Research*, 52:8928–8935, 2013.

[33] Fateme Rezaei, Swernath Subramanian, Jayashree Kalyanaraman, Ryan P. Lively, Yoshiaki Kawajiri, and Matthew J. Realff. Modeling of rapid temperature swing adsorption using hollow fiber sorbents. *Chemical Engineering Science*, 113:62–76, 2014.

[34] Yanfang Fan, Ying Labreche, Ryan P. Lively, Christopher W. Jones, and William J. Koros. Dynamic CO_2 Adsoprtion Performance of Internally Cooled Silica-Supported Poly(ethylenimine) Hollow Fiber Sorbents. *AIChE Journal*, 60(11):3878–3887, 2014.

[35] Ying Labreche, Yanfang Fan, Ryan P. Lively, Christopher W. Jones, and William J. Koros. Direct dual layer spinning of aminosilica/TorlonVR hollow fiber sorbents with a lumen layer for CO_2 separation by rapid temperature swing adsorption. *Journal of Applied Polymer Science*, 132(17):41845, 2015.

[36] Ravi Jain. Carbon Dioxide Recovery. Patent, 2013. US 8591627 (B2).

[37] Jocelyn Bonjour, Jean-Bertrand Chalfen, and Francis Meunier. Temperature Swing Adsorption Process with Indirect Cooling and Heating. *Ind. Eng. Chem. Res.*, 41:5802–5811, 2002.

[38] J. Merel, M. Clausse, and F. Meunier. Carbon dioxide capture by indirect thermal swing adsorption using 13X zeolite. *Environmental progress*, 25(4):327–333, 2006.

[39] Jerome Merel, Marc Clausse, and Francis Meunier. Experimental Investigation on CO_2 Post-Combustion Capture by Indirect Thermal Swing Adsorption Using 13X and 5A Zeolites. *Industrial & Engineering Chemistry Research*, 47(1):209–215, 2008.

[40] M. Clausse, J. Merel, and F. Meunier. Numerical parametric study on CO_2 capture by indirect thermal swing adsorption. *International Journal of Greenhouse Gas Control*, 5:1206–1213, 2011.

[41] K. B. Lee and S. Sircar. Removal and Recovery of Compressed CO_2 from Flue Gas by a Novel Thermal Swing Chemisorption Process. *AIChE Journal*, 54(9):2293–2302, 2008.

[42] Michael G. Beaver and Shivaji Sircar. Adsorption technology for direct recovery of compressed, pure CO_2 from a flue gas without pre-compression or pre-drying. *Adsorption*, 16:103–111, 2010.

[43] Dieter Bathen and Marc Breitbach. *Adsorptionstechnik*. Springer, 2001.

[44] Duong D. Do. *Adsorption Analysis: Equilibria and Kinetics*, volume 2. Imperial College Press, 1998.

[45] Werner Kast. *Adsorption aus der Gasphase*. VCH Verlagsgesellschaft, 1988.

[46] Douglas M. Ruthven. *Principles of Adsoprtion and Adsoprtion Processes*. John Wiley & Sons, 1984.

[47] H.-J. Bart and U. von Gemmingen. Adsorption. In *Ullmann's Encyclopedia of Industrial Chemistry*. Wiley-VCH Verlag, 2005.

[48] U. von Gemmingen, A. Mersmann, W. Sievers, and P. Schweighart. Adsorptionsapparate. In *Verfahrenstechnische Berechnungsmethoden Teil 2: Thermisches Trennen (Eds: S. Weiß)*. Deutscher Verlag für Grundstoffindustrie, 1996.

[49] Gang Li, Penny Xiao, Paul A. Webley, Jun Zhang, and Ranjeet Singh. Competition of CO_2/H_2O in adsorption based CO_2 capture. *Energy Procedia*, 1:1123–1130, 2009.

[50] M. Gholami and M. R. Talaie. Investigation of Simplifying Assumptions in Mathematical Modeling of Natural Gas Dehydration Using Adsorption Process and Introduction of a New Accurate LDF Model. *Ind. Eng. Chem. Res.*, 49:838–846, 2010.

[51] Se-Il Yang, Do-Young Choi, Seong-Cheol Jang, Sung-Hyun Kim, and Dae-Ki Choi. Hydrogen separation by multi-bed pressure swing adsorption of sysnthesis gas. *Adsorption*, 14:583–590, 2008.

[52] Dr. Adolf Fick. Ueber diffusion. *Annalen der Physik*, 170(1):59–86, 1855.

[53] Edward N. Fuller, Paul D. Schettler, and J. Calvin Giddings. A new method for prediction of binary gas-phase diffusion coefficients. *Industrial & Engineering Chemistry*, 58(5):19–27, 1966.

[54] D. R. Garg and D. M. Ruthven. Linear driving force approximations for diffusion controlled adsorption in molecular sieve columns. *AIChE Journal*, 21(1):200–202, 1975.

[55] S. Sircar and J.R. Hufton. Why does the Linear Driving Force Model for Adsorption Kinetics Work? *Adsorption*, 6(2):137–147, 2000.

[56] Hsiao-Kuo Hsuen. An improved linear driving force approximation for intraparticle adsorption. *Chemical Engineering Science*, 55:3475–3480, 2000.

[57] Matthias Stegmaier. *Modular Simulation of Pressure Swing Adsorption for Hydrogen Purification in Compact Units*. PhD thesis, Institut für Chemische Verfahrenstechnik der Universität Stuttgart, 2008.

[58] Michael Nilles. Wärmeübertragung an der Wand durchströmter Schüttungsrohre. In *Fortschritt-Bericht VDI, Reihe 3: Verfahrenstechnik, Nr. 264*. VDI-Verlag, 1991.

[59] H. A. Deans and Leon Lapidus. A Computational Model For Predicting and Correlating the Behavior of Fixed-Bed Reactors: I. Derivation of Model for Nonreactive Systems. *AIChE Journal*, 6(4):656–663, 1960.

[60] H. A. Deans and Leon Lapidus. A Computational Model for Predicting and Correlating the Behavior of Fixed-Bed Reactors: II. Extension to Chemical Reactive Systems. *AIChE Journal*, 6(4):663–668, 1960.

[61] VDI. *VDI-Wärmeatlas*. Springer-Verlag, 2002.

[62] Dieter Vortmeyer. Packed Bed Thermal Dispersion Models and Consistent Sets of Coefficients. *Chem. Eng. Process.*, 26:263–268, 1989.

[63] Dongsheng Wen and Yulong Ding. Heat transfer of gas flow through a packed bed. *Chemical Engineering Science*, 61:3532–3542, 2006.

[64] Dr.-Ing. Evangelos Tsotsas. Über die Wärme- und Stoffübertragung in durchströmten Festbetten; Experimente, Modelle, Theorien. In *Fortschritt-Bericht VDI, Reihe 3: Verfahrenstechnik, Nr. 223*. VDI-Verlag, 1990.

[65] Holger Martin and Michael Nilles. Radiale Wärmeleitung in durchströmten Schüttungsrohren. *Chemie Ingenieur Technik*, 65(12):1468–1477, 1993.

[66] M. Winterberg, E. Tsotsas, A. Krischke, and D. Vortmeyer. A simple and coherent set of coeffcients for modelling of heat and mass transport with and without chemical reaction in tubes filled with spheres. *Chemical Engineering Science*, 55:967–979, 2000.

[67] M. Giese. *Strömung in porösen Medien unter Berücksichtigung effektiver Viskositäten*. PhD thesis, TU München, 1998.

[68] Oliver Bey and Gerhart Eigenberger. Fluid flow through catalyst filled tubes. *Chemical Engineering Science*, 52(8):1365–1376, 1997.

[69] E. Achenbach. Heat and Flow Characteristics of Packed Beds. *Experimental Thermal and Fluid Science*, 10:17–27, 1995.

[70] Oliver Bey and Gerhart Eigenberger. Gas flow and heat transfer through catalyst filled tubes. *Int. J. Therm. Sci.*, 40:152–164, 2001.

[71] E. I. Smirnov, A. V. Muzykantov, V. A. Kuzmin, A.E. Kronberg, and I. A. Zolotarskii. Radial heat transfer in packed beds of spheres, cylinders and Rashig rings Verification of model with a linear variation of λ_{er} in the vecinity of the wall. *Chemical Engineering Journal*, 91:243–248, 2003.

[72] M. Giese, K. Rottschäfer, and D. Vortmeyer. Measured and Modeled Superficial Flow Profiles in Packed Beds with Liquid Flow. *AIChE*, 44(2):484–490, 1998.

[73] D. Vortmeyer and E. Haidegger. Discrimination of three approaches to evaluate heat fluxes for wall-cooled fixed bed chemical reactors. *Chemical Engineering Science*, 46(10):2651–2660, 1991.

[74] D. Vortmeyer and Ping Cheng. Transverse thermal dispersion and wall channelling in a packed bed with forced convective flow. *Chemical Engineering Science*, 43(9):2523–2532, 1988.

[75] Bert Koning. *Heat and Mass Transport in Tubular Packed Bed Reactors at Reacting and Non-Reacting Conditions*. PhD thesis, University of Twente, 2002.

[76] G. Sonntag. Einfluß des Lückenvolumens auf den Druckverlust in gasdurchströmten Füllkörpersäulen. *Chemie Ingenieur Technik*, 32:317–329, 1960.

[77] EUROKIN_fixed-bed_html. *EUROKIN spreadsheet on requirements for measurement of intrinsic kinetics in the gas-solid fixed-bed reactor*, 2012.

[78] T. L. P. Dantas, F. M. T. Luna, I. J. Silva Jr., A. E. B. Torres, D. C. S. de Azevedo, A. E. Rodrigues, and R. F. P. M. Moreira. Modeling of the fixed-bed adsorption of carbon dioxide and a carbon dioxide nitrogen mixture on zeolite 13 X. *Brazilian Journal of Chemical Engineering*, 28(3):533–544, 2011.

[79] J. G. H. Borkink and K. R. Westertrep. Influence of Tube and Particle Diameter on Heat Transport in Packed Beds. *AIChE Journal*, 38(5):703–715, 1992.

[80] Anthony G. Dixon. Heat Transfer in Fixed Beds at Very Low (<4) Tube-to-Particle Diameter Ratio. *Ind. Eng. Chem. Res.*, 36:3053–3064, 1997.

[81] A. S. Lamine, L. Gerth, H. LE Gall, and G. Wild. Heat Transfer in a Packed Bed Reactor with Cocurrent Downflow of a Gas and a Liquid. *Chemical Engineering Science*, 51(15):3813–3827, 1996.

[82] Olaf R. Derkx and Anthony G. Dixon. Determination of the fixed bed wall heat transfer coefficient using computational fluid dynamics. *Numerical Heat Transfer, Part A*, 29:777–794, 1996.

[83] A. G. Dixon and D. L. Cresswell. Effective heat transfer parameters for transient packed-bed models. *AIChE Journal*, 32(5):809–819, 1986.

[84] Wangyun Won, Seunghun Lee, and Kwang Soon Lee. Modeling and parameter estimation for a fixed-bed adsorption process for CO_2 capture using zeolite 13X. *Separation and Purification Technology*, 85:120–129, 2012.

[85] O. Kirscher. *Die wissenschaftlichen Grundlagen der Trocknungstechnik*. Springer-Verlag, 1956.

[86] P. Zehner and E.U. Schlünder. Wärmeleitfähigkeit von Schüttungen bei mäßigen Temperaturen. *Chemie Ingenieur Technik*, 42(14):933–941, 1970.

[87] Noriaki Wakao and Koichi Kato. Effective Thermal conductivity of Packed Beds. *Journal of Chemical Engineering of Japan*, 2(1):24–33, 1969.

[88] D. Vortmeyer and S. Le Mong. Anwendung des Äquivalenzprinzipes zwischen Ein- und Zwei-phasenmodellen auf die Lösung der Regeneratorgleichungen. *Wärme-und Stoffübertragung*, 9:29–37, 1976.

[89] Wolfgang Polifke and Jan Kopitz. *Wärmeübertragung: Grundlagen, analytische und numerische Methoden*. Pearson Studium, 2009.

[90] Peter von Boeckh and Thomas Wetzel. *Heat transfer: Basics and Practice*. Springer-Verlag, 2011.

[91] Ernst-Ulrich Schlünder and Evangelos Tsotsas. *Wärmeübertragung in Festbetten, durchmischten Schüttgütern und Wirbelschichten*. Georg Thieme Verlag, 1988.

[92] Mohammad Saleh Shafeeyan, Wan Mohd Ashri Wan Daud, and Ahmad Shamiri. A review of mathematical modeling of fixed-bed columns for carbon dioxide adsorption. *Chemical Engineering Research and Design*, 92:961–988, 2014.

[93] R. Byron Bird, Warren E. Stewart, and Edwin N. Lightfoot. *Transport Phenomena*. John Wiley & Sons, Inc., 2002.

[94] Erich Hahne. *Technische Thermodynamik: Einführung und Anwendung*. Oldenbourg Verlag, 2010.

[95] J. F. Richardson and J.H. Harker with J.R. Backhurst. *Coulson and Richardson's chemical engineering, Vol. 2, Particle technology and separation processes*. Butterworth-Heinemann, 2002.

[96] G. Damköhler. *Einfluss von Diffusion Strömung und Wärmetransport auf die Ausbeute bei chemisch-technischen Reaktionen*. Akademische Verlagsgesellschaft m.b.H, 1957.

[97] Sabri Ergun. Fluid Flow Through Packed Columns. *Chemical Engineering Progress*, 48(2):89–94, 1952.

[98] B.E. Poling, J. M. Prausnitz, and J. P. O'Connell. *The Properties of Gases and Liquids*. 5th edition, 2001.

[99] Hans-Jörg Zander. *Dynamische Modellierung reaktionskinetischer Systeme mit Neuronalen Netzen und hybriden Modellen*. PhD thesis, Universität Erlangen-Nürnberg, 1999.

[100] Yonathan Bard. *Nonlinear Parameter Estimation*. Academic Press, 1974.

[101] ABB. *Datenblatt Advance Optima AO2000 Serie, Kontinuierliche Gasanalysatoren Modelle AO2020, AO2040*.

[102] Bronkhorst HIGH-TECH. *Datenblatt F-201CV, Massendurchflussregler für Gase*.

[103] MathWorks. *Matlab R2015b Documentation*.

[104] Bastian Steuten. *Adsoprtive Entfernung von Schwefelverbindungen aus Erdgas*. PhD thesis, Universität Duisburg-Essen, 2014.

[105] Gabriel Salazar Duarte, Benedikt Schürer, Christian Voss, and Dieter Bathen. Modeling and Simulation of a Tube Bundle Adsorber for the Capture of CO_2 from Flue Gases. *Chemie Ingenieur Technik*, 88(3):1–11, 2016.